AUTOMATIC SEGMENTATION AND CLASSIFICATION OF RED AND WHITE BLOOD CELLS IN THIN BLOOD SMEAR SLIDES

Mehdi Habibzadeh Motlagh

A thesis
in
The Department
of
Computer Science

Presented in Partial Fulfillment of the Requirements
For the Degree of Doctor of Philosophy
Concordia University
Montréal, Québec, Canada

August 2015

Concordia University
School of Graduate Studies

This is to certify that the thesis prepared

By: **Mr. Mehdi Habibzadeh Motlagh**

Entitled: **Automatic Segmentation and Classification of Red and White Blood cells in Thin Blood Smear Slides**

and submitted in partial fulfillment of the requirements for the degree of

Doctor of Philosophy (Computer Science)

complies with the regulations of this University and meets the accepted standards with respect to originality and quality.

Signed by the final examining commitee:

Dr. Otmane Ait Mohamed	: Chair
Dr. Farida Cheriet	: External Examiner
Dr. Nawwaf Kharma	: Examiner
Dr. Tien D. Bui	: Examiner
Dr. Sudhir Mudur	: Examiner
Dr. Adam Krzyżak	: Supervisor
Dr. Thomas G. Fevens	: Co-supervisor

Approved Dr. Volker Haarslev
Chair of Department or Graduate Program Director

_____ 2015 _____

Amir Asif, PhD, PEng
Dean Faculty of Engineering and Computer Science

Abstract

Automatic Segmentation and Classification of Red and White Blood cells in Thin Blood Smear Slides

Mehdi Habibzadeh Motlagh, Ph.D.
Concordia University, 2015

In this work we develop a system for automatic detection and classification of cytological images which plays an increasing important role in medical diagnosis. A primary aim of this work is the accurate segmentation of cytological images of blood smears and subsequent feature extraction, along with studying related classification problems such as the identification and counting of peripheral blood smear particles, and classification of white blood cell into types five. Our proposed approach benefits from powerful image processing techniques to perform complete blood count (CBC) without human intervention. The general framework in this blood smear analysis research is as follows. Firstly, a digital blood smear image is de-noised using optimized Bayesian non-local means filter to design a dependable cell counting system that may be used under different image capture conditions. Then an edge preservation technique with Kuwahara filter is used to recover degraded and blurred white blood cell boundaries in blood smear images while reducing the residual negative effect of noise in images. After denoising and edge enhancement, the next step is binarization using combination of Otsu and Niblack to separate the cells and stained background. Cells separation and counting is achieved by granulometry, advanced active contours without edges, and morphological operators with watershed algorithm. Following this is the recognition of different types of white blood cells (WBCs), and also red blood cells (RBCs) segmentation. Using three main types of features: shape, intensity, and texture invariant features in combination with a variety of classifiers is next step. The following features are used in this work: intensity histogram features, invariant moments, the relative area, co-occurrence and run-length matrices, dual tree complex wavelet transform features, Haralick and Tamura features. Next, different statistical approaches involving correlation, distribution and redundancy are used to measure of the dependency between a set of features and to select feature

variables on the white blood cell classification. A global sensitivity analysis with random sampling-high dimensional model representation (RS-HDMR) which can deal with independent and dependent input feature variables is used to assess dominate discriminatory power and the reliability of feature which leads to an efficient feature selection. These feature selection results are compared in experiments with branch and bound method and with sequential forward selection (SFS), respectively. This work examines support vector machine (SVM) and Convolutional Neural Networks (LeNet5) in connection with white blood cell classification. Finally, white blood cell classification system is validated in experiments conducted on cytological images of normal poor quality blood smears. These experimental results are also assessed with ground truth manually obtained from medical experts.

Acknowledgments

First and foremost, I would like to thank my parents, for providing me with the opportunity to engage in this project. Without their support I may not have found myself at PhD study, nor had the courage to engage in this task and see it through. They are well aware how this project and my studies throughout my PhD years at Concordia University have formulated my outlook, determination, motivation and perspective that will sculpt my future. Through their and my siblings emotional support, intellectual stimulation and many hours of identity-forming conversation, I am inspired to pursue an unconventional dream in which I truly believe. So, thank you, to Mom, Dad, Pari and Hoshang, thank you Aida and Mohammad for being the most supportive family one could hope for. I will always appreciate all they have done, especially Raha for helping me develop my technology skills, Pouya, Zorena and Mehdi for the many hours of proofreading, and Ahad for helping me to master the leader dots. I dedicate this work and give special thanks to my friends for being there for me throughout the entire doctorate program. All of you have been my best cheerleaders. I would like to express my sincere acknowledgement in the support and help of my supervisors (Adam Krzyżak, Thomas Fevens) who tirelessly helped me to prepare this thesis.

Contents

List of Figures

List of Tables

Chapter 1

Thesis Introduction

1.1 Introduction

The examination of peripheral blood smears represents the cornerstone of hematologic diagnosis. Plainly, the examination of the peripheral blood smear is an important indicator of haematological and other abnormal conditions that affect the body of an organism. Blood cells are classified as erythrocytes (Red Blood Cells), leukocytes (White Blood Cells) or platelets (not considered real cells). The resultant count is the total number of erythrocytes and leukocytes expressed in a volume of blood. Expressing the number of white blood cells (WBC) carries many quantitative and informative clues. For example, the increase or decrease of leukocytes is very critical and may prompt detailed medical attention.

Automatic counting systems have been available in the medical laboratories for the last 30 years. The instruments used for performing cell counts are based on mix of mechanical, electronic and chemical approaches. The commonly used approach across biological disciplines and the ground truth is manual WBC counting and type sorting by a trained pathologist, looking at the shape, e.g, nucleus and cytoplasm, occlusion, and degree of contact between cells. Although the manual inspection method is adequate, it has *three* inevitable types of error: statistical, distributional and also human error [24] such as may happen in poor quality, low magnification view of the slides. Poor magnification and distribution of leukocytes adversely affect the accuracy of the differential count in manual counting.

Accordingly, since haematology is a visual science, machine learning and digital image processing have great potential to develop ways to improve haematology research. Computerized techniques are the best potential choices to carry out and moderate the load of these regular clinical activities for more efficiency and also to describe the frequency, spatial distribution, and portion of blood smear particles. Computer-aided diagnosis (CAD) also establish methods for accurate, robust and reproducible measurements of blood smear particles status while reducing human error and diminishing the cost of instruments and material used.

1.2 Introduction to Clinical Haematology

Haematology [139], a branch of pathology study, includes clinical laboratory, internal medicine, the blood-forming organs, coagulation and blood abnormalities that are summarized into blood studies. Bone marrow in the skull, ribs, sternum (breast bone), vertebral column (backbone), and bony pelvis is responsible to produce these micro bio-cells. White blood cells in bone marrow leukocytes are much denser than those in peripheral blood and just a small proportion of the produced white blood cells is circulated in blood vessels.

The main duty of red blood cells is to carry oxygen (O) to the body biological structures and absorb the carbon dioxide (CO_2) to exhale from the body using the respiratory system. Red blood cell transports nutritive significance, hormones, enzymes and vitamins through the body organs. Furthermore, one the other hand, white blood cells defend of the body organs using phagocytic activity mechanism to remove viruses, bacteria, cell debris (the dead or damaged tissue) and so on that cause disorder and damage in biological structures. In all mammals species including humans, normal erythrocytes posses biconcave disc shape without nucleus and are much less numerous than erythrocytes which predominate in blood. Leukocytes can be divided in two main categories: *granulocytes* and *lymphoid* cells. Neutrophil, Eosinophil (or acidophil) and Basophil are Granulocytes because of the presence of granules in the cytoplasm of WBC cells. So, granulocytes types are Neutrophil, Eosinophil (or acidophil) and Basophil. The lymphoid cells, consist of Lymphocytes and Monocytes (see Fig. 1).

In addition to RBCs & WBCs we have also platelets (PLT), or thrombocytes, that

enable clotting to stop the loss of blood from wounds. The platelets are round and small. Platelets are thin disks, 2-4 μm in diameter and 5-7 fL (fluid ounce that it is equivalent to 30 millilitres) in citrated blood volume. They play role in hemostasis, protect vascular integrity and they provide blood coagulation. Platelet counts are not often requested in a CBC test except for spontaneous bleeding where platelets play a key role in the blood test. In normal human blood, there are $4,000,000 - 6,000,000$, $4,000 - 11,000$, $150,000 - 450,000$ per microliter of RBC, WBC, and normal platelet, respectively, with platelets usually present in complexes rather than singularly.

To detect abnormal cells, CBC test is undertaken, which can detect abnormal immature blood cells (blasts), abnormal lymphocyte, immature granulocyte (IG) flags and nucleated RBC (nRBC) (see Fig. 4). Abnormal immature white blood cells are produced in the bone marrow and circulated into the bloodstream. These cells reproduce very rapidly and they are not considered as healthy white blood cells. Presence of these cells causes blood disorders such as acute myeloid leukaemia (AML) which is a cancer of blood-forming cells in the bone marrow. This is quite a serious health problem and prompt diagnosis and treatment are required.

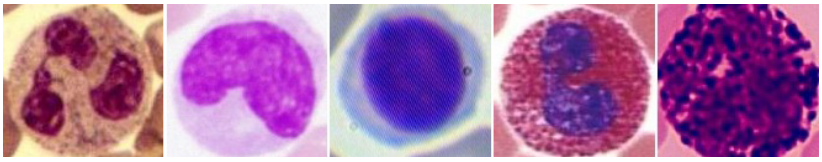

Figure 1: (Left to right): Neutrophil, Monocyte, Lymphocyte, Eosinophil, Basophil

1.2.1 Peripheral Blood Smear Examination

One of the highlighted areas of haematology research is the problem of determining blood cells (CBC) count and leukocyte (white blood cell) differential count (LDC). Complete blood count (CBC) is an informative comprehensive metabolic evaluation medical test which helps doctor and medical experts to check any symptoms and indicating a condition of disorders, such as weakness, fatigue, or, internal body problem, infection and many other diseases you may have.

A CBC test reports five key parameters: white blood cell (WBC) count, red blood cell (RBC) count, hemoglobin (HGB) value which gives color to red blood cells, hematocrit (Hct) value and platelet count in a pre-defined given volume of blood.

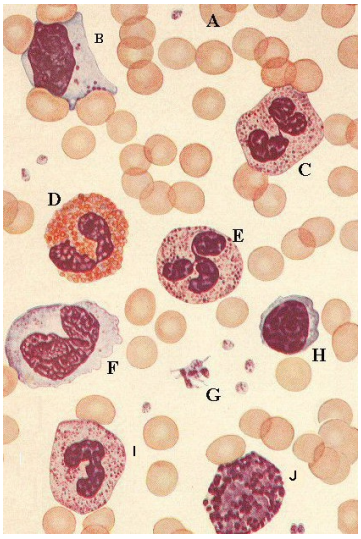

Figure 2: Cell types found in smears of Peripheral blood A)Erythrocyte; B)Lymphocyte; C)Neutrophil; D)Eosinophil; E)Neutrophil; F)Monocyte; G)Thrombocytes; H)Lymphocyte; I)Neutrophil; and J)Basophil.

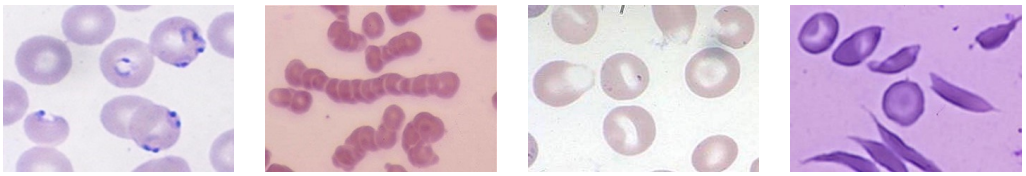

a b c d

Figure 3: Disorders: a) Malaria(P.f) b) Rouleaux, c) Pappenheimer and d) Sickle Cell-Anemia

The CBC measures the volume percentage (%) of red blood cells in blood, known as hematocrit (Hct) which is independent of body size in all mammal species. This Hct ratio may be expressed as a percentage or as a decimal fraction (SI units). Mean Cell Volume (MCV), is consequently calculated from the Hct and the erythrocyte count. MCV = Hct $\times \frac{1000}{RBC}$ (in millions per μL), expressed in femtoliters or cubic micrometers.

Another piece of information on the CBC result is red cell distribution width (RDW). The RDW is an expression of the RBC size distribution. It is computed and derived from the histogram and is the coefficient of variation, declared in percent of the red blood cell size distribution. When there is a large variation is size of red blood cells, two blood disorders may occur. Anisocytosis is a medical term meaning

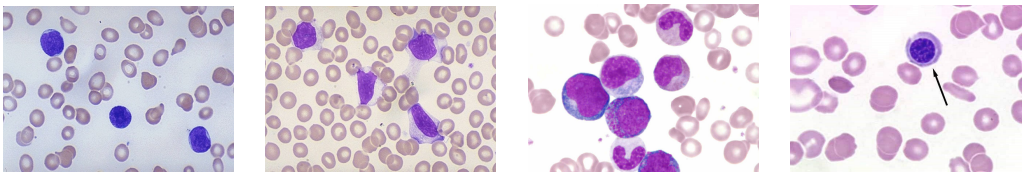

a b c d

Figure 4: Different abnormal cells: a) blast, b) abnormal lymphocyte, c) immature granulocyte (IG) and d) nucleated RBC (nRBC) [158, 236].

that RBCs are of unequal size. They are referred to as microcytes when red blood cells are abnormally small, and macrocytes when red cells are larger than normal. Significantly, in 95% of cases with iron deficiency, an incremental increase of RDW is observed.

The other medical concept that may be reported in CBC result is a significant variation in shape of red blood cells called Poikilocytosis. Any unusual shaped cell is a poikilocyte. Pear-shaped, oval, saddle-shaped, tear drop-shaped, and other irregular shaped cells may be seen in different blood disorders.

White blood cell counting and classification is an important result is CBC medical test. The number of WBCs many be indicative of many conditions. The leukocyte differential is the total number of WBCs expressed as thousands/μL in a volume of blood. There are five normal mature types of WBCs (with typical percentage of occurrence in normal blood): Basophil (<1%); Eosinophil (<5%); Monocyte (3-9%); Lymphocyte (25-35%); and Neutrophil (40- 75%) [183] (see Fig. 1). Other cell types observed in certain diseases are metamyelocyte, myelocyte, promyelocyte, myeloblast and erythroblast [183]. As a result, all the literature and studies mentioned have noted the importance of cell counting system to accomplish and achieve medical goals.

1.3 The Problem

The original benefit of this research lies in the development of an analysis software for CBC, as a tool for medical blood testing, which enables high quality tests and provides the capability of automatic processing of blood slide images to produce data necessary for diagnosis. This work focuses on normal blood smear samples. The objectives of this research are to determine whether the proposed image processing techniques are efficient in managing CBC test, particularly in presence of low quality

samples. We particularly interested in the classification of the five main types of white blood cells (leukocytes) and counting of normal red blood cells (erythrocytes) in a clinical setting.

For many medical topics, studies usually suffer from the fact that it is not easy to access large amounts of samples. Blood samples in this work were obtained from normal healthy patients. A total of 140 samples were obtained in cooperation with J.D. MacLean Centre for Tropical Diseases at McGill University in Montréal, Québec and also Ghods polyclinic medical center in Tehran, Iran. All samples are validated by MD Hematologist Doctor, Parvaneh Saberian and medical specialist, microbiologist, Aida Habibzadeh from Ghods polyclinic medical center in Tehran, Iran. Despite a small sample size, the dataset is generally representative of different conditions that may exist in a blood smear.

1.4 Thesis Structure

We discuss implementations of color conversion, de-noising, edge preserving and counting red blood cells as well as white blood cell classification. This work begins by laying out the theoretical dimensions of the research, and looks at how each step is involved in framework. Chapters describe the design, synthesis, characterization and evaluation of all details. The performance of proposed method is also compared with the state-of-the-art work.

The framework begins with interpretation of the peripheral blood smear (chapter 1, section 1.2. Next, this work gives a comprehensive overview of the recent history of red and white blood cell classification where each has its advantages and drawbacks. Background information were gathered from multiple sources between 1972 and 2014 (chapter 2). Chapters (3 - 7) begin by laying out the theoretical dimensions of the research step, and looks at how these methods are good at the complete blood count (CBC) results and interpretation. It describes the design, synthesis, characterization and evaluation of proposed framework. The section 8.1, in chapter 8 summarizes novel contributions of this thesis in the area of normal blood segmentation and classification. Also all parameters that should be manually set for each component are clarified in individual final section in each step. This clarification gives the reader a clear idea how this framework and could be applied successfully to a different data set. Chapter

8 includes conclusion and suggestion for future work. Some blood smear samples in different conditions are shown in the appendix (chapter 9).

This thesis made research contributions in five areas: pre-processing, binarization, cell separation, and feature extraction, and finally feature selection and classification.

Figures 5 and 6 demonstrate pipeline of the framework indicating what is the step used for each part. Figures 7 and 8 indicate the methodology used in each part.

1.4.1 Methodologies Used

On continuing discussion concerning the methodologies used (see Figures 7 and 8), the normal blood images are saved in JPEG format. Then a key step is to choose a proper gray scale channel to maintain the high and low frequency of components in a given blood image and white blood cells with special characteristics in particular. Distribution behaviours statistical approaches such as semi-IQR and variance are addressed to convert the blood smear images to a proper gray scale . In current dataset G channel rather than the other channels is selected (section 3.1). It also should be noted that other combination of channels such as Y and G might be even result better in Semi-IQR calculation and future work by other researcher could investigate in this matter. Secondly, the method used for denoising is based on the Bayesian non local mean. In a comparative study with other state-of-the art work Bayesian non local mean brings the highest PSNR value in presence of additive Gaussian noise (see Table 7). Thirdly, to build better boundaries for white blood cells and also to replace white blood cell internal heterogeneous parts by homogeneous neighbours, Kuwahara filter is addressed (see Fig. 16). Then, a binarization technique is introduced by merging the Otsu and Niblack methods (section 4). Area-Granulometry is used to estimate RBC size (see Fig. 23). Afterwards, the proposed Cell separation algorithm in an iterative mechanism based on morphological theory, saturation amount, RBC size, edged images and modified Chan-Vese active contours without edges is applied (section 4.3.3). A primary aim of this work is to introduce an accurate mechanism for RBCs counting. This is accomplished by using the immersion-based watershed algorithm which counts red cells separately (section 4.3.4). Next, white blood cells (leukocytes) classification into five major categories using invariant features such as shape, intensity and texture is addressed. Although diverse algorithms have been developed using well established mathematical theory, it remains comparably marginal

in computer-aided diagnosis (CAD) in medical imaging. In this work, features such as orthogonal invariant moments, dual-tree complex wavelet transform, run length are investigated (section 5). Before going further in feature selection a process can be considered as data compression that minimizes redundancy and preserves maximum relevance between features. The evaluation procedure deals with distribution functions in which method such as Kolmogorov - Smirnov, Wilcoxon- Mann-Whitney tests and also Pearson, Spearman and Kendall rank are addressed (section 5.6).

Further, to find a way to determine which of the features are actually worth extracting. The three different feature selection methods including global sensitivity analysis using Sobol index in random sampling-high dimensional model representation (RS-HDMR) expansion (section 6.1), forward sequential feature selection (section 6.2) with classifier interaction and also a branch and bound technique (section 6.3) using minimizing regression problem between features and WBC classes are addressed respectively. This work gives strong evidence that RS-HDMR merging Sobol global sensitivity analysis (section 6.1) is superior to other options in presence of different feature combination in varying datasets (see Table 21). Finally white blood cells recognition with a Support Vector Machine and initial appropriate settings for small dataset size (just only 28 samples per class) is addressed (section 7.2). This work also addresses Convolution Neural Networks to extract topological and receptive field properties from a given raw WBC image (section 7.1). The objective of CNN research in this case-study is to determine whether CNNs can be good predictors in blood classification with few available sample data. The results obtained from the preliminary analysis of white blood cell classification are presented in confusion matrices where this computerized framework is validated with experiments conducted on manual ground truth (sub-section 7.2.3).

Figure 5: Framework Pipeline: RBC segmentation and counting

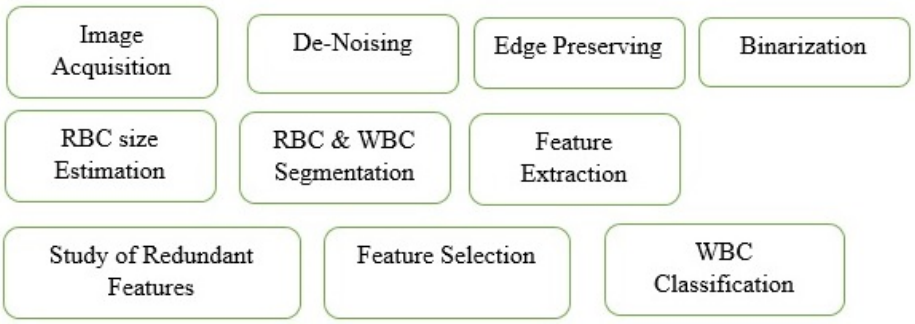

Figure 6: Framework Pipeline: White Blood Cell classification

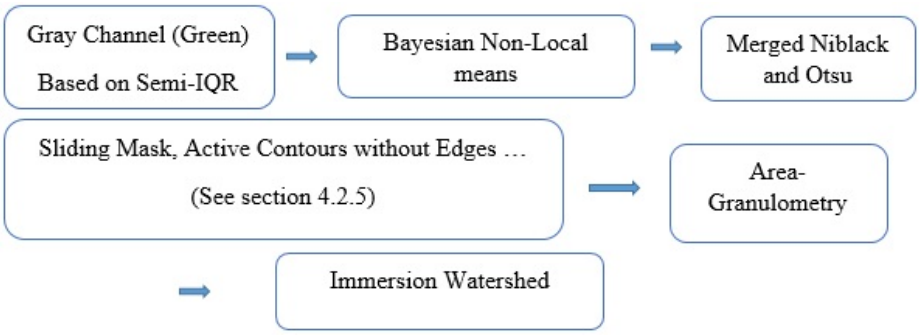

Figure 7: Framework Methods: RBC segmentation and counting

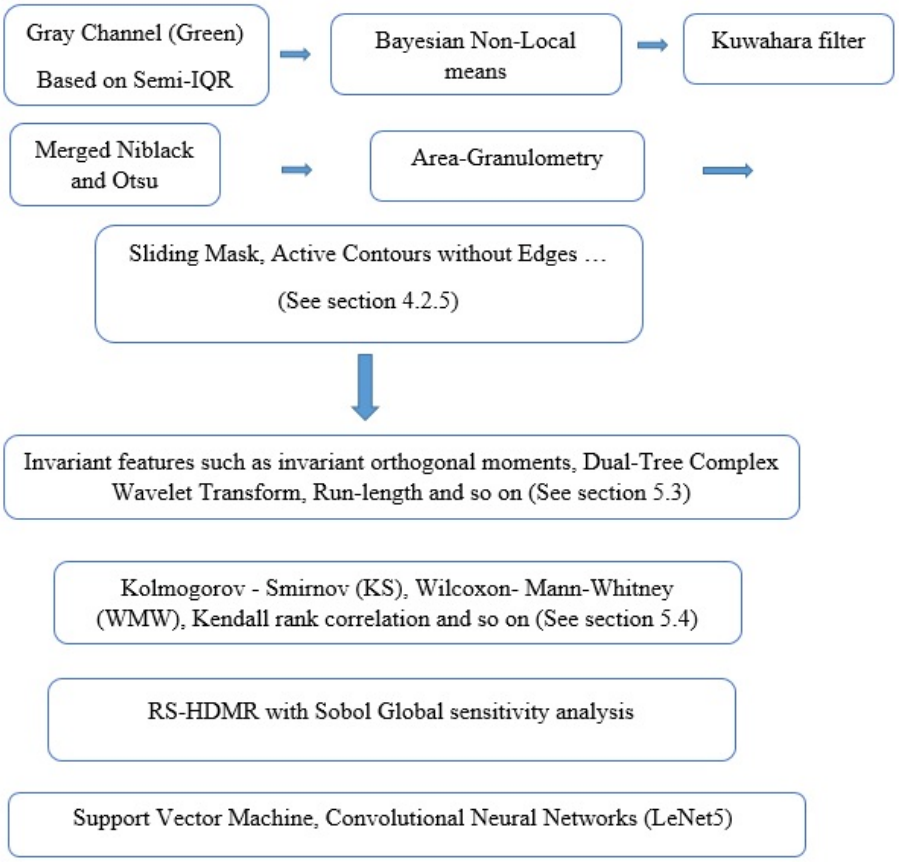

Figure 8: Framework Methods: White Blood Cell classification

Chapter 2

Literature Review on Detection of RBC and WBC

This chapter reviews CBC medical system and the literature concerning the usefulness of image processing and computer vision in connection with blood cells detection and haematology studies. This work first addresses modern CBC haematology systems and their history, and then reviews the research conducted on normal and abnormal blood samples. The objectives of this review are to gain insight into the state of the current work and to identify its shortfalls. The discussions and analyses of blood image processing that have been going on over the years give an overall sense that the generalizability of much of the published research on this issue is problematic. Although extensive research has been carried out in blood cell detection, too little attention has been paid to adequately cover different conditions and to quantify and qualify the association between image processing techniques and blood cell detection.

2.1 CBC Haematology Systems

Cell detection and segmentation in peripheral blood smear for clinical purpose goes back to more than one century ago in 1850 decades where professor Karl Vierordt, from the university of Tübingen in Germany who investigated and developed methods to monitor of blood circulation [238]. He introduced a Haemotachometer as an instrument to estimate the blood flow speed in main blood vessels which are called as arteries. Blood counting technique was addressed in his medical note series [238, 241].

Briefly, this research served as the base for future studies where obviously Vierordt work and findings added substantially to our understanding of blood circulation and haematology basic.

The design of the counting blood cells further developed based on research work by Cramer [37,238], Potain and Malassez and the other [134] in the middle 19th century. The research during the late 19th and early 20th century from different studies by Hayem [85] as a known French hematologist, and also the technique introduced by Oliver [159] an English physician made several contributions to the current literature.

A rapid change is made in the twenties, as a result of the development in photoelectric methods. During years, different electronic counting systems with flow of electrical current and based on conduction were introduced [238]. Since the last 25 years automatic counting system have been available in the medical laboratories with the less and more similar structure [24]. The instruments used to perform cell counts are based on mix of mechanical, electronic and chemical approaches. They are made on the principles of electrical impedance, radio-frequency conductivity, light scattering, and/or cytochemistry. With electrical impedance, blood cells passing through an valve and aperture which a current is flowing cause changes in electrical resistance to provide voltage pulses. In an updated electrical impedance technique red blood cell size distributions automatically will be plotted. In radio-frequency conductivity technique, using a high-frequency electromagnetic probe information on the cell internal structure will be provided by spreading or flowing throughout the fat layer of a blood cells membrane. In the electro-optical method, size of the particle (WBC, RBC, or platelet) is determined by light scattering. Forward angle scatter of a light determines cell surface characteristics and measurement of beam scatter at multiple light angles to differentiate of cell types. In cytochemistry analysis, cytochemical reaction used to detect white blood cells. This method usually works along with electro-optical and data derived from light scattered to aid white blood cell differentiation [24].

2.1.1 Current CBC Systems

Current hematology analyzers used routinely in modern medical laboratories are such as Sysmex XE-series [197] and also Abbott CELL-DYN [69]. The Abbott Cell-Dyn 4000 hematology analyzer integrates four measurement sub-system to accomplish almost a complete CBC medical test. This system works with fluorescence flow

cytometry technique, where argon ion lasers with emitting at 13 wavelengths through the visible, ultraviolet, and near-visible spectrum are also used for nucleated immature RBCs. Hemoglobin (HGB) value is determined using spectrophotometry in which RBC and platelet counts are done by impedance and optical methods, respectively. Product information is available in table 1.

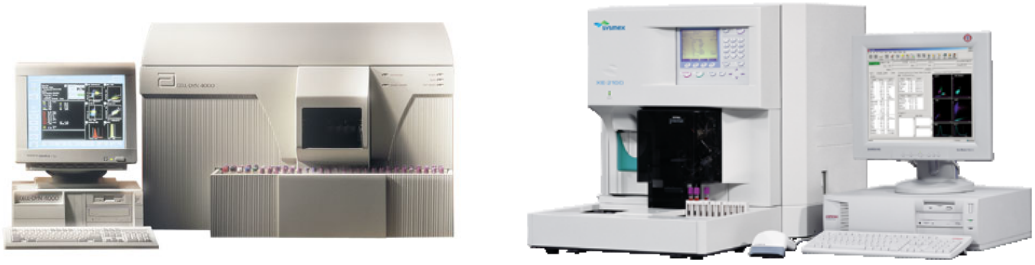

a b

Figure 9: Hematology analyzers: a) Abbott Cell-Dyn 4000, b) Sysmex XE-2100

Sysmex XE-2100 is based on fluorescent flow cytometry and hydrodynamic focusing methodologies to manage CBC test procedure when multiple flows with significantly different flow rates come into contact. Sysmex XE-2100 is enable differentiate normal red blood cell, white blood cell and platelet populations with minimum manual interventions. Generic system specifications is in table 2.

These known systems in white blood cell differential count reveal good correlation with the manual ground truth reference analysis for Neutrophils, Lymphocytes, and Eosinophils (r =0.925, 0.922, and 0.877, respectively) and enough fair for Monocytes and Basophils (r =0.756 and 0.763, respectively). Commonly used approach across biological disciplines and ground truth includes manual WBC counting and type sorting by a trained pathologist and skilled haematology expert, looking at the shape, e.g, nucleus and cytoplasm, occlusion and degree of contact. This manual WBC counting method is based on the count of 100 cells by moving back and forth across the blood smear in a pattern to cover different angle view under the microscope.

Poor magnification and distribution of leukocytes adversely affect the accuracy of the differential count in manual counting. These medical conventional method,

therefore, suffer from imprecision, and poor clinical setting. In other hand, the erythrocytes and leukocyte types that the current equipments are able to manage are restricted to some classes where always update of these systems are based on expensive chemicals and mechanical process [175]. As mentioned, the microscope inspection of blood slides provides important qualitative and quantitative information concerning the presence of hematic pathologies [173], however the number of different sub-cell types that can come out especially for WBC count is relatively large and typically more than 20 [175]. A systematic method and meticulous technique to derive all accurate and consistent cell information from each blood smear examine is highly required. These comprehensive blood studies increase the difficulty in building a feasible hardware based system. Overall, it can be seen that the majority of blood diseases can be detected using image processing and computer vision techniques.

Table 1: Abbott Cell-Dyn 4000: Generic specifications and availability [69]

Abbott Cell-Dyn 4000 Hematology Analyzer	
Manufacturer:	Abbott Diagnostics
Type	Hematology Analyzer
Parameters:	41: 5-pt Differential
Throughput:	106 samples/hour
Method:	Volume Impedance
Open system:	Open
W × D × H:	43× 32× 29 inches / 109× 81× 74 cm
Weight:	326 lbs / 148 kilos

Table 2: Sysmex XE-2100 Specifications

Sysmex XE-2100 Hematology Analyzer	
Manufacturer:	Sysmex Corporation
Type	Hematology System
Parameters:	31: 5-pt Differential
Throughput:	150 samples/hour
Method:	Fluorescent Flow Cytometry:
Configuration:	Standalone Sysmex HST-N, AlphaN Automation
W × D × H:	27.8 × 35.9 × 28 inches / 178 lbs
Weight:	178 lbs / 80.7 kilos

2.2 The Literature on Image Processing in CBC

CBC process can be automated by computerized techniques which are more reliable and economic. Therefore there is always a need for the development of systems to provide assistance to haematologists and to relieve the physician of drudgery or repetitive work. Computer-aided diagnosis (CAD) will establish methods for precise, accurate, robust and reproducible measurements of blood smear particles status while reducing human error and diminish the cost of instruments and material used. Afterwards, software provides the capabilities of upgrading and measurement variability without major changes and extra burdens.

The computerized steps into automated blood examination refers to a work done by Bentley and Lewis [14] in 1975. In this early work, authors used of colour information analysis to obtain integrated data on erythrocytes size in a numbers of normal and abnormal red blood cells. This paper went after to address the correlation between MCV (mean corpuscular volume) refers to the size of erythrocyte and MCH (mean corpuscular hemoglobin) refers to the concentration of hemoglobin in red blood cells. One decade after, the first fully automated processing of blood smear slides was introduced by Rowan [195] in 1986. Further related references are listed in below sections.

2.2.1 Literature Review on Segmentation

Initial success on segmentation of medical imaging and blood segmentation was obtained with graph theory (Martelli [138], Osowski *et al.* [163], Fleagle *et al.* [58, 59]) which was used to navigate around edge pixels in an available image. However this approach has involved images of single objects manually located in an image. Further, it does not address the problems of multiple objects in the image. Therefore, object location, removal of extraneous edges (internal to the cell), or the selection of suitable starting and ending points for the graph search are the initial steps which are should considered. These arguments rely too heavily on quantitative analysis of manual aforementioned pre-processing steps where it is always an inconsistency with this argument. There is no consensus among researchers regarding what method can be applied for different conditions, and there is no general agreement about these initial steps.

Due to complexity of the problem at hand some of the papers are limited to image-based comparisons based on red cells segmented either manually, see Bentley & Lewis [14], Albertini *et al.* [3], or semi-automatically, see Robinson *et al.* [192], Costin *et al.* [35] and Gering & Atkinson [66]. Dong *et al.* [48] proposed a framework with three steps to identify rolling leukocytes in microscopic images. This work profits gradient inverse coefficients of variation (GICOV) to discriminate leukocytes in-vivo environment. Authors first build a set of arbitrary number of ellipses by varying radii and orientation. Local maximum in gradient inverse coefficients of varying value denote presence of white blood cell in a close-by ellipse area where ellipses corresponding to locally maximum GICOV will be relaxed to flexible contours by active B-spline curves. Rathore *et al.* [184] used a method to estimate circularity ratio of cells. Counting is also done using watershed segmentation and Pixcavator student edition software. Lepcha *et al.* [122] segmented and counted number of red blood cells using integration of marker controlled watershed segmentation and morphological operations. Khajehpour *et al.* [71] introduced a line operator and watershed algorithm to segment red blood cells. The line operator with 20 line segments in various directions over a global Otsu threshold image has been applied. Wei *et al.* [246] first employed a K-means classification to detect of leukocyte and then counting RBC was addressed using watershed.

Literature Review on Thresholding

Adjouadi *et al.* [1] used eight-directional scanning to detect the red blood cell boundaries over the thresholded binarized input images. This work examined clustering-based image thresholding to segment cells. One major criticism of Adjouadi's work is that it relies heavily on initial conditions in a given blood smear slide. It used global thresholding and then the existing framework fails to resolve the thresholding problem in presence of different possible staining. There is no general agreement about all possible cells.

2.2.2 Literature Review on White Blood Cell Detection

To go further in discussion and to interpret health changes accurately, practitioners must get knowledge of a complete white blood cell five-part differential. The background on white blood cell classification using computer vision concepts is very vast

and it involves feature extractors, classifiers, quantitative and qualitative process, e.g., [51, 183, 189, 208, 228]. The first paper on blood processing is leukocyte pattern recognition by Bacusmber and Gose in 1972 [11]. In this primary work, classification of white blood cells using shape features and a multivariate Gaussian classifier into their categories are presented. In 1986, the first fully automated processing of blood smear slides was introduced by Rowan [195] .

Active contour model background

Active contour model, or snake is an another common method of boundary detection [99]. In 2001, Ongun *et al.* published a paper [160, 162] in which they described how active contour models facilitate white blood cell edge and boundaries detection. In other work [160], active contours were also used to track the boundaries of white blood cell where occluded cells were not accurately handled. A computerized system where cells are segmented using active contour models was introduced in [161] using shape features and textures for classification. WBC classification in 2009 by Hamghalam *et al.* [80] utilizes Otsu's thresholding method to nuclei segmentation. The results are claimed independent of the intensity differences in Giemsa-stained images of peripheral blood smear and active contours are used to extract precise boundary of cytoplasm but in simulation it failed in different condition. Mukherjee *et al.* [148] proposed a leukocyte detection framework with image-level sets computed via threshold decomposition. An evolution of a level-set curve that maximizes image gradient along homogeneous region was considered as cell boundaries. In general, despite active contour model efficacy in deformed cells, this method is not fully automatic. This method relies on initial positioning for snake algorithms and to date, little evidence has been found associating active contour model with full automated system. It is very obvious that with wrong initial model positioning, boundaries are also tracked negatively.

Fuzzy logic background

Sobrevilla *et al.* [215] used fuzzy logic to segment white blood cells from a digital blood smear image. In that proposed fuzzy logic two regions were segmented; one was the interest region, which contained leukocytes and other part included stained backgrounds with light gray level homogeneous texture, erythrocytes with light-medium

gray level and lastly, it also included the contours of white blood cells in correspondence with heterogeneous areas. In this way both intensity level, homogeneity and heterogeneity taken into account to distinguish between white blood cells and other particles in digital image. However, in both TSMM [252] and fuzzy logic [215], parameter settings were needed to set by statistics and experience. Also, it was limited to very obvious differences among backgrounds, red blood cells, and white blood cells in correspondence with homogeneous areas. Hence, both frameworks fail in different conditions such as color conversion and varying illumination staining inconsistency. Afterwards, Shitong *et al.* [208] proposed white blood cell detection based on fuzzy cellular neural networks (FCNN). FCNN is a hybrid system of fuzzy logic and neural networks (NNs). Experimental results showed that the mentioned detailed approach performance was more efficient than the other comparative methods in paper including TSMM [252] and fuzzy logic approach [215]. This method [208] took advantage of neural network classification and regression performance, combination of Neural Network and fuzzy logic facilitated Classification in uncertain condition in cell pattern recognition.

Morphological changes background

Lezoray [123] introduced region-based white blood cells segmentation using extracted markers (or seeds). However, this method required prior knowledge of color information for proper seed extraction. Kumar [114] applied a novel cell edge detector while trying to perfectly determine the boundary of the nucleus. Furthermore, in other work, WBC segmentation was achieved by means of mean-shift-based color segmentation in Comaniciu and Meer research work [34] while in [95] Jiang *et al.* used watershed segmentation. In other work, in order to improve the segmentation of touching or adjacent blood cells, conventional and typical wavelet transformation combined with morphological operations was proposed in Chan and his co-authors work [28]. Yang *et al.* [255] used a combination of RGB and HSI to describe color space in white blood cell. This work detect white blood cell with gathering color information in Saturation (from HSI) and Blue (from RGB) channels.

Feature Extraction background

Ramoser *et al.* [183] used hue, saturation and luminance values to locate WBCs. Then it goes on classification using a 26-dimensional color feature vector and a polynomial support vector machine (SVM). However, this proposed framework [183] did not address different conditions in camera settings, magnification, varying inconsistent illumination and blood staining. It also ignored texture features that they may produce appropriate space and proper meaningful output to object recognition due to authors false assumption about size and texture feature computation. Xiao-min *et al.* [252] introduced method based on threshold segmentation followed by mathematical morphology (TSMM). In that work binary threshold segmentation was in the first step. The individual white blood cells were detected using the average gray value of cytoplasm as the threshold and then binary segmentation was done; also it was calibrated with erosion and dilation applied to the binary image, where number of morphological operations was assigned by experience. Following that, the WBC nuclei was located with the shape features in correspondence with area and roundness.

Bikhet *et al.* [18] used 10 features from cytoplasm region to classify five main white blood cell types. This work extracts features after initial edge detection that surround white blood cell nucleus and its cytoplasm. Following that, there is an inconsistency with this argument. It suffers from different issues such as using median filter as a denoising is not a reliable selection. In addition, edge information and image contours are very problematic in varying dataset.

Other than that, Theera-Umpon *et al.* [228] used four white blood cell nucleus features and Bayes and artificial neural network were also proposed as classifiers. The first two features were first and second granulometric moments of the pattern spectrum in which the area of the nucleus and the location of its pattern spectrum peak were the other two candidate features. In that work, Bayesian classifiers is based on normal conditional probability density with equal prior class probabilities $P(C_k)$ for each class. Neural Networks empirically set one hidden layer including five hidden neurons in order to satisfy the fast convergence.

Sinha and Ramakrishnan [213] suggested a two-step segmentation framework using k-means clustering of the data mapped to HSV color space and a neural network classifier using shape, color and texture features. Ramesh *et al.* [38] proposed a two-step framework; segmentation and classification of normal white blood cells in

peripheral blood smears. Colour information and morphological processing were basis functions for segmentation part which was almost close to already our published paper in [78]. Latter, WBC classification followed using 19 features such as area, perimeter, convex area, and so on. To lessen the computational burden, fishers linear discriminant (FLD) to trim multi-dimensional set to six dimensions was also applied. Following that, linear discriminant analysis (LDA) to separate these five classes of WBCs was used.

Ko *et al.* [106] addressed a combination of shape, intensity, and texture features with 71 dimensions over a segmented nucleus. These descriptors are variant such as area, perimeter, the number of nuclei. This argument relies too heavily on qualitative analysis of blood slides and the existing accounts fail to resolve cell discrimination with different quality.

Rezatofighi *et al.* [189] described the blood segmentation, feature extraction and evaluation of five main white blood cell classification. This work assessed segmentation using GramSchmidt orthogonalization method along with a snake algorithm to segment cells elements into nucleus and cytoplasm. Next, feature vector was made of nucleus and cytoplasm area, nucleus perimeter, number of separated parts of nucleus, mean, variance of nucleus and cytoplasm boundaries, co-occurrence matrix and also local binary patterns (LBP) measures. Finally, this paper begun by feature selection using sequential forward selection (SFS). It then went on to compare performances of two classifiers; multi-layer perceptron (MLP) and support vector machine (SVM) with Gaussian kernel function. In more recent work (2012) Dorini *et al.* [51] introduced automatic differential cell system in two levels to segment WBC nucleus and identify the cytoplasm region. The image pre-processing with self-dual multi-scale morphological toggle (SMMT) filter along with scaled erosion and dilation morphological operations to improve the correctness and performance of two known segmentation approaches using watershed transformation and level sets was applied. In addition, further, cell cytoplasm region was separated by using gray scale mathematical morphology granulometry. In that work five mature WBC types were classified using a K-Nearest Neighbor (K-NN) classifier with geometrical shape features and a reasonable accuracy (78% performance vs 85% classified manually by a specialist) was achieved.

2.3 Motivation for a Computerized System

As a result, despite its long history in cell classification (see Section 2.2), questions have been raised about the reliability, generality and steps selection in an appropriate blood cell classification system. On the other hand, one major drawback of these aforementioned approaches is that no general attempt was made to quantify the association between low resolution cell appearance and their classification. Therefore, this current work would have been more convincing if the framework considers these concerns.

This work represents an effort towards automating the blood testing system, with general steps concerning color selection, de-noising, edge preserving, and binarization. This work seeks to take advantage of invariant features to maintain better local characteristics. Moreover, it seeks to address the redundancy and the distribution behaviour of features. It also investigates better feature selection strategy to enable a smaller effective feature vector. It assess the degree of importance and the reliability of each individual feature in presence of high dimensional data. More details concerning the contribution to the body of knowledge are found in section 8.1.

Chapter 3

Blood Smear Image Enhancement

Image quality can interfere with the cell border tracking and local information. Therefore, image pre-processing is an important phase of the segmentation procedure. It includes steps to capture a digital image and then remove Gaussian noise of blood smear. It also includes enhancement techniques of image smoothing, edge preserving, and background subtraction, which allow more efficient data analysis. In this chapter, the importance of each pre-processing procedure is highlighted through in-depth analysis.

3.1 Blood Image Pre-Processing

Image acquisition is the action of retrieving raw images from a capturing source, usually a digital camera. Storing raw files into computerized image format as we have all experienced, is an inseparable part of camera shots. Different electronic file formats are available for images. Each format stores the image in a specific way. The most common image file formats found are: Graphics Interchange Format(.GIF), Joint Photographic Experts Group (.JPG), Portable Network Graphics (.PNG) Bit-Map (.BMP), Tagged Image File Format (.TIFF or .TIF). Digital images can be converted to different computer graphics color spaces where there is a number of ways including such as RGB (Red Green Blue), CMY(K)(Cyan Magenta Yellow (Black)), HSL (Hue Saturation and Lightness), YIQ (Luminance (Y), In-phase Quadrature (NTSC color space)), YUV (Luminance (Y), blue luminance (U), red luminance (V) (SECAM and PAL color spaces)), YCbCr (Luminance(Y), Chrominance information for blue and

red components (Cb and Cr)), YCC (Luminance - Chrominance) and CIE (CIELuv and CIELab). Further details regarding file format differences are beyond the scope of this research.

Today, cutting-edge digital microscopy cameras equipped with image sensors are available in few modern medical research centres. However, the objective of this research is to enable analysis of relatively small, low resolution degraded images and to provide a frame work which can be effective in different circumstances, including inexpensive, basic digital cameras. It should also be noted that, even with professional digital camera, improper camera set-up may result in very low quality images, and this research is aimed at enabling analysis of such images. Our framework should address image enhancement such as de-noising and edge preserving to maintain local required information to detect cells. Our work operates with single-frame blood images, where single shots can be joined together to closely stimulate all observations through a microscope.

3.1.1 Problem Statement

To design a reliable system that may be used under different conditions such as different blood staining techniques, types of chemical materials used, microscope types, illumination conditions, human factor, a pre-processing step is required.

Colour map conversion is a key step, especially in presence of white blood cells where their shapes are not entirely convex. White blood cell includes cytoplasm whose texture; membrane, nucleus is non-uniform staining and it is found in granular. According to staining, different types of image acquisition, illumination, position of blood cells (overlapping and very closely positioned particles), intrinsic properties of cells (e.g., Leukocytes characterized by the presence of cytoplasm when viewed under light microscopy) and other conditions such these, it is very common that acquired images have blood cells which are close to background color and cells separation is always questionable.

Secondly, noise removal helps to stabilize the next steps to achieve accurate localizations or parametric estimations [168]. All medical and clinical images may contain some visual noise from a variety of sources however noise is much more prevalent in certain types of imaging than others such as magnetic resonance imaging (MRI),

computerized tomography (CT), and ultrasound imaging (sonography), while radiography produces images with the least amount of noise [217].

Thirdly, pre-processing is continued by edge enhancement in presence of white blood cell. Edge preserving maintains better white blood cell boundaries appearance. So, therefore edge sharpening with an enhancement filter that moderates and lessens these effects will yield superior segmentation results. On the other hand, all minor visible color spectrum are not required even though they are burden to system and increase complexity. Providing an overall painting-style look removes internal color spectrum detail as well as it increases sharpness of cell edges as compared to photo realistic images. It facilitates to get an effective visual appearance and it would be a proper step prior feature extraction. Consequently, on completion of pre-processing, the process of edge preserving and image abstraction from white blood cell blood images is achieved using edge-preserving filters.

3.1.2 Literature Review

Colour Selection:

Some previous published work used the *green* channel of the RGB color encoding to analysis blood image data [45, 107, 133, 141]. Also it can be seen that white blood cell granular cytoplasm pixels can be highlighted better in the image histogram of the green channel [242]. A number of other color spaces rather than RGB have been addressed in literature for different specific purposes. Several attempts have been made to use gray scale intensity of colourful JPEG blood smear images [71, 144, 173, 198, 262]. For example, authors in [144] suggested to use L$\star$ a$\star$ b$\star$ color model for reduced color feature. In addition, in study [81] using HSI color space is recommended to extracting leukocyte nucleus. Authors in [263] used combining B from RGB and Y component from CMYK color spaces to have more contrast in presence of white blood cells.

Noise Removal:

Many efforts have been devoted to reducing this undesired effect. Wavelet shrinkage is a signal de-noising technique based on the idea of thresholding the wavelet coefficients of an image. One of the most practical and widely used de-noising technique is wavelet

shrinkage approach which thresholds the wavelet coefficients of an image. Removing the small coefficients and then reconstructing the signal could produce signal with lesser amount of noise. The biggest challenge in the wavelet shrinkage approach is finding an appropriate threshold value [60].

Sendur *et al.* [204, 205] introduced Bivariate wavelet shrinkage functions. Authors used Bivariate shrinkage function based on Daubechies wavelets. In most non-linear thresholding wavelet-based methods it is supposed that the wavelet coefficients are independent when coefficients of natural images have significant dependencies. The bivariate shrinkage functions consider the dependencies between the coefficients and their parents in detail of wavelet function. The bivariate estimates of wavelet coefficients with non-gaussian Bayesian models to characterize the dependency between parent points and their children at the same spatial position.

In paper [177], a speckle noise reduction algorithm using wavelet approach over the logarithm of various medical ultrasound images is used. Yu *et al.* [259] proposed an algorithm for Gaussian noise reduction from degraded medical images using a wavelet-based trivariate shrinkage filter with a spatial-based joint bilateral filter.

Chen *et al.* [31] developed wavelet de-noising method with neighbor dependency. This method used a modified thresholding in a given windows size for different wavelet coefficient sub-bands independently. This method could maintain minor important details for a given small windows (i,e. 3×3). Pizurica *et al.* [174] proposed a wavelet domain de-noising method using estimation of the probability that a given wavelet coefficient is a significant noise-free component. This method introduced a novel threshold function, which shrinks each coefficient according to probability that it presents a signal of interest which is free of noise.

Fischer *et al.* [57] proposed a de-noising method with combination of localized oriented Gabor filters, Fourier and wavelet transforms. This combination preserves local details in poor orientations by such multi resolution wavelet transforms.

Coupè *et al.* [36] introduced an improved non-local means filter for image de-noising. This method changes a noisy pixel value by the weighted average of other local neighbourhood pixels with weights reflecting the similarity between this pixel and the other pixels. This approach updates Bayesian parameters directly by the noise variance given the patch size.

Dengwen *et al.* [42] introduced an optimal threshold for every sub band by Steins

unbiased risk estimate (SURE) in a given neighboring window size. This method profits from dual-tree complex wavelet transform (DT-CWT) as a shrinkage function to alleviate redundant problem in typical wavelet.

In [265], Gaussian process regression (GPR), to detect edges with more detailed information is addressed. In paper [17] computed tomography (CT) images have been de-noised with combination of total variation (TV) and curve-let based methods. The edged image is extracted from the left noise of TV algorithm by processing it through curve-let transform.

Manjón *et al.* [136] first decomposes the signal into the local principal components, then it shrinks the less relevant components, and lastly signal is reconstructed as a free noise signal. The intuitive idea is that image can be represented as a linear combination of a small number of basis images while the noise, being not sparse will be spread over all available components. In a similar work image de-noising with patch based PCA (local versus global) is also investigated. Deledalle *et al.* [27] introduced three patch based de-noising algorithms which applied hard thresholding on the coefficients. The algorithms differ by the methodology of learning the dictionary: local PCA, hierarchical PCA and global PCA. Salmon *et al.* [199] takes advantage of over-complete dictionaries combined with sparse learning techniques. This method adapts a generalization of the PCA for de-noising degraded images by Poisson noise.

In terms of blood cell detection, in work [44] median filter is used to de-noise blood microscopic images. Other work [135] proposed de-noising and blood image enhancement by inter-scale orthogonal wavelet based threshold which is based on stains unbiased risk estimator (SURE) approach.

Edge Preserving:

Further, concerning edge enhancement, as mentioned in the literature review [72] (see Fig. 16), linear and non-linear filters which are appropriate candidates to smooth heterogeneous white blood cell areas.

Edge preserving is achieved by applying the following filters: convolution kernel filter [10], symmetrical nearest neighbour filter [84], bilateral filter [231] and Kuwahara filter [115, 167].

Bilateral filtering [231] is a simple, non-iterative and non-linear combination of nearby image values to perform edge-preserving smoothing. As it can been seen

from Bilateral filtering, two points are closeby pixels in which they are neighbours in a spatial location, or they are close to one another in intensity values. This filter considers similarity in geometric and photometric locality. This filter replaces the value at x location with an average of similar pixel values. As a consequence, when the bilateral filter is applied of the boundary, the bright pixel is replaced at the center by an average of the bright pixels in its adjacent and nearby region, and it ignores the dark pixels. It also reversely centred on a dark pixel then the bright pixels are ignored instead. Finally, with using these steps image edges are preserved in some extent. Symmetrical nearest neighbour (SNN) is based on distance measurement. This filter compares symmetric 4-connected surrounded pixels in four directions (N-S, W-E, NW-SE and NE-SW) with the center pixel and it only considers the pixel from each paired set which is the closest to the center pixel value.

3.2 Research & Experimental Results

The prepared database (140 samples of five types) includes images of different conditions for a sample referring to fig. 10. When images of blood smear have been capturing, they are saved in JPEG (less computational requirements)format with 512 $\times$ 512 resolution. The calculation (see sub-section 3.2.1) shows that using the G (green) channel is the best choice for converting the current blood smear images to gray scale. Furthermore, the study examines the efficiency of Bayesian non local mean de-noising technique in order to enhance cytological input images. After extensive experimenting, the Kuwahara filter as a non-linear smoothing filter is chosen in this study to smooth and preserve the white blood cell edges.

3.2.1 Colour Scale Channel

Computational outcomes have shown the adequate discrimination is achieved using the "Green" color channel [72]. It is obvious that Y channel is also an appropriate alternative in case (see Table 4). Green encoding is better at maintaining high frequency feature information [72].

Experiments on a set of *10* sample (different image characteristic (see Table 13) blood smear images show that the green channel has a wider range of gray-level values in the intensity histogram than the red and blue channels and thus keeps more

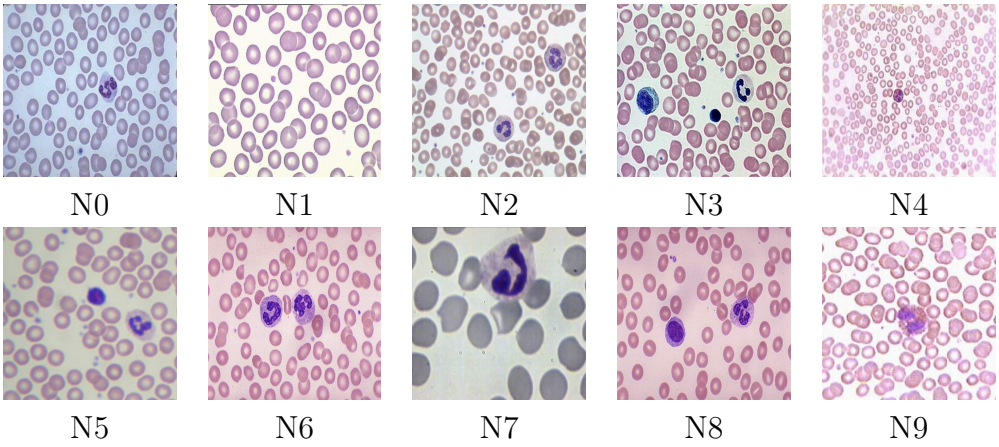

Figure 10: Normal blood smear images with different characteristics (N0–N9)

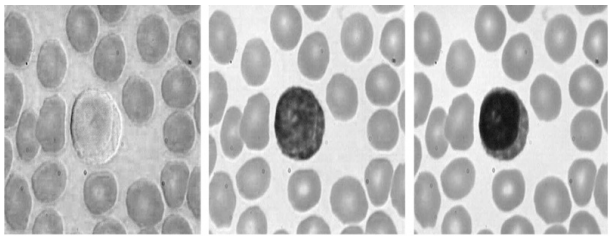

Figure 11: (Left to right): Blue, Red, and Green channels.

feature detail. The G channel generally has the highest contrast between structures even in the presence of different backgrounds (e.g., different staining and/or different techniques for capturing images) as compared to the red and blue channels. Gray-level distributions of three RGB channels for a sample image are shown in fig. 12.

The variance of a data set corresponds to how far the values are spread out from each other. We can validate better resolution of G channel by considering the variance of the different three RGB channels over the 10 sample images with different noise characteristics. Table 5 shows the details of the images and their corresponding variances. Clearly, the variance is the highest for the G channel. Other than that we could also test the efficiency of color encoding by some other statistical approaches. In blood smear images there are particles such as white blood cells which include granular cytoplasm which contain very high frequency components in very narrow and close-by range in blood smear histogram.

It means the spread and dispersion of skewed distributed variables can play a great role to keep the details of image characteristics. The quality of different color encoding

Table 3: Percentile range for different color map in different conditions: (top to down: a, b, c); a) total over 10 regular images (N_0–N_9, whose characteristics are described in figure 10); b) total over same 10 images with moderate noise and c) same 10 images with high noise

	10 Normal images		
Channel	25_{th} **Percentile**	75_{th} **Percentile**	**Semi-IQR**
Red	166	234	34
Green	159	237	34
Blue	178	215	19
	10 Additive medium noisy images		
Channel	25_{th} **Percentile**	75_{th} **Percentile**	**Semi-IQR**
Red	210	251	21
Green	168	241	21
Blue	193	248	18
	10 Additive high noisy images		
Channel	25_{th} **Percentile**	75_{th} **Percentile**	**Semi-IQR**
Red	188	255	34
Green	155	252	34
Blue	195	255	30

can be measured by percentile ranges along with mean and standard deviation. The most common of these is the interquartile range, which is a measure of variability and computed as one half the difference between the 75_{th} percentile ($Q3$) and the 25_{th} percentile ($Q1$). As we expect to have more details and variety in high frequency range we can use the formula for semi-interquartile range $(Q3 - Q1)/2$ as a good measure of spread for skewed distributions.

Besides the RGB and HSI color space, we also consider the YIQ color space. YIQ encods two kinds of information: luminance (Y) and color information (I and Q). The main reason for using YIQ is the sensitivity of human visual system which is more aware of changes in luminance than to changes in hue or saturation and thus a wider bandwidth should be dedicated to luminance than to color information. So, we compare the Y channel with the G channel of the RGB color space. Since with YIQ encoding wide bandwidth is dedicated to Y, opacity and clearance of object in Y channel is expected to be comparable with G channel (see Fig. 13). As a result, calculations prove that the best choice for converting the blood smear images to gray scale is to use the G (green) channel of the RGB encoding, or the (Y) channel of YIQ channel encoding. Figure. 14 and table 6 show that higher semi-interquartile range

Table 4: Percentile range for Y (YIQ) and G (RGB) color map in different conditions: (top to down: a, b, c); a) total over 10 regular images (N0–N9, whose characteristics are described in figure 10); b) total over same 10 images with moderate noise and c) same 10 images with high noise

	10 Normal images		
Channel	25_{th} **Percentile**	75_{th} **Percentile**	**Semi-IQR**
Y	159	235	33
G	159	237	34
	10 Additive medium noisy images		
Channel	25_{th} **Percentile**	75_{th} **Percentile**	**Semi-IQR**
Y	168	241	21
G	168	241	21
	10 Additive high noisy images		
Channel	25_{th} **Percentile**	75_{th} **Percentile**	**Semi-IQR**
Y	155	252	34
G	155	252	34

belongs to (green) channel in RGB color-map.

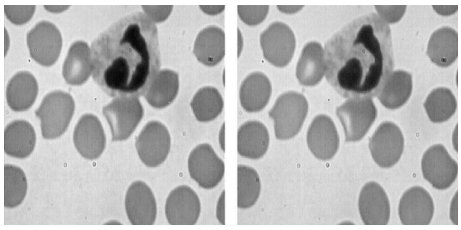

Figure 13: Left to right: G channel (RGB encoding), Y Channel (YIQ encoding)

Experiments with the same 10 sample blood smear images again show that the G channel has a wider range of gray-level values in comparison with Y Channel outcome, see Fig. 14. In addition, the variance is highest for the G channel (see Table 6). However, combination of different channels may result higher variance as well and of-course user could profit varying combinations.

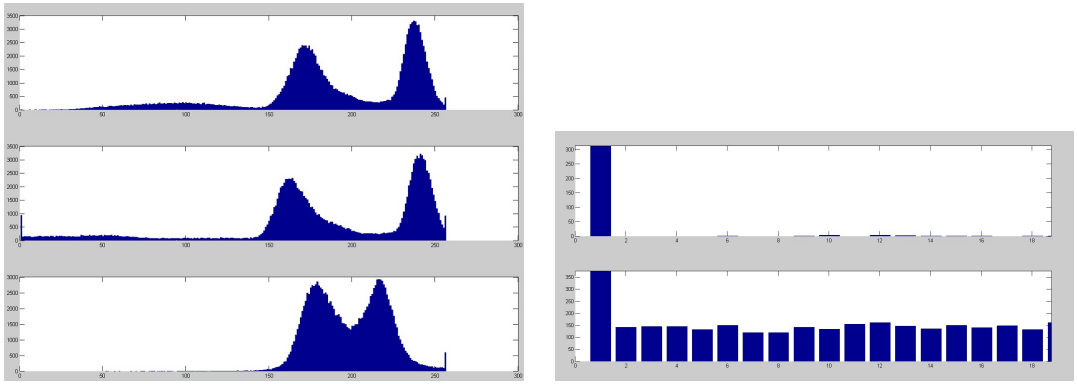

a b

Figure 12: a) Gray scale distribution (top to bottom (image from fig. 11)): Red, Green, and Blue channels. b)Zooming in on left side of distributions in fig. 12 (top to bottom): Red and Green channels.

Table 5: Variance of individual color channels (RGB color space) over 10 blood smear images with different noise characteristics.

Color Channel	**Image Characteristics**	**Variance**
Red	Normal images	$1.2395 * 10^{08}$
Green	Normal images	$1.4088 * 10^{08}$
Blue	Normal images	$0.94807 * 10^{08}$
Red	Additive medium noisy images	$2.19 * 10^{08}$
Green	Additive medium noisy images	$2.99 * 10^{08}$
Blue	Additive medium noisy images	$1.75 * 10^{08}$
Red	Additive high noisy images	$1.14 * 10^{09}$
Green	Additive high noisy images	$1.41 * 10^{09}$
Blue	Additive high noisy images	$0.82 * 10^{09}$

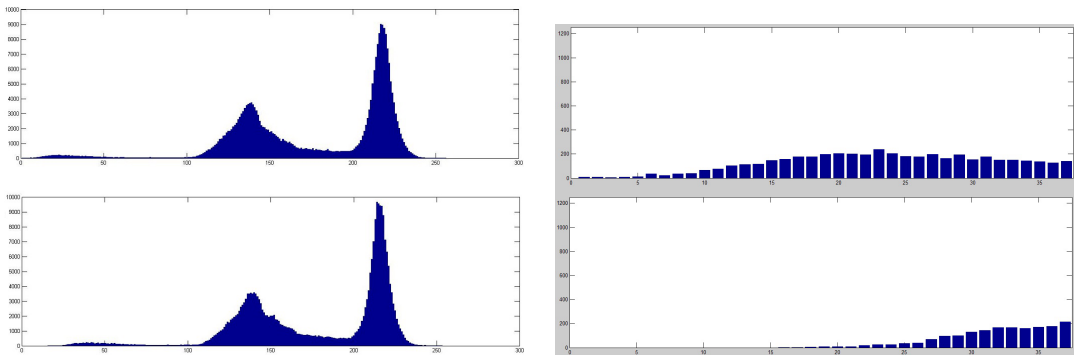

a b

Figure 14: a) Gray scale distribution (top to bottom (image from fig. 11)): a) Green (RGB) and Y (YIQ) channels. b) Zooming in distribution (top to bottom): G (RGB), Y (YIQ).

Table 6: Variance of G (RGB color space) and Y (YIQ color space) over 10 blood smear images with different noise characteristics.

Color Channel	**Image Characteristics**	**Variance**
G	normal images	$1.4088 * 10^{08}$
Y	normal images	$1.2707 * 10^{08}$
G	additive medium noisy images	$2.99 * 10^{08}$
Y	additive medium noisy images	$1.47 * 10^{08}$
G	additive high noisy images	$1.41 * 10^{09}$
Y	additive high noisy images	$0.98 * 10^{09}$

3.2.2 Image De-Noising

This section briefly compares some work that are non-linear thresholds in image de-noising. In particular, we implement twelve leading de-noising algorithms in terms of blood smear de-noising. Two types of multiplicative noise are often found in microscopic imaging: thermal and shot noise. Random fluctuations of amplified electrons from a photo-sensor cause thermal noise. Thermal noise becomes more highlighted especially in low-light situations with more required amplification. Thermal noise is interpreted as a Gaussian random value where it has mean zero and non-zero variance. The noise level (Gaussian) is equal at all pixels. Also, photons hitting the sensor is a random process that causes shot noise. Shot noise is modelled as a Poisson distribution. In general, a Gaussian, or normal distribution with mean and variance is the most possible important distribution in these microscopic imaging. Following that, to do a comprehensive comparative study, the original images have been corrupted synthetically by additive Gaussian noise of zero mean and an arbitrary variance to stimulate the poor scenarios.

The non-linear threshold methods (for more details see Section 3.1.2) such as phase preserving de-noising [109], wavelet neighboring sub-band SURE shrinkage [42], Gabor wavelets [57], Bayesian non-local means filter [36], local PCA decomposition [136], hierarchical PCA and global PCA [27], Wavelet SURE shrink [50], wavelet Bayes shrink [30], wavelet Visu (soft and Hard) shrink [49] and also Bivariate wavelet shrinkage functions [205] are investigated in this framework.

Thereby, to compare performance peak signal-to-noise ratio (PSNR) measure is

applied. $PSNR(dB) = -10 \times \log_{10} \frac{\sum_{ij=0}^{n} |(B_{ij} - A_{ij})|}{n^2 \times Max_{A_{ij}}}$ computes the peak signal-to-noise ratio, between two original and additive noisy blood smear images where B_{ij} and A_{ij} are noisy and original intensity value in gray-scale imaging with $Max_{A_{ij}} = 255$.

Table 7 presents $PSNR$ results for both moderate and high additive Gaussian noise with standard deviation 30 (medium level) and 100 (high noisy level), respectively. In fig. 15 visual appearance of using different de-noising techniques are shown. This experiment compares the performance of the Bayesian non-local means algorithm and the other de-noising techniques under different initializations: original or degraded (additive noise) blood smear image. Bayesian non-local means filter yields better performance than the other image de-noising techniques (see Table. 7). From the experimental results it can be concluded that for moderate noise the Bayesian non-local means filter produces the best results. It produces the maximum PSNR for the output image compared to the other filters. However, other algorithms namely, wavelet neighbouring sub-band SURE shrinkage that uses dual-tree complex wavelet transform to lessen redundancy problem, self-invertible Gabor wavelets that maintains poor orientation resolution details and also Bivariate that preserves dependency between pixels in different scales are also appropriate alternatives to be considered. The neighbouring wavelet shrinkage output is somehow blurred and post-processing steps involving de-blurring and edge preserving may be needed.

It can also be observed that for Gaussian noise these named methods produces better results than the classical median filter may cited in previous blood smear detection work [44]. The median filter output is very blurred in presence of Poisson and Gaussian noise that may lose main details in a given blood image (see Fig. 15). It can also be observed that SURE shrink cited in blood smear detection work [135] has PSNR = 11.62 where other techniques such as Bayesian non-local means filter, self-invertible Gabor wavelets, Wavelet neighbouring sub-band SURE shrinkage and Bivariate have higher PSNR (see Table. 7).

Further, in presence of high noise level, wavelet neighbouring sub-band SURE shrinkage produces better results than the other. Also it should be noted that presence of such as this high Gaussian noise ($N(\mu = 0, \sigma^2 = 100)$) is almost impossible in practice.

To sum up, experimental results with average noise level and the quantitative PSNR measure in a comparative study indicate that Bayesian Non-local means, self

invertible Gabor wavelets, neighbouring sub-band SURE shrinkage function, and bivariate are as efficient methods to de noise digital images in presence of additive Gaussian noise in microscopic imaging.

Table 7: Non-linear de-noising techniques for blood smear samples using PSNR levels with moderate and high Gaussian noise ($N(\mu = 0, \sigma^2 = 30, 100)$).

		Additive Noise Deviation	
		PSNR($\sigma^2 = 30$)	PSNR($\sigma^2 = 100$)
Methods	Bayes Shrink	11.0760	10.0183
	Bayesian Non-local means	***19.9736***	11.2937
	Bivariate	14.5495	11.3376
	Log Gabor wavelet	15.5730	13.1074
	Neigh SURE shrink	15.2426	***15.4017***
	Patch based Local PCA	13.2424	10.8443
	Patch based Global PCA	13.1923	10.8587
	Patch based Hierarchical PCA	13.0809	10.8745
	Phase Preserving	14.2682	10.5320
	SURE shrink	11.6209	11.4432
	VisuShrink(Hard)	12.2455	14.7936
	VisuShrink(Soft)	14.3215	14.5921

3.2.3 Image Edge Preserving

An appropriate filter to removes details in a high contrast region, and preserves boundaries even in low-contrast areas is Kuwahara filter. As a result, to recover degraded and blurred boundaries in white blood cell while reducing the negative effect of noise in images, edge preservation, Kuwahara as a non-linear smoothing filter is applied. This filter takes a square window ($size_{length} = 2 \times l$) around a pixel $I(x, y)$ in the blood image. This square is divided into four smaller square regions $Q_{i=1\cdots4}$ for a given point. It computes the mean (μ) and variance (σ) for four sub-quadrants, and then it assigns the mean of the pixels with lowest variance to other sub-quadrants regions [115, 167]. Thereby, Kuwahara as a noise-reduction filter that preserves whitr blood edges is performed to compensate for blurring side-effect and also a painterly look is achieved by preserving and enhancing directional image features.

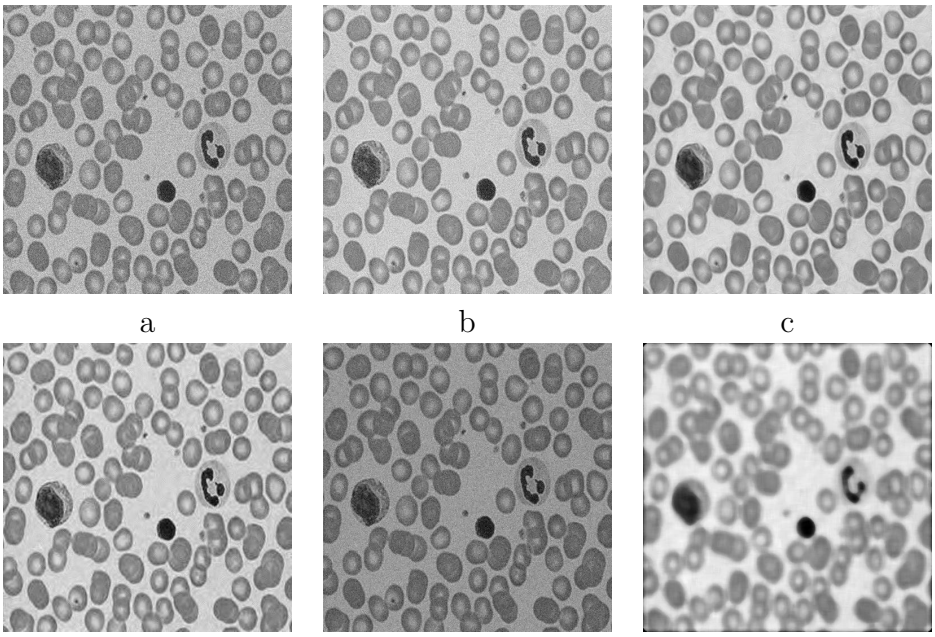

Figure 15: De-noising by different methods for blood smear images corrupted by Gaussian noise ($N(\mu = 0, \sigma^2 = 30)$) : a) Noisy Image, b) Bayesian Non-local means, c) Gabor Wavelet, d) Neigh SURE Shrink, e) Bivariate and f) Median filter.

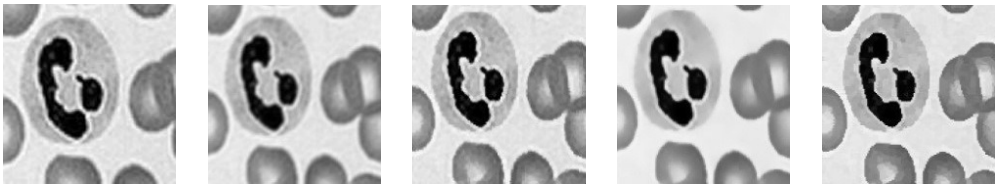

Figure 16: Edge-preserving for a given white blood cell image: a) Original b) Convolution kernel, c) Symmetrical Nearest Neighbour filter, d) Bilateral filter and e) Kuwahara filter.

3.2.4 Pre-Processing Settings

This section gives a brief overview of initial settings with regard to image enhancement and pre processing steps (see Figs. 5,6). This section briefly explains how each parameter is set. There are many challenging problems in setting these parameters in an ideal efficient way and some changes are inevitable to apply for different dataset. However, the most parameters could be kept unchangeable.

Colormap Selection

This study uses JPEG format (see Section 3.1). Following that, to choose a proper gray scale channel statistical approaches such as variance and semi interquartile are addressed. These two measures determine whether local details are enough kept (see Tables 4, 5). There is no parameter that should be set manually.

Denoising Selection

This framework uses Bayesian non-local mean [36], Gabor wavelet [57], Bivariate [205] and neighbouring SURE shrink function [42] (see Table 7). These candidates require initialization and setting before going further to use them. These settings are in table 8.

Image Abstraction

As for white blood cell detection, edge preserving and image abstraction is addressed using Kuwahara filter (see Fig. 16). Kuwahara filter is by a sliding windows with where its parameters namely, mean and standard deviation are automatically calculated in four sub-regions in a defined sliding windows. This size should be enough small to cover all details. To sum up, only windows size is manually set (15×15). Of course, it is obvious smaller windows just only increase running time and there is no more burden than increasing computational time.

Table 8: De-noising: Settings and Parametrization

	Bayesian Non-local Mean	
Parameter	**Value**	**Comment**
M	7	Search area size $(2 \times M + 1)$ That is a window with 15×15 pixels.
α	3	Patch size $(2 \times \alpha + 1)$.
h	0.1	To control how to maintain local structures as well as noise removal.

	Self Invertible Gabor wavelets	
Parameter	**Value**	**Comment**
Nf	5	Number of scales of log-Gabor transform.
No	8	Number of orientations of log-Gabor transform.
Dec	1	Gabor domain will be decimated (dec=1) or non-decimated (dec=0)
$Type$	$Soft$	Denoising thresholding function (Hard Vs Soft).
f	1	Parameter that tunes the denoising strength (> 0).

	Neighbouring SURE Shrink	
Parameter	**Value**	**Comment**
Wavelet Function	DT_CWT	DT_CWT (section 5.3.3)reduces uncertainty, minimizes redundancy in the output.
Ł	3	The number of wavelet decomposition level.

	Bivariate Denoising	
Parameter	**Value**	**Comment**
Wavelet Function	Daubechies	More coefficients both in low pass and high pass.
L	3	The number of wavelet decomposition level.

3.3 Comparison of the Proposed Approach to the State-of-the-Art

This section concerns color channel selection, de-noising and edge preserving that presents a comparison of the proposed approach to state-of-the-art pre-processing techniques for analyzing blood smear images .

3.3.1 Colormap Selection

Authors in other works [18, 44, 46] proposed different channels due to the nature of their data. However, the experimental data are rather controversial, and there is no general agreement about color space selection. This thesis examines mono-chromic channel in different color spaces (see Section. 3.2.1). The green channel selection is supported by the calculation results in normal blood smear slides (see Table 3).

The green channel is better at maintaining high frequency feature information and contrasts in gray scale intensity that are more easily distinguished in the G channel. The high frequency information is essential to preserve white blood cells structure in particular (see Fig. 11). However, combination of different channels with weighting of individual channels to achieve a desired appearance is not addressed in this thesis and will be in the future.

3.3.2 Denoising Selection

As for blood cell detection, there is a considerable volume of published studies describing the role of median filter in blood samples de-noising. In work [18, 44, 46] and also in malaria research [224, 225, 226] median filter is used to de-noise blood microscopic images.

Median filter is an appropriate technique to remove salt-and-pepper noise where pixel looks much different from its neighbours. Median filtering often fails to provide agreeable smoothing of non-impulsive noise where the underlying object has edges [25,152] and its result could be unpredictable for different dataset. Perhaps the most serious disadvantage of this median method is that there is no way to address correlation and dependency between pixels and then it adversely reduces the visibility of certain features within the image. Moreover, the median filtering approach is not efficient for the images with large amounts of Gaussian noise or speckle noise [152]. Median filter depends on sliding windows size and once intensity values are nearly small compared to the size of the pre-determined neighbourhood, it will adversely change the median value and then eventually the median filter cannot sort out image detail from undesirable noise. As a result, median filter is not an appropriate candidate for blood smear images with these nature of noise that may address in blood smear imaging (see Section. 3.2.2).

Other work in 2011 [135] explored wavelet de-noising by inter-scale orthogonal wavelet which is based on stains unbiased risk estimator (SURE) approach. In this method, as it can be seen from literature review, it is assumed that the wavelet coefficients are independent and there is no connection in different wavelet scales. However, independence assumption may not be satisfied for natural images and blood smear samples.

In conclusion, as it can be seen from results, Bayesian non local mean, optimal

threshold using SURE shrinkage function with dual tree complex wavelet and neighbouring window, self-invertible 2D Log-Gabor wavelets and Bivariate filter bring benefit in blood smear de-noising (see Table 7) in presence of different Gaussian noise level.

3.3.3 Image Abstraction

Previous studies of white blood cell segmentation have not dealt with this possible adverse condition in blood smear slides where boundaries are messy, granular and in low faded conditions. Experimental results show that Kuwahara and Bilateral filters are proper candidates to build better outcome close to the expected boundaries. In general, Kuwahara is superior to Bilateral in this application (see Fig. 16). Kuwahara filter brings two benefits together. It expands homogeneous region in cytoplasm to its heterogeneous neighbours using a sliding windows. This approach thus removes unwanted color details in cytoplasm that they are not needed in this low resolution images. Secondly, as mentioned before white blood cells do not have determined edges. This filter makes a sharp pixels next to non-obvious edges. As a result, existing sharp pixels close to possible edge and also removing unnecessary details bring benefits for next steps in white blood cell segmentation (see Section. 4.4.2) and also in feature extraction (see Section. 5.5).

3.4 Pre-Processing Findings and Contributions

One of the contributions is the pre-processing, for enhancing the appearance of the shape. It includes color channel selection, de-noising and edge preserving that are explained in details as follow. Colour space selection would be automated using distribution behaviour calculations to keep local and global details. This De-noising algorithm is a significant development as the most commonly used approaches, i.e. Median filter, can not be used when the nature of noise is either Gaussian or unknown. And also the results of the edge preserving are found to be promising when the white blood cells having degraded internal structure and almost invisible boundaries.

3.4.1 Colormap Selection

This work proposed a statistical calculation for analyzing the color map selection in presence of different possible color spaces (see Section. 3.1.1). The method is based on a variance and semi interquartile that enables us to test how low and high frequency information can be accumulated. These details are very critical in presenting white blood cells where boundaries and their internal structure are very fragile and of course inappropriate selection leads inevitable problems in next framework step. For example, blue channel in current dataset is unable to maintain intensity details separately (see Fig. 11). Authors in other works proposed different channels due to the nature of their data. Comparative study and discussion is addressed in section 3.4.1. However, combination of different channels with weighting of individual channels to achieve desired appearance is left for future study.

3.4.2 Denoising

This work has empirically tested different de-noising mechanisms for a given intensity blood image. As for blood cell detection, there is a considerable volume of published studies describing the role of median filter in blood samples de-noising. In addition, few work used SURE wavelet shrinkage as well. Discussion will be found in section 3.3.2. In conclusion, as it can be seen from presented results that Bayesian non local mean, optimal threshold using SURE shrinkage function with dual tree complex wavelet and neighboring window, self-invertible 2D Log-Gabor wavelets and Bivariate filter bring benefit in blood smear de-noising (see Table 7) in presence of different Gaussian noise level produce the best results.

3.4.3 Image Abstraction

Third, in terms of blood cell detection, white blood cell is with low contrast boundaries and weak edges. The Kuwahara edge preserving is highly suited to enhance poor visibility conditions (see Fig. 32). Experimental results and discussion is found in section 3.3.3 and figure 16. As a result, existing sharp pixels close to possible edge and also removing unnecessary details bring benefits for next steps in white blood cell segmentation (see Section 4.4.2) and also in feature extraction (see Section 5.5).

Chapter 4

Blood Binarization & Cell Separation

After de-noising and artistic edge enhancement, binarization is the third step which allows to extract some features, having sub images and get ready to apply techniques for different purpose over the images. This work proposes a modified binarization method that reduces limitations and drawbacks of each local and global thresholding.

Binarization and some post-processing to enhance the quality of binary image is followed by cell size estimation which helps to differentiate various types of particles in the blood smear image. The size estimation approach is chosen in this step because it identifies several advantages of the case study. Normal red blood cells in particular are found with an average size distribution in healthy people. Moreover, cell separation into two sub-groups including white blood cells and red blood cells is followed also on using size parameter.

Further, a key step in many experimental blood smear analysis involves counting of red blood cells and white blood cell differential (see Section 1.2.1). A simple counting of cells brings different benefits for health system and provides a great help in detecting problems at early stages.

4.1 Problem Statement

After pre-processing (denoising and edge enhancement), binarization is the third step which allows to extract WBCs and RBCs sub-images, compute the RBCs size and

count them. The aim of this section is to determine which algorithm is the most reliable and robust for binarization of medical images, specifically used in blood cells.

Generally, binarization can be applied with either global or local thresholding where both have intrinsic problems. For the global approach, a constant intensity threshold value T (between 0 and 255) is chosen. If the intensity value of any pixel (in the grey scale) of an input image is greater than T, then pixel is set to white otherwise it is set to black. A global threshold (T) which maximizes the variance between the means of the histogram classes on each side of the threshold is selected. On the other side, a local thresholding technique depends on the window size moving over the image that it separates background with local statistics measures.

Global binarization argument relies heavily on quantitative analysis of one unique threshold value in which most local approaches use adaptive local values. Uniform contrast distribution in most cases leads to global thresholding unlike in presence of degraded images, complex scene images, variation in contrast and illumination. In these aforementioned conditions, global thresholding may fail to resolve the contradiction between background and foreground.

Different algorithms have already introduced to improve both local and global thresholding of digital images. In general, no identical binarization algorithm is superior to others. However, some methods are better than others for specific applications. The goal in this study is to obtain a robust binarization method to allow for further blood image content clarification. Binarization is the last step before computing cell sizes and their enumeration.

Further, a normal blood cell is one of two major particles: a RBC with a normal probability distribution function (PDF) with average size around 6.0-8.5 μm or a WBC with average size around 7-18 μm which includes a nucleus and cytoplasm. Mature WBC is about equal normal RBC size (i.e, Basophil) up to 3 times bigger than normal and mature RBCs (see Section. 1.2).

As mentioned in medical background (see Section 1.2.1), size is a key parameter to identify the blood sample health. Also, as mentioned earlier (see Section 1.2.1), the red cell distribution width (RDW) is an expression of the red blood cell (RBC) size distribution in complete blood count (CBC) report.

We use *size characteristics* as an effective factor to distinguish between the two main types of cells that are RBCs and WBCs. Red blood cells size estimation is

an essential task at various stages of blood slide processing to go further in cell segmentation. We aim to have two sub-images containing individual white blood cells and red blood cells are separated in order to count cells in CBC medical test. The aim of segmentation is to isolate each individual blood cells, especially when they are close and overlapping in the viewing of the microscope.

It locates and recognizes the cell contours to distinguish amongst them. An inaccurate segmentation leads to ulterior quantification and parameter measurement. The goal of our CBC segmentation and counting research is to find methods partitioning the digital blood smear image into non-intersecting regions; RBCs and WBCs.

Finally, thus far, after cell separation we have two individual sub-images for RBCs and WBCs and have localized the WBCs. A complete medical CBC reports number of cells to properly understand a patients health. In particular, the distribution of the different subtypes and proportional rate in a blood sample is CBC interest.

4.2 Literature Review

To the author's best knowledge, there are no comparative evaluations of the efficiency of binarization algorithms at binarizing medical blood smear images.

4.2.1 Global Thresholding

A considerable amount of literature has been published on global binarization. Ridler and Calvard (1978) [190] developed a binarization algorithm while retaining the appropriate possible illumination of the image. In 1979 Otsu [164] classified foreground and background with a global threshold. The optimum threshold in Otsu method is selected automatically by using the probability terms whereas it maximizes variance between-class and minimizes variance within-class. Other than Otsu algorithm, there is a large and growing body of global thresholding schemes have been proposed such as algorithm of Kapur *et al.* [97]; Fan *et al.* [55]; Portes de Albuquerque *et al.* [40]; and also Xiao *et al.* [251]. It should be noted that among all these global binarization studies, Otsu [164] is frequently cited.

4.2.2 Local Thresholding

Locally adaptive binarization methods compute a threshold for each pixel in the image on the basis of information appeared in a neighbourhood of a given pixel. During the two last decades, a lot of information has become available on local thresholding. The first discussion and analyse of local thresholding backs to 1972 with Chow and Kaneko algorithm [32]. In that method, original image is divided into a set of regions. Intensity histograms are computed for all sub-divided sections and then thresholding value will be selected for these histograms. All predefined local thresholding values are interpolated twice times first region-wise and then point-wise to obtain a threshold for the original image. Numerous studies have been attempted to reach better performance in different applications. They are more promising locally adaptive binarization methods that we could mention in the literature.

Bernsen [16] in 1986, introduced a method which is based on a given contrast threshold in a sliding window. The pixel is set at the mean of the minimum and maximum grey values in the sliding window if local contrast is above the predefined contrast. Otherwise, it is set to background. The contrast value is arbitrary where default value is recommended to be set at 15.

Niblack [155] in 1990, introduced a binarization algorithm using two values that are mean and standard variation in a sliding window. The size of the window must be large enough to suppress the noise amount in the image as well as be also small enough to maintain local details. In practice, a window size of 15-by-15 could be an appropriate selection. This method can work roughly without user intervention as it requires only a coefficient value that helps to separate and adjust the percentage of pixels that belong to foreground (especially in the boundaries). The default value is 0.2 for bright objects and -0.2 for dark objects. In Current application as cells (see Fig. 10) are almost darker than background we could use $k = -0.2$.

Sauvola [201] in 2000, also introduced a local thresholding method using means and standard variation in a sliding window. Sauvola is almost considered as a variation of Niblack's method. However, the formulation has a little difference and it has two parameters to be adjusted. Parameter (k) that default value is 0.5 and (r) that usually is 128. These two value are very questionable and the existing default fail to resolve the contradiction between foreground and background with different conditions. Overall, these setting are almost arbitrary and could be changed with

different dataset and user interference is addressed to some extent.

Feng *et al.* in 2004, introduced a local thresholding method [56] with using many parameter settings. Feng method is an appropriate candidate to maintain information from a given image, especially for poor quality, non-uniform illumination, low contrast samples. This method can qualitatively outperform the other thresholding methods. However, the Feng method contains many parameters. This method used two sliding windows with different size to preserve the details. The threshold value is calculated where α, γ, K_1 and K_2 are positive constants that they rely on the nature of dataset. Padding parameter should be also set which are circular, replicate and symmetric. Feng argument relies heavily on quantitative analysis of image parametrization. This method requires calibration through different iterations of testing and retuning. One of the limitations with this explanation is that it does not explain how parameters could be set automatically to some extent. The optimum window size and other parameters can be adjusted using different experimental results and this system requires user surveillance. Hence, this method is not recommended widely for an semi-automated system without user intervention.

Gatos *et al.* in 2006, [65] introduced a two-step approach to build a local thresholding method. First Sauvola's method is applied and then local threshold values based on the estimated background are computed. This method could be an appropriate option in presence of degraded and complex background. However, background estimation can be addressed in different ways [64, 142] and there is no superior identical method that can be used for different backgrounds with varying conditions.

Bradley *et al.* in 2007, [22] introduced a local thresholding method that a given pixel is considered as a foreground if its brightness value is lower than the average brightness of the surrounding pixels in a given sliding window. The amount of difference is calibrated using a percentage value (T) and should be adjusted empirically. This manual settings can be changed for different circumstance and dataset. However, the advantage of this method is its low computational time and only on T parameter adjustment. Bradley method is two times faster than Sauvola's method [201]. Local mean and variance are computed in Sauvolas method, while Bradleys method calculates just local mean and variance can be calculated using expected value.

Su *et al.* [219] in 2010 proposed an edge-based local threshold method that it computes image contrast. Their approach profits combination of canny as an edge

detector and Otsu to Binarize images. This method is good at removing heterogeneous background noise but it may fails to detect the degraded, low resolution and close-by objects.

Hedjam *et al.* [86] in 2011 used a prior information and the spatial relationship on the image. This method used Gaussian distribution to model foreground and background where as the first step, Sauvolas method is used to Binarize original image. This method is based on known local prior information of the background and foreground. However, there is an inconsistency with this argument.

Ntirogiannis *et al.* in 2014 proposed [157] proposed a combination of a global and a local thresholding binarization method at connected component level to reach better performance in presence of variety of degraded handwritten document images. The method profits combination of Niblack and Otsu algorithm on normalized images. This combination and discussion is very close to already our published paper in 2011 and 2012 [72, 78].

4.2.3 Blood Smear Binarization

To date, the blood smear researches are more about on global thresholding methods rather than local thresholding methods. Some papers on blood segmentation such as [15], [242] and also one of frequently cited work [46] all tried global thresholding method using the well known Otsu method. The existing global Otsu thresholding value fails to resolve different conditions that exist in blood slide images. A serious weakness with this argument, however, is that known but also it does not manage binarization with nearby background and foreground intensity values range [78].

No research has been found concerning combination of global and local thresholding in microscopic imagery systems. This research discusses the challenges and strategies to manage binarization in presence of different unfavourable conditions in a typical blood smear image.

4.2.4 RBC Size Estimation

There is a considerable volume of published studies describing the role of Granulometry for size estimation in mathematical imaging and vision. Granulometry is a known method to extract blood smear size characteristics. Automatic thresholding

using Granulometry and regional maxima in image pattern spectrum are addressed in some blood studies such as [14, 41, 46, 194, 226]. Granulometry and its applications will be explained in the section. 4.3.2.

4.2.5 RBCs & WBCs separation

A serious attempt to segment in order to count backs to Vincent *et al.* work with morphological filter to reconstruct segmentation in image analysis in 1993 [239]. Svensson *et al.* described a decomposition scheme by a fuzzy distance transform to separate objects into sub-parts [221]. Li *et al.* [125] introduced a framework to segment nuclei in images where their framework is based on three steps including a gradient approach, flow tracking and grouping, and finally local adaptive thresholding.

Hoover *et al.* [88] described an automated framework to locate blood vessels using match filter and thresholding algorithms. Jelen *et al.* [94] addressed nuclei segmentation on breast cancer malignancy classification with level set, fuzzy cmeans segmentation. Quelhas *et al.* [176] introduced sliding band filter to locate cell nuclei and cytoplasm with evaluation for two datasets of cell culture images. Sadeghian *et al.* [198] introduced a frame work to segment white blood cells using image gradients, edge detection algorithms. Dorini *et al.* [51] introduced nucleus and the cytoplasm segmentation with self-dual multi-scale morphological toggle (SMMT) filter along with scaled erosion and dilation morphological operations to improve the correctness and performance of two known watershed transformation and level sets segmentation approaches. In an important work Di Ruberto *et al.* [46] used classical area opening (see Fig. 26) morphology technique to separate between WBCs and RBCs. Authors claimed to isolate the white cells by a morphological erosion with a disk-shaped structuring element whose size is achieved by the granulometric analysis (RBC size). This approach has some drawbacks. It just neglected overlapping phenomena among cells. It is not also efficient for all possible five WBCs types where Basophil (fig. 1) can be possible found the RBC size. Some previous studies have focused on the implementation of active contours to extract blood cell boundaries in white blood cell study [80]. Blood vessel segmentation using active contours is also addressed in [43]. Active contours [191] require initialization and additional regularizers and therefore, the active contour using a level set adjustment in some cases is costly and also makes unwanted extra spurious regions as fake boundaries.

4.2.6 RBC Counting

Watershed is frequently used for an automatic contour detection and cell segmentation [131, 240]. First idea of watershed comes from geography topographic concepts where water divides lines of the domains of attraction of rain falling over the region (Tobbogan method). An alternative approach is where landscape being immersed in a water, with holes pierced in local minima that are called Basins. These two approaches [131] are interpreted as follow. Immersion starts from low altitude to high altitude while Toboggan approach starts from high altitude to low altitude. Watershed in image processing isolates objects from the background into disjoint regions (see Fig. 28).

4.3 Research & Experimental Results

4.3.1 Blood Binarization

To separate blood particles (foreground) from background the binarization step is applied. In this study , the foreground objects are RBCs and WBCs while the remaining objects such as platelets, artefacts in peripheral blood smear and stained plasma are declared as background.

In the blood smear images slides, because of different kinds of image acquisition, illumination, staining and when the intensity variations between the cells and stained plasma are low, and since there are frequently overlapping and very closely positioned particles, finding a global value T (Thresholding) to separate the image into two ideal regions of blood particles and background is not always simple and perhaps not even possible (closely positioned pairs of particles will be merged into single particles, regardless of any fine tuning of the value of T). After pre-processing which are denoising and edge enhancement; several binarization algorithms including Niblack [102], Bernsen [16], Sauvola [201], Feng algorithm [56], Wolf & Jolion [247], Bradley [22] and Otsu [164] to enable foreground background separation improvement of blood smear microscopic images (see Fig. 17) can be candidates where in practice we have a variety of intensities of grey in the blood smear images. This contribution is directed toward a robust binarization method in blood smear digital diagnosis. In Niblack [102], the local thresholding is based on $T(x, y) = m(x, y) + k * s(x, y)$, where $m(x, y)$

and $s(x, y)$ are the average and the standard deviation of a local area for which the size of the window must be large enough to suppress noise in the image while at the same time it has to be small enough to maintain local details. The value of k decides how much of the total print object boundary is taken as a part of the given object. Coefficient k helps to separate and adjust the percentage of pixels that belong to foreground (especially in the boundaries).

In experiments over different samples with different initial conditions (see an example in fig. 17) showed that Niblack is the most reliable method to maintain disjoint components which is crucial in avoiding over or under segmentation. However, This local binarization tends to produces a considerable amount of spurious foreground regions in non-cell particle regions.

After comparison study between the various algorithms for pixel segmentation a merged binarization algorithm on blood smear images with different characteristics and staining conditions is proposed. To overcome the problem of unwanted made foreground spots, this work takes advantage of merging Niblack local thresholding with Otsu global algorithm. Otsu global thresholding is not an appropriate binarization individually where this method tends to result in overlapping objects that are too close to one another which in turn leads to false results after segmentation.

In particular, we aim at more accuracy in terms of minimizing the number of close pairs of particles that are merged into single particles during binarization process. In the modified version, pixels are labelled as backgrounds pixels if they are labelled as either background pixel in Niblack or in Otsu and the remaining points are kept as foreground (objects). Using this merging process, we mitigate the problem of extra small spurious regions produced by the Niblack algorithm. In the experiment involving Niblack algorithm 15×15 neighbourhood and $k = -0.2$ regarding to this image size and cell magnification are selected.

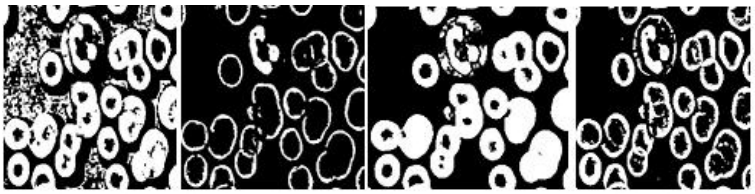

Figure 17: Binarization methods: a) Bernsen; b) Sauvola; c) Otsu; and d) Niblack

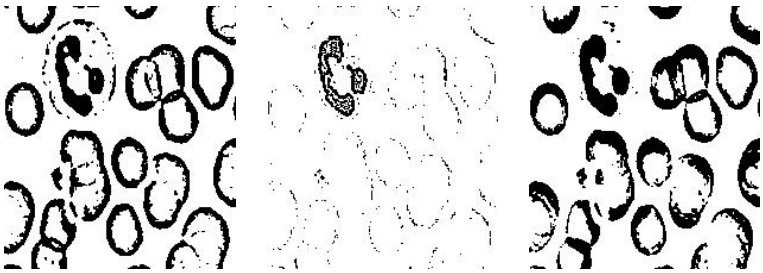

a b c

Figure 18: Local Binarization Methods: a)Bradley b)Feng and c)Wolf

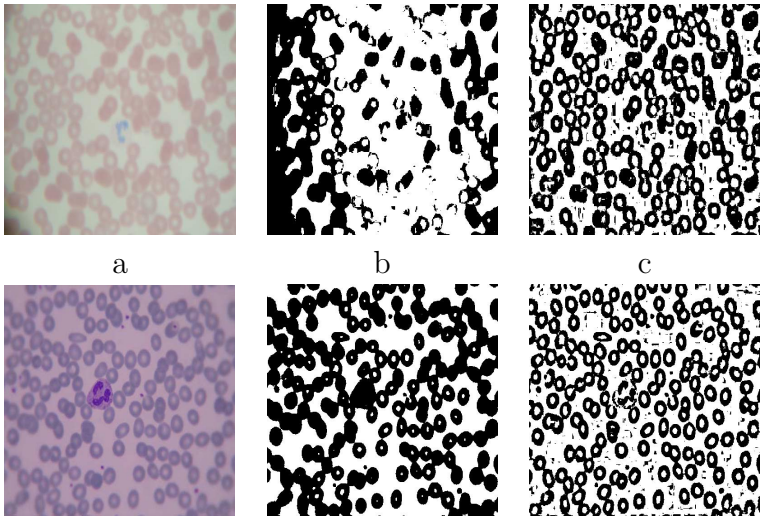

a b c

d e f

Figure 19: Binarization for low quality image: a, d) Original images b, e) Otsu, c, f) Niblack

Statistical Measures & Experimental Results

To determine the best binarization algorithm, we determine the statistical significance between the algorithms by using the normalized cross-correlation (NCC) approach $\Upsilon(u, v)$ (see Eq. 1) which is often used in template matching and pattern recognition problems for determining the degree of similarly between two images A and B (as a template matching using green channel output of each image) [20]. If A exactly matches B then γ (the array of correlation coefficients) is equal to 1 while in cases of exact dissimilarity result in $\gamma = 0$. In general, the coefficients in γ typically vary between (-1) and $(+1)$ [72].

This comparison with normalized cross-correlation (NCC) approach is limited to

only four appropriate candidates (see Fig. 17) in this experiment. The experimental data in other cases are rather controversial, and there is no general agreement about their usefulness (see discussion in section. 4.2.2). In some cases, like Feng algorithm [56], many parameters adjustments are necessary, which, in turn, requires user intervention for different conditions due to overload.

$$\gamma(\upsilon,\nu) = \frac{\sum_{x,y}[A(x,y) - \bar{A}_{\upsilon,\nu}][B(x-\upsilon,y-\nu) - \bar{B}]}{\left\{\sum_{x,y}[A(x,y) - \bar{A}_{\upsilon,\nu}]^2 \sum_{x,y}[B(x-\upsilon,y-\nu) - \bar{B}]^2\right\}^{1/2}} \tag{1}$$

The resulting coefficients in the matrix of normalized cross-correlation (NCC) cannot all be needed and then the measurement of performance and efficiency are subjected to a comparison using the average (expressed as the mean, median, and mode), standard deviation and range to show how much variation or dispersion there is between existing values.

In our experimentation to study the effect of noise on binarization results, we degrade the objects (foreground) in samples by adding noise including Gaussian and speckle noise to simulate worst cases that may appear in image capturing. Also to simulate dirty slides or camera lens a 2, 3 pixel Gaussian blur to the samples is applied.

The following tables present the results obtained from the preliminary analysis of normalized cross-correlation (NCC). The result has been divided into three parts. The first part (see Table 9) deals with all 10 sample blood images (see Fig. 10). Then it goes for for separated white blood cell images (table 10). Finally, the last table investigated the impact of binarization on red blood cells (table 11). In terms of NCC value the largest means are generated by Otsu as a global thresholding and the dispersion and variation is low which prove the acceptable degree of similarity between image and its template. However, in WBC segmentation and discrimination between WBCs and RBCs this approach may fail and also this algorithm merges disjoint close by objects as it uses global thresholding over all slides and then local details are not kept. WBCs nucleus and cytoplasm intensity vary from the intensity of dominant of RBCs and as the number of RBCs is about 100 times more than WBCs then global thresholding is influenced by RBCs rather than WBCs. Therefore, WBC boundary and its components are degraded and damaged based on Otsu global thresholding in

spite of having higher template matching.

Next, this calculation has also been applied to separated regions composing of a single WBC and few RBCs, with small gaps between these objects (see Fig. 17). The NCC shows Niblack algorithm brings higher NCC performance. However, in Niblack, because of using local thresholding, a minor background difference in intensity value, makes spurious objects may results such as unwanted fake foreground spots. As a result, after enough investigation the desired result is achieved with higher NCC in a small windows (Niblack) including WBCs and few close by RBCs (better segmentation in foreground) with along higher NCC value in global thresholding by Otsu to avoid having spurious spots in background. Admittedly, merged these two Niblack and Otsu develops a methodology for the selective binarization. The results obtained from the preliminary analysis of NCC are shown in following tables (see Tables. 9,10,11). In the experiment involving Niblack algorithm 15×15 neighbourhood and $k = 0.1$ regarding to this image size and cell magnification are selected. The experimental results indicate that merged Niblack and Otsu is enough sufficient to obtain foreground and background separation.

4.3.2 RBC Size Estimation

Granulometry [206] results size distribution in pattern spectrum diagram (output). Granulometry algorithms involve sequences of openings ($I \circ SE = (I \ominus SE) \oplus SE$) or closings ($(I \oplus -SE) \ominus (-SE)$) derived from the erosion and dilation of increasing size, where I and SE are image and structure element. $\ominus$ and $\oplus$ also denote the erosion and dilation, respectively. Granulometry is determined with $\forall x \in I; \;\; x \mapsto s + \lambda s \times x$ where S is a homothetic center and λ is an expanding non - zero ratio. Granulometry is commonly interpreted to a maximum of morphological opening morphological operation (or closings) with the homothetic transformation which is an increasing affine transformation space of a simple convex structuring element (SE). Typically, structuring element (SE) is a line segment, a circle, a square, or a hexagon.

Edge Fracture in Granulometry

In broadly speaking, Granulometry uses a series of morphological opening operations to estimate a size distribution of particles in digital images. As a expected result, in an ideal output, we should have only one peak for a single complete circle, but

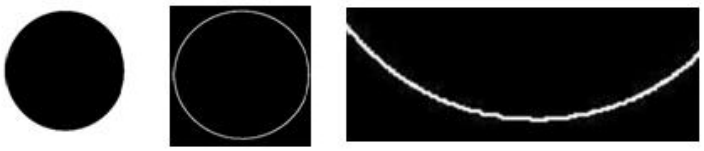

Figure 20: Granulometry over simple circle

an incomplete circular object shown in fig. 20 produces local maxima. We call this undesirable effect an *edge fracture* [113]. We just observe that after applying the edge detection and skeleton algorithms to real cell images which are typically not complete curves the observed circular pieces are regarded as a new objects surrounded between two ideal complete circles. Consequently we can expect in granulometric output at least two local regional peaks. By this simple work, we find that blood smear particles are not complete circular object and there are always discrete components on curve tracer, which is another reason for undesirable local maxima.

Area-Granulometry

In literature review, Granulometry as a volume and mass distribution is found with two variations (Granulometry vs Area-Granulometry). Area - Granulometry [140,143] brings two benefits to size estimation in blood smear sample. Any patch and hole inside the blood image objects (such as seen in fig. 21) leads to errors in pattern spectrum computation with spurious regional maximum that are more in typical method. Furthermore, area method introduces fast algorithm to be applied [140]. Finally, Area-Granulometry gives better performance than Granulometry with an improved estimator of size distribution of image and it is an appropriate tool for size distribution in presence of blood smear slides with different resolution.

According to normal blood probability density function (PDF) and since white blood cells are very fewer in number than red blood cells, with a ratio of about 1 white blood cell to every 100 to 200 red blood cells. The maximum regional peak in pattern spectrum diagram (Area - Granulometry output; see Fig. 23) refers to the number of RBCs with an acceptable RBC radius size (in this sample is 10px). It is not possible, though, to estimate the size of WBCs based on Granulometry because of their intrinsic characteristics and the overlapping. WBCs are classified into five main shape groups with varying degrees of non-convexity and Granulometry may fail

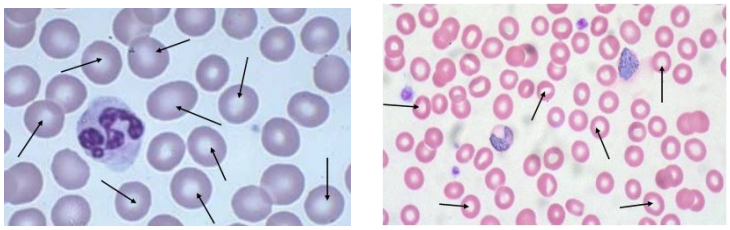

Figure 21: Patches and holes inside the RBC image

to estimate white blood cells size.

In conclusion, Area-Granulometry over normal erythrocytes is an acceptable size estimator as RBCs have:

- Uniform-Membrane.
- N-PDF(Normal PDF).
- Circular shape.
- High rate of density (The ratio of WBC to RBC is 1 or $2:100$)
- The maximum peak (the most redundancy and amplitude) in pattern spectrum (Granulometry result)
- Remarkable accuracy (based on Area - Granulometry)

This Area-Granulometry approach is not an efficient method for white blood cell size estimation. When it is applied, it may result in false and true negative values for both red and white blood cells. The following are the reasons that Area-Granulometry is not suitable for WBC size measurement.

- Variation in shapes (circular, elliptical)
- Low density in blood smear slides (few samples are in a given blood volume)
- Edge fracture effect (see Fig. 20)
- Intrinsic characteristics (not solid membrane).
- Nucleus and granular area.
- Variation in size ($1-3$ times of normal RBC)

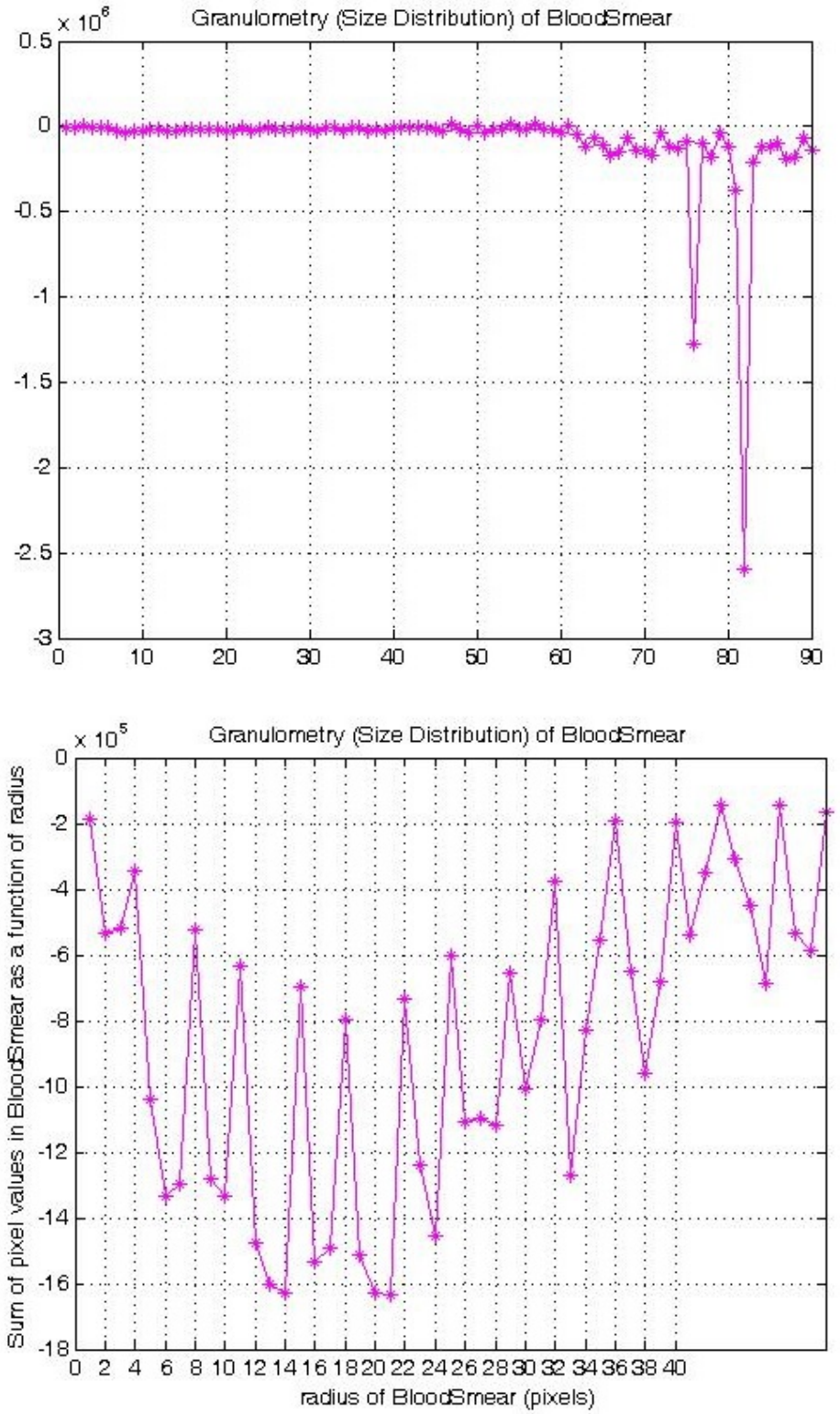

Figure 22: (Top to Bottom) a normal blood sample; an abnormal blood smear sample (size detector)

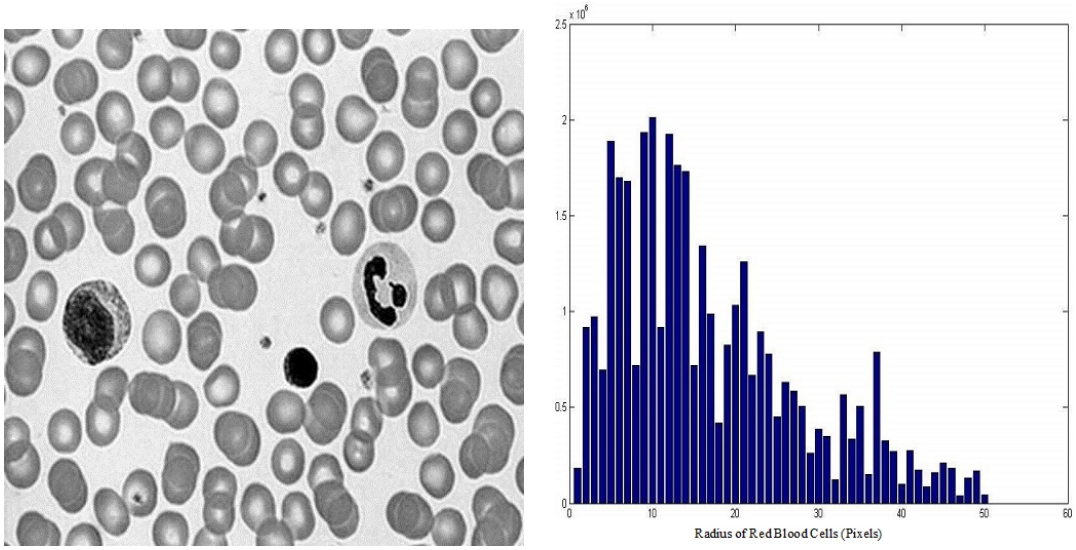

a b

Figure 23: (left to right): a) de-noised green channel of initial sample; b) Granulometry over blood smear sample (RBC size detector)

- Overlapped and adjacent RBC cells may address false WBC.

Overall, applying Area - Granulometry to RBCs images in normal blood smear can be reliable in determining and estimating their size. However, for abnormal samples with different shapes or with extra overlapping between the particles Granulometric approach may fail (see Fig. 22) [113].

4.3.3 RBCs & WBCs Separation

First, two sub-images composed of RBCs and WBCs are required. Size estimation discussed in the previous section (see sub-section 4.3.2) is also used here to achieve the accurate and precise cell separation. In normal blood smear images, all available particles are approximately circular. Hence, we select (disk) shape as default and basic structure element for Granulometric algorithm (previous section . 4.3.2).

A pipeline method for the accurate separation of leukocytes and erythrocytes in a simultaneous and cooperative way is proposed. This is done in two main procedures which are extracting a sub-image containing individual closed WBC regions, and also separating WBCs from RBCs [78]. The proposed separation algorithm is an iterative mechanism which is based on morphological theory, saturation amount and red blood

cell size. The computational cost of the following process is primarily affected by determining an effective mask to separate the WBCs from the RBCs.

- Extract sub-images containing individual closed WBC regions. The algorithm approximately determines the location of WBCs nucleus and enhances WBC boundaries.
- Use step-by-step iterative method based on RBC size estimation, circular mask, saturation value and noise removal to separate WBCs and RBCs into two individual sub-images to separate white blood cells from red blood cells.

Extracting a sub-image containing individual closed WBC regions: First, a sub-image containing WBCs is separated from the image generated at the end of step 5) of the framework. This is done in five steps: A) An approximate location of nucleus is found by keeping 70% maximum (S) value in HSV channel module over edge preserved image. B) A morphological dilation by RBC size (Granulometric pattern spectrum output) is performed over the discontinuous extracted dots (equal or greater than 70% maximum (S)) to estimate and close the entire possible connective WBC region. C) A square mask surrounding the center of mass of connective regions (after dilation) with the size of 2 $\times$ diameter of mass region is applied over whole image to extract sub-images including separated WBCs and somewhat near RBCs. D) Since the boundaries of the WBCs in the image after merging binarization and canny output may still be imprecise, a more accurate estimation of the WBC boundaries can be obtained by applying an active contour using the Chan-Vese implementation [29]. In this improved curve evolution method, cells and white blood cells in particular whose boundaries are not completely defined by gradient are detected and traced using active contour model where the stopping criteria term does not depend on the gradient and edged images, as in the conventional active contour models. On continuing work Canny edge detection to the resultant image is then applied. This edge detected image is then merged with the image generated at the end of step 5 and the interiors of the cells are filled pixel-wise in this merged image. E) As a post-processing step some small spurious regions is cleaned up by using a closing morphological transformation (SE size = 1 px).

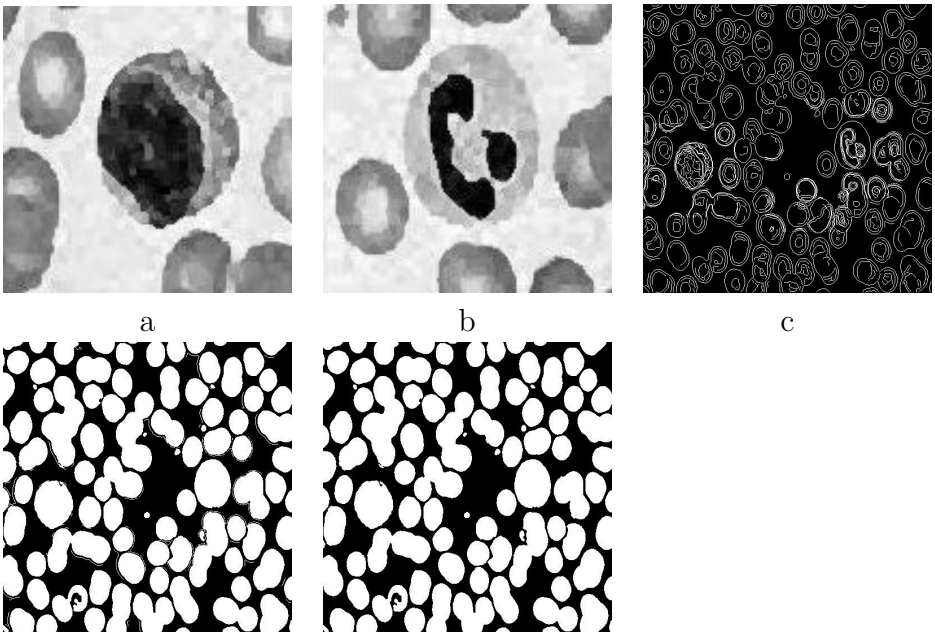

Figure 24: Extracting a sub-image containing individual closed WBC regions: a, b) Sub-images containing WBCs; c) Canny over Chan-Vese Active Contour Without an Edge; d) Adding new edged image and enhanced filled object; e) Modified filled object (closing SE=1px)

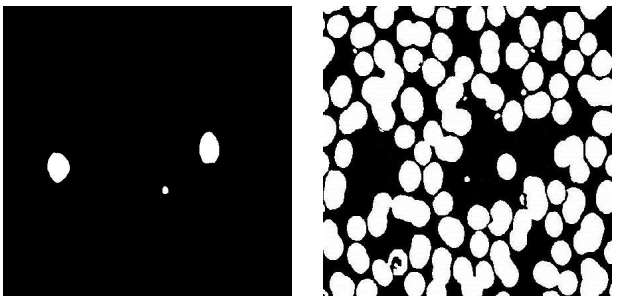

a b

Figure 25: Separating WBCs from RBCs: a) WBC indicator; b) Separated RBC sub-image

Separating WBCs from RBCs: Thus far, an image is formed with solid objects; before counting, WBCs and RBCs should be separated into two sub-images. This task could be done by a step-by-step iterative method: A) Apply granulometry over the blood smear image (with the RBC interiors filled in) and saving approximate RBC size. B) Initialize the possible available WBC size from expected physical characteristics and an acceptable marginal range: C1=80% *RBC size (as an initial marginal value). C) Moving the circular mask over blood smear image and detecting the exact matching objects of the same size. D) For those matched objects with any pixel with an S value greater than 70% of the maximum value (which indicates the presence of a nucleus here), all its pixel intensities are set to 0 (zero). E) Applying circular mask function in a closed loop by an initial radius value (C1=80% $\times$ RBCsize) and then moving the mask over all image pixels. F) Save the WBC indicator in a new image mask. G) Possible noisy remained region and speckles are removed by deleting closed objects less than $\frac{1}{3}$ RBC size. Two separated sub-images are seen in fig. 25. Proposed method has a computational cost when it determines an effective mask to disjoint all five main kinds of WBCs from the RBCs. In contrast, similar approach [46, 226] suffers from the drawbacks such as inability to deal with overlapping cells and also is not efficient for all possible five WBCs types including Basophil (fig. 1) which has may similar size to the red blood cells. A comparative results for two addressed methods are shown in fig. 26. As a result, it is obvious that area-opening does not cover overlapped objects and then it fails to segment white blood cells.

In another comparative study, authors in [80, 156, 160] proposed using typical

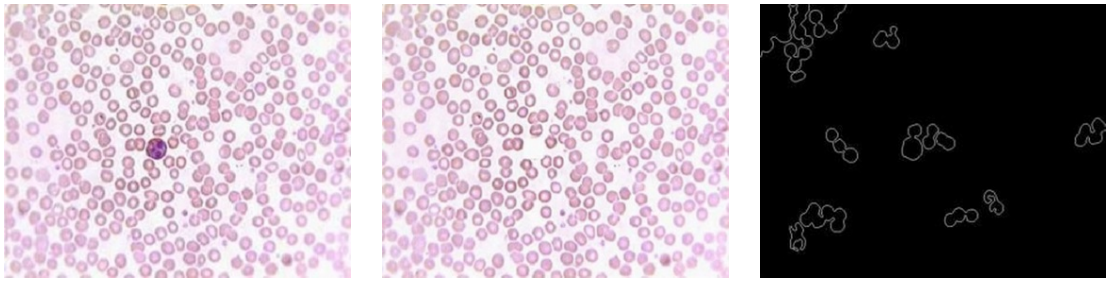

a b c

Figure 26: Separating WBCs from RBCs: a) Sample slide; b) RBC separated using this work ; c) Area- Opening [46]

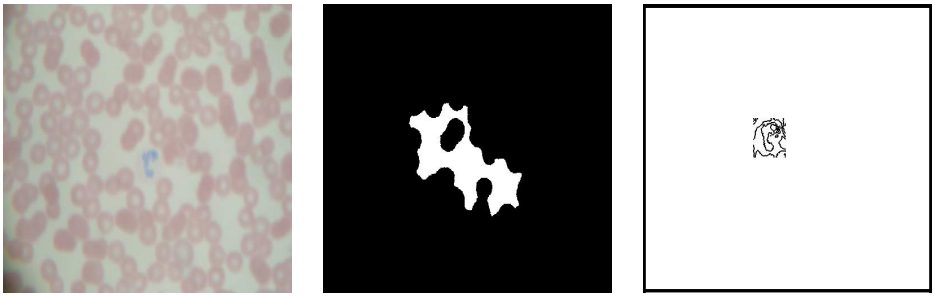

a b c

Figure 27: Separating WBCs from RBCs: a) Low quality sample ; b) WBC separated using active contour [80, 156, 160]; c) WBC separated using Active contours without edges [29].

active contour to segment white blood cell boundaries. Active Contour relies too heavily on presence of obvious gradient edge information. In this case, where because of a lack of solid white blood cell curve, evolving curves surrounding leukocytes will are be stopped out of the expected region like edges. Therefore this technique fails to resolve white blood cell segmentation for all possible conditions (see Fig. 27).

4.3.4 RBC Counting

We applied watershed [131] as an efficient approach which can handle overlapping cells (fig. 28) to count RBCs. The watershed is based on regions, which classifies pixels according to their spatial proximity, gradient of gray levels and homogeneity of textures. The accuracy and efficiency of segmentation over images is directly related to the previous steps such as they are addressed in image pre - processing

and segment closed objects. Performance and feasibility of the computed blood cell count results are compared with manual counts of RBCs and WBCs (the differences between the computed counts and the manual counts). Also, a set of different blood smear test images (see Fig. 2) with a variety of image characteristics were used to show proposed framework accuracy and robustness for degraded images which are blurry and/or noisy. In the last four rows (see Table 13), the images have had noise added to the images to test the robustness of our framework under extreme conditions. The results are compared with manual counts of the number of RBCs and WBCs, with the difference between the computed counts and the manual counts indicated by the numbers in parenthesis. The results show that our approach is closer to the actual counts, especially in noisy images showing that our denoising techniques lead to better results. In particular, WBC counts are much more accurate with our framework than with Di Ruberto et *al.* [44, 46] and their extended work [224, 225, 226] (a total of 1 miscounted, over-counted, WBC versus 23 for previous studies), while on the other hand, RBCs are frequently uncounted but to a smaller extent than the typical over-counts of the other techniques (a total of 80 miscounted RBCs versus 182 for previous work).

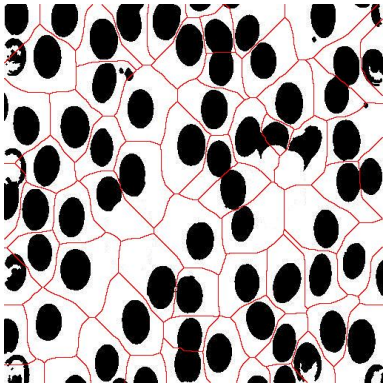

Figure 28: Watershed marker over blood smear image

4.3.5 Binarization & Cell Separation Settings

This section has been divided into two parts. The first part deals with binarization and then it go on to cell segmentation to count separately.

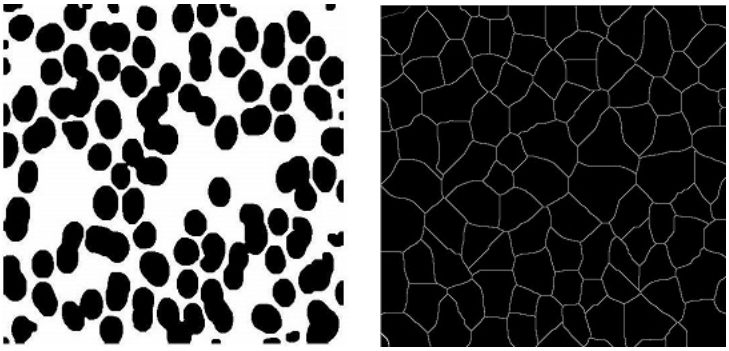

a b

Figure 29: Watershed for RBC counting: a) Solid RBCs; b) Watershed markers

Binarization

As for binarization, this research uses combination of Otsu and Niblack (see Section. 4.3.1). Niblack is a local threshold that uses a sliding windows with (15×15) and default k. This k is an adjustable parameter to separate pixels that belong to foreground. The default value is 0.2 for bright objects and -0.2 for dark objects. In current application as cells are almost darker than background we could use $k = -0.2$.

Cell Separation

As for cell separation, this work uses combination of techniques namely, Granulometry method, canny scheme and active contours without edges method, in order to track boundaries. Granulometry uses consecutive morphological openings in which minimum size is 1 pixel and end-point in this work is arbitrary set at 50. The initialized guess value that could be 2 or 3 times more than this. This value is calibrated using pattern spectrum outcome. In reality, end point first initialized from a larger value and then it reduces to a smaller number that we have output in pattern spectrum diagram (for example see Fig. 23). In this framework after trial and practice 50 is an appropriate marginal end-point for current dataset. Of course, it is very obvious larger number just only increase running time and there is no more burden than increasing computational time. Following cell separation (see Section 4.3.3), active contours without edges is addressed with following settings (see Table 12)

Table 9: Summary of normalized cross-correlation (NCC) data for each binarization algorithm performance in different conditions: (top to bottom) total over 10 regular images (N_0–N_9);

	10 Normal and regular images						
Algorithm	**Mean**	**Median**	**Mode**	**StdDev**	**Range**	**Min**	**Max**
Otsu	-0.0094	-0.0111	0	$0.9410 * 10^5$	1.0803	-0.1866	0.8937
Bernsen	-0.0096	-0.0101	0	$1.16 * 10^5$	0.7935	-0.2882	0.5055
Sauvola	-0.0111	-0.0150	0	$1.53 * 10^5$	0.6727	-0.2754	0.3973
Niblack	-0.0111	-0.0143	0	$1.468 * 10^5$	0.7328	-0.2654	0.4674
	10 moderate Gaussian Noisy images						
Algorithm	**Mean**	**Median**	**Mode**	**StdDev**	**Range**	**Min**	**Max**
Otsu	-0.0096	-0.0115	0	$1.9166 * 10^5$	1.0385	-0.1862	0.8522
Bernsen	-0.0098	-0.0107	0	$1.1905 * 10^5$	0.7262	-0.2882	0.4379
Sauvola	-0.01110	-0.0132	0	$1.36 * 10^5$	0.5429	-0.2554	0.2875
Niblack	-0.0107	-0.0112	0	$1.27 * 10^5$	0.5676	-0.2399	0.3277
	10 high Gaussian Noisy images						
Algorithm	**Mean**	**Median**	**Mode**	**StdDev**	**Range**	**Min**	**Max**
Otsu	-0.0100	-0.0110	0	$4.1870 * 10^5$	0.7052	-0.1933	0.5119
Bernsen	-0.0106	-0.0117	0	$1.2897 * 10^5$	0.6793	-0.2882	0.3911
Sauvola	-0.0103	-0.0113	0	$1.2073 * 10^5$	0.3996	-0.2263	0.1732
Niblack	-0.0102	-0.0110	0	$1.1962 * 10^5$	0.3937	-0.2173	0.1764
	10 moderate Speckle Noisy images						
Algorithm	**Mean**	**Median**	**Mode**	**StdDev**	**Range**	**Min**	**Max**
Otsu	-0.0094	-0.0112	0	$1.1551 * 10^5$	1.0696	-0.1863	0.8833
Bernsen	-0.0093	-0.0097	0	$1.1605 * 10^5$	0.7315	-0.2882	0.4433
Sauvola	-0.0111	-0.0144	0	$1.4113 * 10^5$	0.5226	-0.2704	0.2522
Niblack	-0.0107	-0.0124	0	$1.2886 * 10^5$	0.5755	-0.2476	0.3279
	10 high Speckle Noisy images						
Algorithm	**Mean**	**Median**	**Mode**	**StdDev**	**Range**	**Min**	**Max**
Otsu	-0.0089	-0.0103	0	$0.1483 * 10^5$	0.7766	-0.1630	0.6136
Bernsen	-0.0095	-0.0100	0	$1.1701 * 10^5$	0.6337	-0.2882	0.3454
Sauvola	-0.0103	-0.0115	0	$1.2037 * 10^5$	0.3574	-0.2326	0.1248
Niblack	-0.0100	-0.0109	0	$1.1847 * 10^5$	0.3817	-0.2211	0.1605
	10 blurry images						
Algorithm	**Mean**	**Median**	**Mode**	**StdDev**	**Range**	**Min**	**Max**
Otsu	-0.0093	-0.0109	0	$0.8049 * 10^5$	1.0766	-0.1863	0.8902
Bernsen	-0.0094	-0.0103	0	$1.1626 * 10^5$	0.8632	-0.2882	0.5749
Sauvola	-0.0111	-0.0155	0	$1.5747 * 10^5$	0.6492	-0.2794	0.3698
Niblack	-0.0111	-0.0147	0	$1.4936 * 10^5$	0.7084	-0.2683	0.4401

Table 10: Summary of normalized cross-correlation (NCC) data for each binarization algorithm performance in different conditions for sample separated WBCs: (top to bottom) total over 10 regular images (N_0–N_9); total over 10 moderate Gaussian Noise; 10 images with high Gaussian Noise; total over 10 moderate Speckle Noise; 10 images with high Speckle Noise; total over 10 regular blurry images (N_0–N_9)

	10 Normal and regular WBCs images						
Algorithm	**Mean**	**Median**	**Mode**	**StdDev**	**Range**	**Min**	**Max**
Otsu	0.0259	0.0459	0	$3.0834 * 10^5$	1.2122	-0.3870	0.8252
Bernsen	0.0262	0.0437	0	$0.3987 * 10^5$	1.1234	-0.4192	0.7042
Sauvola	0.0304	0.0390	0	$0.5008 * 10^5$	1.0516	-0.4021	0.6495
Niblack	0.0310	0.0383	-0.4320	$0.5222 * 10^5$	1.0942	-0.4320	0.6622
	10 moderate Gaussian Noisy WBCs images						
Algorithm	**Mean**	**Median**	**Mode**	**StdDev**	**Range**	**Min**	**Max**
Otsu	0.0269	0.0425	0	$2.7136 * 10^5$	1.2061	-0.4053	0.8008
Bernsen	0.0253	0.0424	0.1131	$0.4044 * 10^5$	1.0541	-0.3945	0.6596
Sauvola	0.0304	0.0398	0.0318	$0.4341 * 10^5$	0.8623	-0.3879	0.4744
Niblack	0.0310	0.0394	0.2240	$0.4601 * 10^5$	0.9226	-0.4163	0.5063
	10 high Gaussian Noisy WBCs images						
Algorithm	**Mean**	**Median**	**Mode**	**StdDev**	**Range**	**Min**	**Max**
Otsu	0.0255	0.0345	0	$1.5675 * 10^5$	0.9911	-0.3685	0.6226
Bernsen	0.0256	0.0359	0.0062	$0.4188 * 10^5$	0.9984	-0.3856	0.6129
Sauvola	0.0300	0.0381	0	$0.4072 * 10^5$	0.7184	-0.3628	0.3556
Niblack	0.0300	0.0379	0.1400	$0.4104 * 10^5$	0.7240	-0.3587	0.3653
	10 moderate Speckle Noisy WBCs images						
Algorithm	**Mean**	**Median**	**Mode**	**StdDev**	**Range**	**Min**	**Max**
Otsu	0.0274	0.0459	0.0933	$2.8116 * 10^5$	1.2477	-0.4250	0.8227
Bernsen	0.0254	0.0424	0	$0.3972 * 10^5$	1.0728	-0.4085	0.6643
Sauvola	0.0303	0.0388	0	$0.4386 * 10^5$	0.9395	-0.3915	0.5480
Niblack	0.0309	0.0377	0.2034	$0.4798 * 10^5$	1.0064	-0.4154	0.5910
	10 high Speckle Noisy WBCs images						
Algorithm	**Mean**	**Median**	**Mode**	**StdDev**	**Range**	**Min**	**Max**
Otsu	0.0243	0.0388	0	$1.0496 * 10^5$	1.0946	-0.3688	0.7258
Bernsen	0.0234	0.0361	0.0193	$0.3984 * 10^5$	0.9451	-0.3508	0.5944
Sauvola	0.0292	0.0357	0	$0.4047 * 10^5$	0.7086	-0.3541	0.3545
Niblack	0.0300	0.0368	0.0045	$0.4119 * 10^5$	0.7384	-0.3683	0.3701
	10 blurry WBCs images						
Algorithm	**Mean**	**Median**	**Mode**	**StdDev**	**Range**	**Min**	**Max**
Otsu	0.0250	0.0429	0	$2.8675 * 10^5$	1.2130	-0.4147	0.7983
Bernsen	0.0261	0.0438	0	$0.3980 * 10^5$	1.0870	-0.4347	0.6523
Sauvola	0.0311	0.0399	0	$0.5042 * 10^5$	1.1009	-0.4362	0.6647
Niblack	0.0319	0.0416	0.1646	$0.5334 * 10^5$	1.1329	-0.4742	0.6587

Table 11: Summary of normalized cross-correlation (NCC) data for each binarization algorithm performance in different conditions for windows sample including few disjoint close by RBCs: (top to bottom) total over 10 regular images (N_0–N_9); total over 10 moderate Gaussian Noise; 10 images with high Gaussian Noise; total over 10 moderate Speckle Noise; 10 images with high Speckle Noise; total over 10 regular blurry images (N_0–N_9)

	Normal and regular RBCs images						
Algorithm	**Mean**	**Median**	**Mode**	**StdDev**	**Range**	**Min**	**Max**
Otsu	0.0083	-0.0094	0	886.7119	1.1373	-0.2159	0.9214
Bernsen	0.0111	-0.0029	-0.0283	206.1605	0.9564	-0.2439	0.7125
Sauvola	0.0150	0.0114	0	216.3476	0.9460	-0.2852	0.6608
Niblack	0.0158	0.0153	0	227.5969	0.9023	-0.3206	0.5816
	moderate Gaussian Noisy RBCs images						
Algorithm	**Mean**	**Median**	**Mode**	**StdDev**	**Range**	**Min**	**Max**
Otsu	0.0087	-0.0094	0	774.9890	1.1128	-0.2203	0.8925
Bernsen	0.0124	-0.0007	-0.2535	207.6752	0.9120	-0.2535	0.6585
Sauvola	0.0147	0.0084	0	212.8327	0.8623	-0.2497	0.6126
Niblack	0.0155	0.0112	0	221.0434	0.8402	-0.2777	0.5626
	high Gaussian Noisy RBCs images						
Algorithm	**Mean**	**Median**	**Mode**	**StdDev**	**Range**	**Min**	**Max**
Otsu	0.0127	-0.0010	0	145.6640	0.7748	-0.2112	0.5636
Bernsen	0.0151	0.0057	-0.2599	226.7028	0.6677	-0.2599	0.4078
Sauvola	0.0146	0.0068	0	209.7879	0.6003	-0.2302	0.3701
Niblack	0.0149	0.0091	0	211.5264	0.6039	-0.2403	0.3636
	moderate Speckle Noisy RBCs images						
Algorithm	**Mean**	**Median**	**Mode**	**StdDev**	**Range**	**Min**	**Max**
Otsu	0.0083	-0.0095	-0.0061	879.6408	1.1249	-0.2126	0.9123
Bernsen	0.0111	-0.0032	0	206.1431	0.9394	-0.2420	0.6974
Sauvola	0.0146	0.0091	0	212.3325	0.9249	-0.2798	0.6451
Niblack	0.0156	0.0140	0	223.6009	0.8827	-0.3049	0.5779
	high Speckle Noisy RBCs images						
Algorithm	**Mean**	**Median**	**Mode**	**StdDev**	**Range**	**Min**	**Max**
Otsu	0.0093	-0.0050	0	958.8368	0.8862	-0.1965	0.6896
Bernsen	0.0122	-0.0017	-0.0307	206.7132	0.8003	-0.2375	0.5629
Sauvola	0.0146	0.0054	0	208.1570	0.6578	-0.2358	0.4220
Niblack	0.0149	0.0068	0	210.8861	0.6416	-0.2428	0.3988
	blurry RBCs images						
Algorithm	**Mean**	**Median**	**Mode**	**StdDev**	**Range**	**Min**	**Max**
Otsu	0.0078	-0.0100	-0.0107	917.8296	1.1215	-0.2050	0.9165
Bernsen	0.0112	-0.0023	-0.0470	206.2240	0.9465	-0.2406	0.7059
Sauvola	0.0151	0.0111	0	218.9666	0.9408	-0.2918	0.6490
Niblack	0.0159	0.0155	0	233.7550	0.8839	-0.3247	0.5592

Table 12: Boundaries detection: Settings

	Active contours without edges	
Parameter	**Value**	**Comment**
Mask	Small	Create a small circular mask to track gradient.
NumIter	1500	Total number of iterations that is a trade-off between computational complexity and contour accuracy.
M_u	0.1	Weight of length term.
Method	Multi phase	2-phase segmentation of the image is applied to detect both contours with, or without gradient.

Table 13: Experimental results of ten different blood smear images (numbered N0 – N9). Counts for RBCs and WBCs are given from manual counts, as well as by our framework using either Bivariate, or Gabor Wavelet. Values given in parentheses are the differences between counts computed and those obtained by a manual count (negative values indicate under-count; positive values indicate over-count). The last column labelled Subtypes refers to the WBC subtypes. In addition, the results are compared to those of the work [18, 44, 46] and their extended work [224, 225, 226].

Image #	**Image Characteristics**	**Manual Count**		**Our Framework using Gabor Wavelet [57] denoising Count (error)**		**Our Framework using Bivariate [205] denoising Count (error)**			**The Framework of Tek [226] *et al.* Count (error)**		**Subtypes**
		RBC	**WBC**	**RBC**	**WBC**	Smooth	**RBC**	**WBC**	**RBC**	**WBC**	
N0	Normal sample	104	1	98(-6)	1(0)	0.1	98(-6)	1(0)	122(18)	4(3)	1/1
N1	Without WBCs	75	0	68(-7)	0(0)	0.1	68(-7)	0(0)	78(3)	0(0)	-/-
N2	Blurred and Overlapped	125	2	115(-10)	2(0)	0.1	117(-8)	2(0)	152(27)	2(0)	2/2
N3	Normal sample	105	3	99(-6)	3(0)	0.1	99(-6)	3(0)	122(17)	9(6)	2/3
N4	Blurred	325	1	314(-11)	1(0)	0.1	312(-13)	1(0)	283(-42)	15(14)	0/1
N5	Blurred	66	2	62(-4)	2(0)	0.1	60(-6)	2(0)	90(24)	1(-1)	1/2
N6	Numerous Overlapping	90	2	78(-12)	2(0)	0.1	77(-13)	2(0)	100(10)	3(1)	2/2
N7	WBCs touch RBCs	18	1	16(-2)	1(0)	0.01	16(-2)	1(0)	35(17)	2(1)	1/1
N8	WBCs touch RBCs	69	2	65(-4)	2(0)	0.1	65(-4)	2(0)	81(12)	5(3)	2/2
N9	Blurred, Numerous overlapping, WBCs touch RBCs	101	1	83(-18)	2(1)	0.1	83(-18)	2(1)	108(7)	4(3)	0/1
N6	Additive Medium Noise	90	2	78(-12)	3(1)	0.1	78(-12)	2(0)	136(46)	4(2)	2/2
N9	Additive Medium Noise	101	1	83(-18)	2(1)	0.1	80(-21)	1(0)	93(-27)	4(3)	0/1
N6	Additive High Noise	90	2	70(-20)	1(-1)	0.1	65(-25)	2(0)	12(-78)	4(2)	0/2
N9	Additive High Noise	101	1	73(-18)	5(4)	0.1	70(-21)	2(1)	56(-64)	5(4)	0/1

4.4 Comparison of the Proposed Approach to the State-of-the-Art

Comparative studies on state-of-the-art are divided into binarization and blood cell segmentation.

4.4.1 Binarization

To date, the blood smear studies are more about global thresholding methods than local thresholding methods. Published work on blood segmentation [15,44,46,224,225, 226,242] use well-known Otsu global thresholding approach. The existing global Otsu thresholding value fails to resolve different conditions that exist in blood slide images. Inconsistent initial conditions may cause an abrupt change in global thresholding value and the binarization cannot construct a consistent system of foreground and background separation. Finding a global value as thresholding to separate the image into two separated regions of blood cells (RBCs in particular) and background (stained plasma) is not always simple and perhaps not even possible. It may cause false negative (FN) result in foreground detection (see Table 13). Global thresholding is with a serious weakness, however, is that much known but also it does not manage image binarization with nearby background and foreground intensity values range (see Fig. 19). Closely positioned pairs of particles will be merged into single particles, regardless of any fine tuning of the value of global thresholding. It is obvious that merged cells may cause false negative (FN) in RBCs detection (see Fig. 19). Overall, Otsu is a parameterless method to remove background details such as found in stained plasma background. However, it is non-adaptive to retain cells as they are foreground.

This work suggests to use combination of global and local thresholding to reach higher similarities between original and binarized converted images (see Table. 11). Merging Otsu and Niblack alleviates built-in problems in presence of adjacent cells and background variety.

4.4.2 Cell Separation

In an important work Di Ruberto et *al.* [44,46] and their extended work [224,225,226] authors addressed classical area opening morphology technique to separate between

WBCs and RBCs. Authors claimed that white blood cells can be separated by a morphological erosion with a disk-shaped structuring element whose size is achieved by the granulometric analysis (RBC size). Despite the simplicity of implementation and understanding, proposed method suffers from several major drawbacks. First, all white blood cells are not always bigger than a normal RBC size as Basophil which is about RBC size (see 4th image in top row in fig. 10). Secondly, overlapping phenomena among cells is also possible and it is a normal incident in blood smear slides. Therefore, these work findings cannot be extrapolated to all sample slides and these results therefore need to be interpreted with caution. A generally accepted framework of cell segmentation is lacking (see Fig. 26). Other work [80, 156, 160] addresses to use nucleus and its surrounding active contour and level set to separate WBCs in which generalization of these methods are very questionable in different conditions. First and foremost weakness backs to regular nature of leukocyte boundaries, lack of obvious edge for WBCs and low quality in nucleus presentation. In the classical active contour models an edge-detector is highly used to stop the evolving curve on the boundary of the desired white blood cell. However, WBC boundaries are not ideally defined by gradient in low quality images and it easily make false segmentation (see Fig. 27). Secondly, initial contour location is needed and should be close to the white blood cell that is to be segmented. Authors in [208] proposed fuzzy cellular neural networks (FCNN) to detect white blood cell. The principal are combination of fuzzy logic, and neural networks. Neural network uses enough number of different samples to give optimal generalization and update properties of back-propagation. This approach is not practical with this limited available dataset, i.e. 28 samples per each white blood cell class. In practice, having big data is not easy to address in medical projects.

This research is dealing with blood smear images segmentation using a step-by-step iterative method. More information is addressed in section 4.3.3. This framework can be extrapolated to all five mature white blood cells including Basophils. This step-by-step method managed faded white blood cell boundaries in this difficult dataset with active contours without edges and canny detection on top of that. It built a closed curve delineating a white blood cell despite of detecting these edges in other work [80, 156, 160]. It also managed overlapping incident that is common between RBCs in particular. However, it should be noted that the method and results

presented here in this work are only applicable for normal microscopic blood images. This algorithm may fails in presence of abnormal conditions such as Malaria.

4.5 Binarization & Cell Separation Contributions

Another contribution is the procedure developed for obtaining optimum binary images from mono-chromic channel with inhomogeneous background regions by creating a merged local and global binarization. This procedure is efficient and promising for all types of captured blood images with different conditions. This binarization algorithm is an important improvement as the previous work in this field used global thresholding approaches, i.e. Otsu, that these global findings cannot be extrapolated to all possible blood smear images (see Section 4.4.1). In addition, the study has gone some way towards enhancing our understanding of faded boundaries problem in white blood cell separation (see sub-section 4.3.3 and figure 27). Taken together, these findings suggest a role for active contours without edges in white blood cell segmentation for all classes.

4.5.1 Binarization

To date, the blood smear researches are more about on global thresholding methods rather than local thresholding methods. This work addresses to use combination of global and local thresholding to reach higher similarities between original and binarized converted images. The missing cells in global approach is enhanced using this merged technique, for which the local thresholding gives the required foreground as cells. The method used for this blood smear study may be applied to other histopathological images also. Comparative study and discussion is found in section 4.4.1 and figure 19.

4.5.2 Cell Separation

This research is dealing with blood smear images segmentation using a step-by-step iterative method. White blood cells are localized and segmented with reference to improved binarization, edge detection, saturation value, RBC size estimation, circular morphological mask, active contours without edges, and noise removal. More

information is addressed in section. 4.3.3. This framework can be extrapolated to all five mature white blood cells including Basophils. This step-by-step method managed faded white blood cell boundaries in this difficult dataset with active contours without edges and canny detection on top of that. It built a closed curve delineating a white blood cell despite of detecting these edges in other work [80, 156, 160]. It also managed overlapping incident that is common between RBCs in particular.

Comparative studies and discussion is addressed in section 4.4.2. In addition, it should be noted that the method and results presented here in this work are only applicable for normal microscopic blood images. This algorithm may fails in presence of abnormal conditions such as Malaria.

Chapter 5

Feature Extraction For WBC Classification

Image feature extraction has been established for years and has been used in many diverse pattern recognition and image processing fields. However, choosing efficient features for the detection of white blood cell from pathological images is significant problem. The main task of the feature extraction is to choose strongest connected correlated with the recognized classes. The main goal of feature extraction is to identify the strong features, i.e., the features with high discriminatory power. The aforementioned features can be grouped into *three* categories: *shape*, *intensity*, and *texture features*.

5.1 Problem Statement

This research aims to improve WBC type recognition even in presence of poor quality or low magnification images (see Fig. 1). In order to distinguish among white blood cells types, we need to extract features from the WBC sub-images and compute new features that lead to better separability of classes by classifiers. Features should be easily computed, robust, insensitive to various distortions and variations in the images, and rotationally invariant.

Features Combination:

Combining all individual features together allows to compensate error rates and also it increases their classification reliability to some extent. Features are generated using

different transformation parameters and also are evaluated to select the set with best discrimination power.

Features Reduction:

To reduce excessive dimensionality of different features, linear or non-linear combinations of features are applied through projection of the high-dimensional data on lower dimensional space to optimize the accuracy of classifier and it also reduces computational cost. To maintain the optimal features and components, non-linear dimensionality reduction methods under different names and algorithms have been introduced. They include PCA [96], locally linear embedding (LLE) [196] and graph embedding [254].

Numerous studies have attempted to explain these feature reduction techniques However, limited work has been able to draw attention to feature selection algorithms. In this study, we use feature selection algorithms described in section. 6.

5.2 Literature Review

The literature on automatic leukocyte segmentation and classification involves different descriptors and sub-class classification. Section 2.2.2 reviews the literature concerning white blood cell in connection with different approaches. These studies are based on active contour, fuzzy logic, morphological operations and feature extraction.

5.3 Research & Experimental Results

All invariant features are scaled between 0 and 1 to simplify computational complexity and have consistent inputs for measurement. As a result the final features vector has a total of 12104 coefficients for each white blood cell image with 28×28 low size. We use feature vector based on three main group features that it includes different invariant features such as four main intensity histogram calculations, the set of 11 invariant moments, the relative area, the co-occurrence, run-length matrices, the dual tree complex wavelet transform, Haralick and Tamura features.

5.3.1 Intensity Features

The Gray scale intensity values are used to extract efficient features for white blood cell classification. This work examines the mean (μ), standard deviation (σ), skewness (γ_1), and kurtosis (K) of white blood cells intensities. These features are based only on the absolute value of the intensity measurements in the segmented white blood cell images. A histogram describes the occurrence relative frequency of the intensity values of the pixels in a white blood cell image. The intensity features that we will consider are the first four central moments of this histogram: Mean, Standard deviation, Skewness, and Kurtosis [193]. The mean (μ) gives an estimate of the average intensity level in the region of the cell and the standard deviation (σ) is a measure of the dispersion of intensity. Skewness (γ_1) is a measure of histogram symmetry while kurtosis (K) is a measure of the tail of the histogram. Intensity features may prove inadequate for specially low quality white blood cell data set. For this dataset, other features such as the shape, and texture features may be useful for improved white blood cell classification.

5.3.2 Shape Features

In image processing and pattern recognition, two types of shape descriptors are used: *contour-based* and *region-based*. The former provides the objects external border information where they ignore the shape of the interior content. The latter considers both boundary and the interior of the digital shape.

Several studies investigating contour-based descriptors have been carried out on different algorithm names. Examples to contour-based shape descriptors includes chain code algorithm which is the first approach for representing connected external curves [61]. Other option is Fourier descriptors which exploit shape signatures in Fourier coefficients. It represents shape in a frequency domain [68, 100, 171].

The object boundary contours can be also extracted through curvature scale space [145, 146]. B-spline curve approximation is sum of pixels under a given criterion which optimally approximates the original object curve [70]. Polygon decomposition is a structural shape representation where boundaries are first sub-divided into line segments by polygon approximation [169, 202]. Furthermore, a number of other investigations into the contour-based shape descriptors are also addressed such as perimeter, compactness ($\frac{perimeter^2}{area}$), eccentricity (a measure of aspect ratio; length

of major axis to minor axis), Hausdoff distance (a measure of similarity) [53], and autoregressive (estimate the image model by prior knowledge) [52].

All these mentioned contour-based descriptors reviewed so far cannot represent ideally white blood cell shapes for which the complete and continuous boundary information is not ideally available with granular and non-uniform borders.

Also, questions have been raised about the validity and reliability under the constraints of translation, rotation and uniform-scaling invariance properties. Region-based shape descriptors derive benefit from both boundaries and interior pixels and that is why it would be an appropriate candidate for white blood cell detection at low resolution.

Invariant Moment-based Features

In reviewing the literature, the current study found that among different various shape features are often named, invariant moment as a region-based calculation which can provide invariant characteristics under different conditions are likely occur. Although moment algorithms and theory have been well established in mathematics, far too little attention has been paid to use of invariant moment in computer-aided diagnosis (CAD) in medical imaging and for blood smear analysis in particular. This research has given an account the reasons for the widespread use of *(11)* different invariant moments (are listed below) over white blood cells images with 28×28 pixel size.

The Hu set of Invariant Moments:

In the decade 60, a set of *seven* invariant moments was given by Hu [91, 151]. Shape feature variables computed from normalized centralized non-orthogonal moments up to order three. Hu set moments are one of the most widely used groups of invariant moments and have been extensively used for decades in pattern recognition. However, a major problem with this application is information redundancy. Mathematical terms are defined in [91, 151].

These Hu set invariant moments (IM) are invariant to shape changes in rotation, scaling and translation. It can be used for disjoint objects as well such as granular white blood cell cytoplasm (non-continuous and discrete borders), 3-4 lobed nucleus Eosinophil, bilobed nucleus Basophil, partially two lobes Lymphocyte; which are available in joint or disjoint form and appearance in normal white blood cells. However, it should be noted that higher-order Hu set moments are sensitive to noise and

they suffer from information redundancy.

The Orthogonal Polynomials Moments:

Discrete orthogonal moments (OM) are approaches to lessen information redundancy drawback and shortcomings. Our work will review the research conducted on the following orthogonal polynomials moments. In reviewing the literature, authors carried out a number of investigations into using the following invariant moment in pattern recognition. However, very little was found in the literature on the question of using moment in medical imaging. Zernike [128], Generalized Pseudo-Zernike [250], Fourier-Chebyshev [172], Fourier-Mellin [207], Radial Harmonic Fourier [187], Dual Hahn which are a complex set of Tchebichef and Krawtchouk moments [108], Discrete Chebyshev [150], Krawtchouk [256], Gegenbauer [89], Legendre [62, 261] are orthogonal moments investigated in our research. A brief comparative study of invariant moment approaches is summarized in table 14.

Brief review of invariant orthogonal moments in image processing: This section reviews the literature concerning the usefulness of using moment concepts in pattern recognition. This review has been divided into eleven parts. The first part deals with already published work in Zernike moment and then it looks at how other consecutive ten moments are addressed in literature review.

In recent years, several studies investigating Zernike orthogonal moment have been carried out on blood smear images. In 2006, Asadi *et al.* published a paper [9] in which they described Zernike moments in correspondence with leukemia cell classification. In 2011, Apostolopoulos *et al.* [6] pointed to some of the ways in which actual RBC sizes is estimated using Zernike feature sets with repetition degree $n = 6$ and different polynomial orders. In addition, in 2013, Das and co workers [39] demonstrated that Zernike features propose shape-based red blood cells characterization in anaemia.

In the second part, to date several studies have produced estimates of Pseudo-Zernike and Generalized Pseudo-Zernike, but there is still insufficient data for medical images. In preliminary work on Pseudo-Zernike and Generalized Pseudo-Zernike moments, different authors have measured these moments in a variety of face recognition methods. In 2003, Haddadnia *et al.* [79] published a paper in which they described the effect of orders of Pseudo-Zernike moment invariant to recognize human faces

with Radial Basis Function neural network. Three years later, Pang *et al.* [257] investigated the impact of Pseudo-Zernike moments to improve Fishers linear discriminant functionality where both, Pseudo-Zernike moments and Fishers linear discriminant are applied in sequence to derive a lower-dimensional feature vector to maximize the between class scatter, while minimizing the within-class scatter. The results demonstrated that this combination is an efficient way when there are inadequate samples in face recognition task. In 2008, Nabatchian *et al.* [153] reported face recognition in connection with Pseudo-Zernike moment invariant and different known k-nearest neighbours (kNN), Support vector machine (SVM), and hidden Markov model (HMM) classifiers for FERET face database. This dataset consists of 14051 grayscale face images from 1209 people with different conditions in illuminations, and facial expressions. In 2009, Rajwa *et al.* [180] pointed to some of the ways in which different bio-particle types including Listeria, Salmonella, Vibrio, Staphylococcus, and E. coli were classified using results obtained from pseudo-Zernike moments and classification was done using support vector machines (SVM), Fisher linear discriminant (FLD) and Bayesian maximum likelihood classifier (ML).

Rajwa and co-authors also performed a similar series of experiments in their own work to prove that bio-particles classification accuracy and efficiency [181, 182].

Few studies investigating Generalized Pseudo-Zernike orthogonal moment have been carried out on image recognition. The research to date has tended to focus on Pseudo-Zernike rather than Generalized Pseudo-Zernike. Analysis of Generalized Pseudo-Zernike involved in face recognition was first carried out by Herman *et al.* [87] in 2009. Authors proposed feature extraction based on Generalized Pseudo-Zernike moment and then their framework was evaluated using radial basis function neural network (RBF-NN) Classifier in which results showed that the Generalized Pseudo-Zernike is superior to Zernike and Pseudo-Zernike moments. There are articles [33, 209] which are survey work on Generalized Pseudo-Zernike moment and other orthogonal moments in medical imaging application. However, using Generalized Pseudo-Zernike moment and other alternative options still remain marginal in medical pattern recognition tasks.

In the third review, to date there has been some published work on using Legendre moment in pattern recognition terms and medical imaging. Preliminary known work on Legendre moment was undertaken by Bailey *et al.* [12] which provides in-depth

analysis of using Legendre moment showing its efficiency for handwritten Arabic numerals. The study in 2011 [229] was to evaluate and validate noise robustness of Legendre moments on medical X-Ray Images.

After that, various pieces of research using Radial Tchebichef moment in image processing and pattern recognition are addressed. The study in 2013 [137] was to compare and validate texture classification using discrete Tchebichef moments conducted on three known databases: Brodatz, Outex, and VisTex. Discrete orthogonal Tchebichef moments with combination of Fisher linear discriminant (FLD) analysis are used as a face recognition method [230]. The study in [166] was to investigate the performance of six orthogonal moments including Tchebichef moments in brain and knee reconstruction for images captured under different views. In a comparative study [92], an approach for the detection of global image modifications based on a set of Tchebichef moments features in connection with different medical imaging (MRI, X-Ray) was introduced.

Afterwards, several attempts have been made to use Krawtchouk moment in characterizing image shapes for computer vision and medical image analysis applications. Bing Hu *et al.* in 2013 [90] have recently developed a methodology for Chinese character recognition using Krawtchouk moment. Classification of benign and malign masses in mammograms is followed using Zernike and Krawtchouk moments by a k-nearest neighbour strategy where the results showed that Krawtchouk reached an accuracy rate of 90.2% compared to 81% for Zernike moments [154]. A comparative study of moments including Legendre, Zernike, Tchebichef and Krawtchouk for CT liver tumor scan and prostate ultrasound image analysis is addressed in [248]. The experimental have shown that high performance can be achieved by using Krawtchouk in comparison to other alternative approaches.

To date, there has been very little published work on using Fourier-Chebyshev moment in pattern recognition terms. In 2002, Ping and his co-workers published a paper [172] in which they described 26 English alphabet letters image reconstruction using invariant Fourier-Chebyshev moment. Authors also conducted a series of trials to assess sensitivity to noise robustness with using Fourier-Chebyshev in comparison to performance of the FourierMellin moments. In reviewing the literature, no data was on the question of using Fourier-Chebyshev in medical image processing.

Some studies have attempted to explain the Fourier-Mellin moment pattern recognition applications. Singh *et al.* (2001) [227] in analysis of face and non face binary classification, have attempted to draw attention to usefulness of Fourier-Mellin moment with support vector machine to categorize all inputs into two face or non-face classes. To achieve promising digital image edge location accuracy, Bin *et al.* examined Fourier-Mellin moments with different orders and degrees to detect the image edges [19]. In Liu *et al.* work (2011) [132], Fourier-Mellin moment has been applied to blurred color fish images to evaluate the efficiency and invariance performance of the Fourier-Mellin moments for deformed gray scale images with respect to different blurring distortions and additive noise levels. Wang *et al.* (2013) [243] have recently developed a methodology for the selective introduction of mechanics to avoid redundant data in full-field measurements such as image decomposition and reconstruction. In spite of appropriate local and global characteristics of Fourier-Mellin polynomials, previous studies of pattern recognition using Fourier-Mellin polynomials have not dealt with medical imaging and computer aided diagnosis (CAD) framework and this is the motivation for this work.

Although Gegenbauer polynomials have appropriate local and global built-in characteristics, few studies exist which adequately cover different image processing applications. Liao *et al.* (2002) [130] analysed Chinese characters and concluded that, in presence of much large and difficult Chinese characters with high similarity levels in shape, two different characters are effectively distinguished by lower orders of (α) invariant Gegenbauer moment. This work conducted a series of 6763 Chinese characters, saved in 24×24 pixels with the font of Song, as the testing images. Archibald *et al.* (2003-2004) [7, 8] reviewed the literature concerning the usefulness of Gegenbauer image reconstruction method to improve the quality of segmentation in magnetic resonance imaging (MRI). So far, there has been little discussion about Gegenbauer moment implementation in medical pattern recognition terms and further research should be done to investigate.

Furthermore, Ren *et al.* (2003) [187] reviewed the research conducted on reconstructed images of the English letters with 64 Radial Harmonic Fourier moments with different orders and with repetition factor ($n = 8$). Ren *et al.* [185] performed a similar series of experiments in 2007. It begins by laying out the theoretical aspects of the

Radial Harmonic Fourier moment, and then it looks at how to investigate and compare the properties of Radial Harmonic Fourier moment and Fourier-Mellin moment in detection of a set of gray-scale four Chinese characters with real noises. both Radial Harmonic Fourier moment and Fourier-Mellin moment generally have the same Fourier factor in angle direction ($exp(\jmath n\theta)$). However, the radial functions are different. Singh *et al.*(2013) [211] reviewed recent research on the efficient water marking scheme using Radial Harmonic Fourier moments. The proposed image watermark is performed using Radial Harmonic Fourier moment magnitudes to minimize the added host image spatial distortion.

In addition, very little research has been found that surveyed with Radial-Harmonic-Fourier moments in medical imaging. Again, Ren *et al.* (2003) [186] gave an account of Radial-Harmonic-Fourier moments in the recognition of cell smear images. This Radial-Harmonic-Fourier moment makes several noteworthy contributions to image analysis and further investigation and experimentation into medical image processing is strongly recommended.

Following to literature review, this work reviewed the literature from the period and found little evidence emerged for the role of Hahn or Dual Hahn moments in image processing and pattern recognition. However, no attention has been paid to medical imaging recognition. Ahmad *et al.* (2009) [2] studied the effects of Hahn moment on image watermarking techniques. Their work was about to design an effective and robust watermarking system that could lessen geometric-distortions as well as different common watermark attacks. Ananth *et al.* (2012) [5] conducted a series of YALE and FERET human face database in which he examined the Dual Hahn moment, Racah moment and Tchebicef moment with different available face conditions expressed facial expressions, lighting conditions. Ananth Raj (2013) [179] used discrete Dual Hahn moment to develop a contrast enhancement system in presence of monochrome and color images. To compare performance evaluation of enhancement techniques; three index; image entropy, coefficient information content and universal quality index were calculated where the results were extracted using Dual Hahn, Kratchouk, Tchebichef moments and Alpha rooting.

Consequently, after reviewing the literature, several studies [8, 9, 12, 19, 33, 39, 79, 90, 92, 132, 137, 172, 182, 185, 187, 209, 211, 248] have produced estimates of invariant

orthogonal moments in pattern recognition but there is still insufficient data for medical imaging. This lack of a comprehensive study in medical imaging has existed for years.

To date, it is apparent that very few works on blood smear detection use Zernike [39] and Radial Harmonic Fourier [186] moments. This study sets out with the aim of assessing the importance of invariant moment features in white blood cell classification in presence of very low quality dataset. Further data collection is required to determine exactly how invariant moments affects feature extraction in microscopic blood smear images.

Zernike Moment: Zernike moments [127] are given in the polar coordinates; magnitude and phase. Rotating a digital image would not change the magnitude. Due to this property, the magnitude of Zernike moments has been used as a shape feature in image processing applications. It can be observed that accuracy and performance rate would be improved significantly when the order (m) increases as it expected.

Generalized Pseudo-Zernike Moment: Generalized Pseudo-Zernike polynomials [249, 250] are an expansion of the conventional pseudo-Zernike polynomials where basis function is also along with a free $\alpha \geq 1$ parameter to adjust zero points of real-valued radial polynomial.

Legendre Moment: This moment provides scale and translation invariant characteristics and it could cover different angle capturing as well. Furthermore, we can observe significant performance in analyzing small size images using Legendre moment [62, 261, 264].

Discrete Krawtchouk Moment: Studies addressed, in this work, so far suffer from the fact that the Legendre and Zernik approaches fail to take digitalization error into account. When the order (m) of the moments increases, this digitalization error apparently occurs. Subsequently, this change makes a decrease in the exactness of the computed components moments. Oh the other hand, Krawtchouk moment [256] does not need a discretization because it is based on discrete Krawtchouk polynomials. Following that, Krawtchouk moment has recursive and symmetry properties. These properties lead to ease the computational cost [256]. kp_1 and kp_2 are varying parameters associated with the Krawtchouk polynomials to extract local properties.

Radial Tchebichef Moment: Radial Tchebichef moment brings invariance and

orthogonality characteristics. In this term, kernel is defined using Tchebichef polynomials with radial-polar coordinate like to Zernike moments [149]. In general, radial moments provide rotational invariance by considering only magnitude and ignoring phase component.

Fourier-Chebyshev Moment: This combined set is based on the Fourier transform and Chebyshev polynomials in a given orthogonal moment function. It brings appropriative properties such as symmetry property, recurrence relation that can be effectively used in image analysis, image reconstruction and computing efficiency [124, 172].

Fourier-Mellin Moment: This defined radial polynomials [207, 212, 244] bring more zeros in the region of small radial distance and as a result it leads to present small images in better representation.

Gegenbauer Moment: Gegenbauer ($G_n(x;\alpha)$) or ultra-spherical polynomials represent a large and growing body of orthogonal polynomials with a scaling factor ($\alpha > -0.5$) adjustment [89]. The most obvious finding [89] to emerge from this ultra-spherical polynomials is that a global characteristic is determined with a small (α) whereas local image features with large value of (α) is extracted. In this work, the evidence from granular, complex and disjoint white blood cell membrane suggests that a Gegenbauer moment implementation with low value of (α) should be carried out on dataset to preserve global white blood cell information.

Radial Harmonic Fourier Moment: Initially, it is based on a polar coordinate function, radial polynomial and Fourier transform. This method profits combination of Mellin transfer order, and Fourier transfer. Therefore, Radial Harmonic Fourier moment is rotational, scaling and intensity distortion invariant [187].

Discrete Dual Hahn Moment: Dual Hahn polynomials [266] bring minimal information redundancy. In addition, discrete structure provides numerical stability and it does not need for continuous to discrete numerical approximation. Dual Hahn polynomials provide properties such as recurrence relation, symmetry, scale and rotation invariant to facilitate the computation of moments. In general, the dual Hahn polynomials are a set of orthogonal polynomials with more adjustable parameters ($\alpha_1 \geq 0,\ \alpha_2 > -1$) than Tchebichef and Krawtchouk moments to provide more flexibility in describing the digital image.

Table 14: Comparative Study of Invariant Moment Approaches

Moment Name	Short Definition	Benefits	Literature review in medical image processing	Comment
Hu set	A set of *seven* invariant non-orthogonal moments up to order *three* given by Hu [74, 91]	Invariant to rotation, scaling and translation.	Hu set moment is the most widely used group of invariant moments in image processing [74]	Sensitive to noise and provides information redundancy.
Zernike	A set of continuous complex orthogonal Zernike polynomials [127].	Zernike moments are given in polar coordinates; magnitude and phase where magnitude value is a rotation invariant feature with no redundancy.	Several studies have been carried out on blood smear images [9, 39].	When order (m) of the moments increases, this change makes a decrease in accuracy. Furthermore, because of digitalization, large variations need to be transformed resulting in a high computational cost.
Generalized Pseudo-Zernike	An extended orthogonal pseudo-zernike polynomials which are defined on the continuous unit circle ($x^2 + y^2 = 1$) [249, 250].	A free $\alpha \geq 1$ parameter is used to adjust zero points of real-valued of radial polynomial to, in turn, provide better feature presentation.	Little information was found on the association between pseudo-Zernike and medical imaging [180, 181, 182].	Discretization process is required to apply.
Legendre	Extended continuous orthogonal Legendre polynomials which provide scale and translation invariant characteristic [62].	Modified Legendre moment provides significant performance in analyzing small size images [62]. It is also robust to noise and blurry effect [264]	The study in 2011 [229] is only published work to evaluate of Legendre moments on medical X-Ray Images.	When order (m) of the moments increases this results in a decrease in accuracy. Furthermore, because of digitalization large variations need to be transformed, resulting in high computational cost.
Tchebichef	Based on a Radial Tchebichef polynomial expansion in which radial moments provide rotational invariance by considering only magnitude and ignoring phase component [149].	It is a discrete expansion, which constructs a set of scale and rotation invariant robust features.	Few pieces of research using Radial Tchebichef moment in medical image are addressed [92].	It is as a discrete orthogonal moment in the polar coordinate and there is no need to take digitalization process.
Krawtchouk	Based on discrete weighted Krawtchouk polynomials basis function to provide invariant features [256].	It brings recursive and symmetry properties to lessen the computational cost.	Several attempts have been made for medical image analysis applications [248].	Computational complexity is at an acceptable degree for large dataset [256].
Discrete Dual Hahn	The dual Hahn polynomials are a set of discrete orthogonal polynomials with more adjustable parameters ($\alpha\_1 \geq 0$, $\alpha\_2 > -1$) than Tchebichef and Krawtchouk moments to give more flexibility with minimal information redundancy.	It has properties such as recurrence relation, symmetry, scale and rotation invariant	No attention has been paid to medical imaging recognition.	
Fourier-Chebyshev	A mathematical combined term which is based on the discrete Fourier transform and a radial shifted Chebyshev polynomials (ψ_pq) [172]	This set brings appropriative properties such as symmetry property, recurrence relation, and it also takes a different sampling method that is more efficient in preserving details. [124].	In reviewing the literature, no data was found on the question of using Fourier-Chebyshev moment in medical image processing.	
Fourier-Mellin	It is based upon intensity values, circular Fourier transform and radial Mellin polynomials in a polar coordinate system [207, 212].	It is a scale and rotation-invariant orthogonal moment. This moment set has more zeros in the region of small radial distance, which leads to better performance in presence of small images.	In reviewing the literature, no data was found on the question of using Fourier-Mellin polynomials in medical imaging.	
Gegenbauer	It is based on Gegenbauer or ultra-spherical polynomials. It represents a large body of orthogonal polynomials with a scaling factor ($\alpha > -0.5$) adjustment, Γ refers to gamma function, P_n related to the Jacobi polynomials [89].	The most obvious finding to emerge from this ultra-spherical polynomials is that a global characteristic is determined with a small (α) whereas local image features with large value of (α) is extracted.	So far, there has been little discussion about Gegenbauer moment implementation in medical pattern recognition terms and further research should be done to investigate [8].	In our work a small (α) is carried out on dataset to preserve global white blood cell information.
Radial Harmonic Fourier	It is based on radial polynomial and discrete Fourier transform in a polar coordinate system, where radial function is defined by three conditional Equations [187].	They are invariant in terms of shifting, scaling, and rotation. This moment set has better ability to describe small images	Very little research has been found that used Radial-Harmonic-Fourier moments in medical imaging and in the recognition of cell smear images [186].	This is an appropriate option in presence of available low resolution dataset.

Relative shape measurements vector:

In addition, relative area (A_r), is also considered in white blood cells classification in our study. Shape feature vector includes invariant orthogonal moments and relative area for each white blood cell image.

As a result, and after relevant and redundant feature analysis (see Section 5.6) this suggests that moment implementation provides $332-36 = 296$ features corresponding to $11 - 1 = 10$ different invariant moment approaches (all approaches listed above excluding Legendre). In conclusion, the final shape feature vector consists of 297 feature coefficients for each white blood cell sample, composed of (296) invariant moment coefficients and (1) measure for A_r.

5.3.3 Texture Features

The following features aim to quantify the overall local density variability inside the object. It is often difficult to visualize textural features and associate feature values with the appearance of cells.

The vector includes features associated with the Laplace transform, gradient-based, flat texture features [193], and also co-occurrence matrix [82] which is defined over a white blood cell image to be the distribution of co-occurring values at a given offset. Various combinations of the matrix are taken to generate features called *Haralick* features [82] (namely, the angular second moment, contrast, correlation, sum of squares: variance, inverse difference moment, energy, and entropy). Afterwards, six parameters approximating visual perception is used based on the *Tamura* feature [222]. In addition, run-length is an another texture coarseness measurement at typical directions such as 0, 45, 90, and 135 degrees [223]. 11 features for a given gray-level for each individual white blood cell image are extracted. Dual-tree complex wavelet is also examined in this research. It calculates coefficients along rows and columns, and in *six* directions and angles at each individual pixel.

The setting, details and proposed framework using these textural features are addressed as follows. This section creates a high dimensional feature vector . These features include gradient transformation features ($\nabla f(x,y) = (\frac{\partial f(x,y)}{\partial x}, \frac{\partial f(x,y)}{\partial y})$), laplacian transformation features ($\nabla^2 f(x,y) = \frac{\partial^2 f(x,y)}{\partial x^2} + \frac{\partial^2 f(x,y)}{\partial y^2}$), flat texture features, and also co-occurrence matrix [82] which is defined over an white blood cell image to be the distribution of co-occurring values at a given offset. Let $n \times m$ be the size of the

input image I. Also, let $(\triangle x, \triangle y)$ be the parameters of an offset. Mathematically, a primary co-occurrence matrix definition is given by:

$$C_{\triangle x,\triangle y}(i,j) = \sum_{x=1}^{n}\sum_{y=1}^{m} \begin{cases} 1 & ;\ if \quad I(x,y) = i \ \&\ I(x+\triangle x, y+\triangle y) = j \\ 0 & otherwise \end{cases}.$$

Each entry is therefore considered to be the probability that a pixel with value i will be found adjacent to a pixel of value j. It estimates the probability that pixel $I(k,l)$ has intensity i and a pixel $I(m,n)$ has intensity j. Various combinations of the matrix are taken to generate features called *Haralick* features [82] (namely, the angular second moment, contrast, correlation, sum of squares: variance, inverse difference moment, energy, and entropy).

Afterwards, six parameters approximating visual perception is used based on the *Tamura* feature [222]. Tamura textural features include namely, coarseness (coarse versus fine), contrast (high versus low), directionality (directional versus non-directional), linelikeness (line-like versus blob-like), regularity (regular versus irregular), and roughness (rough vs. smooth). In addition, run-length [223] is an another texture coarseness measurement in specified directions. Run is a series of consecutive pixels which have the same intensity along with a specific direction. The dimension of run-length matrix is M by N, where M is the number of gray levels and N is the maximum run length at typical directions such as 0, 45, 90, and 135 degrees [223]. 11 features such as short run emphasis (SRE), long run emphasis (LRE), gray-level non-uniformity (GLN), run length non-uniformity (RLN), run percentage (RP), low gray-level run emphasis (LGRE), high gray-level run emphasis (HGRE), and some other ones are consequently extracted from run-length matrices $R(\imath, \jmath)$. For a given gray-level, individual white blood cell image, a run-length matrix $R(\imath, \jmath)$ quantifies the coarseness of a white blood cell texture at 0, 45, 90, and 135 degrees defined as the number of runs with pixels of gray level $\imath$ and run length $\jmath$. Further explanations and medical imaging application on run-length features are also addressed in various articles such as [103, 188, 232].

Initially, in this work gradient and laplacian transformation, flat texture with $r = 0$, *seven* Haralick features, *three* Tamura features i.e., coarseness, contrast, and directionality, *eleven* run length statistics and dual tree complex wavelet transform in *six* directions are considered.

Dual-Tree Complex Wavelet Transform (DT-CWT)

Wavelet transform analysis provides well-organized tools for capturing local image structure and details, with powerful analysis performance and multi-resolution properties, which is suitable for image analysis although it has several inherent drawbacks. The wavelet transform has *four* unsolved structural problems [203]: *Oscillations* (the coefficients tend to oscillate positive and negative around singular points, thus wavelet coefficient value tends to be exaggerated), *Shift variance* (a minor shift and rotation of the signal leads to significant variations in the distribution of energy between wavelet coefficients at different scales), *Aliasing* (since coefficients are quite extensive and are computed via down-sampling with non-ideal low-pass and high-pass filters which tends to alias the signals between one another and make them not to be identified as different or distinct), and *Lack of directionality* (lack of directional selectivity particularly makes difficult the analysis of geometric image features such as ridges and edges). To overcome these *four* weaknesses Dual-Tree Complex Wavelet Transform [105, 203] were introduced. The dual-tree wavelet was introduced as an extended and enhanced version of the typical discrete wavelet tree (DWT), with additive properties, shift invariance and directional selectivity in two and higher dimensions. DT-CWT is faster compared with the traditional template matching method [237] and also overcomes using wavelet thresholding [28] by having freedom degrees in variance and directional selectivity.

In practice, DT-CWT combines two digital wavelet transforms, using even and odd wavelets to provide complex coefficients. Each tree (α,β) contains purely real filters, whereby the two trees produce the real and imaginary parts respectively of each complex wavelet coefficients. For the tree (α,β) we need low pass filters with group delays which differ by half a sample period. The Q-shift (quarter shift) filter attains required group delays (see Fig. 30). This leads to low aliasing energy and also good shift invariance. The DT-CWT analysis is applied in $1-D$, along rows and columns, and *six* oriented $2-D$ complex wavelets are constructed from different combinations of the outputs.

The outcome of the DT-CWT is thus a set of complex coefficients as a sufficiently rich representation of local structure at each pixel for six different orientations (sub-bands) $\pm\frac{\pi}{12}, \pm\frac{\pi}{4}, \pm\frac{5\pi}{12}$, and for each of a number of scales by factor 2. For our segmented cell images, DT-CWT is applied at 6 scales, the number of levels of wavelet

decomposition and 14-tap Q-shift [105, 203] filters to white blood cell images, with 6 scales $(14*14, 7*7, 4*4, 2*2, 1*1, 1*1) \times 6$ sub-bands $(\pm\frac{\pi}{12}, \pm\frac{\pi}{4}, \pm\frac{5\pi}{12}) \times 2$ magnitude, phase components for each 28×28 sample (low magnified images). Regarding using the information in the feature vectors for SVM classification (see Section 7), the complex values (real and imaginary) are converted to polar form (magnitude, phase) to place alternating values into the feature vector (magnitude_1, phase_1, magnitude_2, phase_2 and so on) give the best results in classifier.

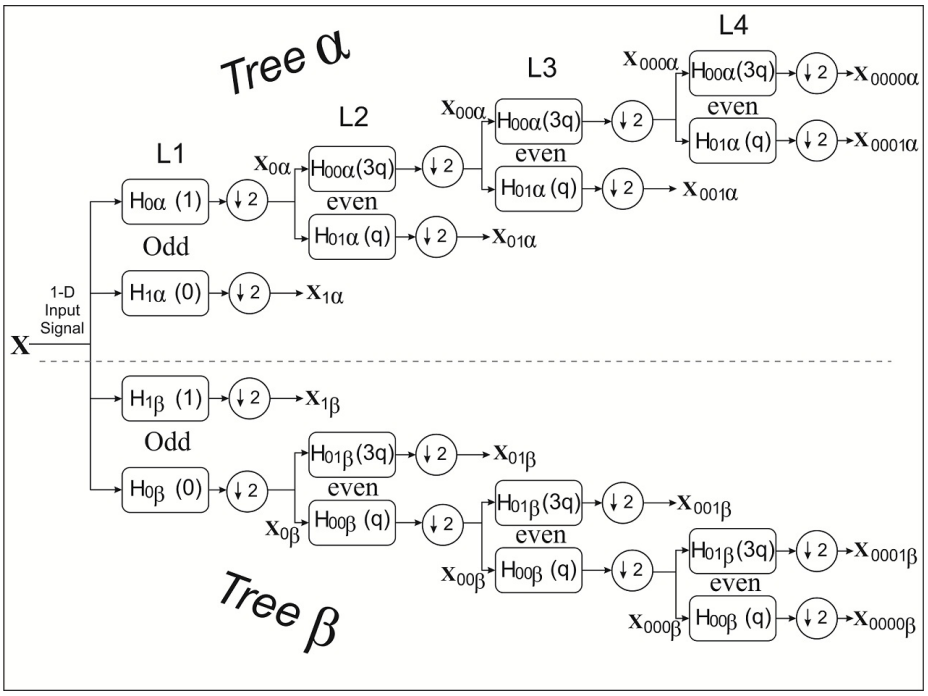

Figure 30: Q-shift DT-CWT [104], giving real and imaginary parts of complex coefficients from two trees(α,β). The approximate delay for each filter is shown by brackets in figures, where $q = 1/4$ sample period.

Taken together, these textural features indicates a total of 11019 feature coefficients for each white blood cell sample saved in 28×28. This textural feature vector may be divided into sevens aforementioned sub-groups and categories. The first part deals with Gradient, Laplacian and flat texture features with 784 items for each of them respectively. Then it will then go on to Haralick vector and also Tamura textural features with 13 and 6 elements respectively. Finally Gray-level run length matrix in four orientations (0, 45, 90, and 135) provides 6296 coefficients where DT-CWT gives a total of 2352 features for each 28×28 sample.

5.3.4 Feature Extraction Settings

This section examines feature extraction settings. As for feature extraction, this project examines three main different invariant feature sets (see Section 5.3). First, all segmented white blood cells are resized to 28×28 to simulate a low resolution image. Intensity features do not require parameters setting (see Section 5.3.1). However, with reference to shape and texture features, parametrization and their own settings are addressed as follow.

Shape Features

Hu set moments (see Section 5.3.2) are based on central moments of order up to 3. Hu set is calculated with different combination of order and repetition up to 3 (0, 1, 2, 3). It doesn't require any settings. In invariant orthogonal moment definition (see Section 5.3.2), low order captures general shape information and high order moment gradually maintains high frequency information representing detail of a given blood image. In this framework for all moments order and repetition are set to be $(5, 5)$. Next, most of these named invariant orthogonal moments do not require initial settings. However, required parameters are set as it can be seen at following table 15.

Table 15: Orthogonal Invariant Moments: Setting

	GP-Zernike, Krawtchouk, Dual Hahn, Gegenbauer		
Moment	**Parameter**	**Value**	**Comment**
GP-Zernike	α	1	A varying parameter that to adjust zero point to maintain details.
Krawtchouk	kp_1, kp_2	0.75	Varying parameters to extract local properties (Max = 1).
Dual Hahn	α_1, α_2	0.5	Varying parameters to extract local properties (Min= 0).
Gegenbauer	α	-0.5	A varying parameter to preserve global characters.

Texture Features

Textural features are covered in section 5.3.3. Most of these named invariant features do not require initial settings. Run-length, Flat texture and Dual Tree Complex Wavelet Transform (DT-CWT) require initial settings as follow.

Run-length [103,188,232] as a texture coarseness measurement is applied at typical directions such as 0, 45, 90, and 135 degrees. Next, flat texture [193] is applied with $r = 0$ where r is the arbitrary window size of the median filter. Finally, For our segmented cell images, DT-CWT [105, 203] is applied at 6 scales, the number of levels of wavelet decomposition and 14-tap Q-shift filters to image samples, and in 6 directions. It also should be noted that wavelet complex coefficients are converted into magnitude, phase components for each 28×28 sample (low magnified images) to set in a feature vector.

5.4 Advantages of Features

This section reviews briefly the usefulness of the aforementioned features in white blood cell classification. Each feature alone has certain important benefits for white blood cell detection. This study uses a combination of features, selected based on specific criteria, as depicted in table(see Table 21).

Intensity Histogram Features:

This measure describes globally the color change in a given white blood cell sample. However, for the purpose of white blood cell detection, such findings are not always sufficiently reliable to be extrapolated to all datasets. In addition, it was found that, with low quality, or degraded images, results were not very encouraging (see Tables 24, 23).

Hu set of Invariant Moments:

These coefficients are invariant to shape changes in rotation, scaling and translation. However, higher-order Hu set moments are sensitive to noise and they also include redundant information.

Orthogonal Invariant Moment:

They are invariant in rotation, scaling and translation and they provide minimal information redundancy. Some of these, like Dual Hahn, Fourier-Mellin, Radial Harmonic

Fourier and Fourier Chebyshev are adequate for extraction of local details with their own varying parameters (see Tables 14, 21).

Haralick Features:

It is based on a probability that a given pixel a has value of i while simultaneously an adjacent pixel b has value of j. Thirteen features were extracted by Haralick from the Gray-Level Co-Occurrence Matrix (GLCM). This provides a general view of the distribution of co-occurring values in a given white blood cell. It represents a statistical approach, which characterizes the amount of spread with regard to intensity values in adjacent pixels. The colour feature alone is not enough to interpret a small white blood cell image. However, the combination described provides a global attribute with local information.

Dual Tree Complex Wavelet Transform:

It provides a local, invariant rich characterization, by using a dual tree of wavelet filters along the rows and columns, and in six directions and angles at each individual pixel. It brings non-redundant information, and it also overcomes the four major weaknesses typical of Wavelet Transform.

Gray Level Run Length:

It is a coarseness measurement. Run detects a series of consecutive pixels which have the same intensity along the typical directions such as 0, 45, 90, and 135 degrees. Intensity histogram lacks detailed information. However, Run is a measure that can be used to distinguish images with different local appearances, even though they have similar histograms. It can efficiently describe the colors, directions and geometrical shapes of the white blood cells in an image. Eleven features were extracted by Run calculation.

Tamura Features:

It is a series of features that correspond to human visual perception. This is the great advantage of the Tamura features. Six features were extracted by Tamura concept. It

should be noted that the first three features: coarseness, contrast, and directionality, which depict a white blood cell sample in accordance with visual perception, are particularly important.

Gradient Feature:

It is a measure to describe the directional change of gray intensity values in a given white blood cell image. Gradient feature is robust to lighting and camera changes. It is a characteristic appropriate for WBC detection, of which this work takes advantage.

Laplacian Feature:

The Laplace transformation is a means to establish borders and boundaries of white blood cells, via zero sum of the second partial derivatives. Essentially, this feature examines the velocity of gradient changes in a given white blood cell, since a white blood cell lacks strong edges and boundaries. Thus, a link between these features and white blood cell detection is weak.

Flat Texture:

It represents the smoothing difference between the original white blood cell and a median filtered image. The average value of a flat texture image describes the unbalance in light and dark pixel distributions. The degree of smoothness is calculated by varying the arbitrary parameter (r) as a multiple of the median calculated.

5.5 Comparison of the Proposed Approach to State-of-the-Art

This section focuses on comparative studies on state-of-the-art feature extraction and white blood cell detection. Authors in [160] used a feature set composed of shape and color texture based features. The feature set are area of cell and nucleus, ratio of nucleus area and perimeter length over cell, compactness and boundary, energy of nucleus, and also from second and third-order central moments. As mentioned before, varying capturing angles and different magnification cause non reliable variant cell

appearance in correspondence with area, perimeters and roundness or other similar measures like these. Also, second and third-order central moments as Hu set moments are also so sensitive to noise and it is with redundant information. Thus their performance depends on their own dataset and the generalizability of this published research is problematic.

Authors in [34] used chromatic feature sets that are very questionable in different conditions (see Table 24). Authors in [213] examined shape features such as eccentricity of the nucleus and cytoplasm contours, compactness of the nucleus, area-ratio and the number of nucleus lobes. This article also used texture features such as gray-level co-occurrence matrix(GLCM) and auto-correlation matrix to detect cells. The key problem with this explanation is that separation nucleus and cytoplasm in low resolution images is not easy as well as cytoplasm contours and number of nucleus lobes is very problematic in different possible adverse conditions. However, gray-level co-occurrence matrix(GLCM) provides several invariant statistics about the texture of a white blood cell image that it brings appropriate characteristics even in low resolution images (see Section. 5.3.3).

Authors in [183] used a 18 color, 8 shape dimensional feature vector and support vector machine (SVM). With reference to color characteristic, authors used mean, standard deviation, and skewness calculation separately for hue, saturation, and luminance. Furthermore, authors examined contour-based descriptors such as convexity, perimeter, principal axis ratio, compactness, circular and elliptic variance. All these contour-based descriptors reviewed so far cannot represent ideally white blood cell shapes for which the complete and continuous boundary information is not ideally available with granular and non-uniform borders. However, mean, standard deviation, and skewness gives appropriate characteristic even in low quality image.

Authors in [228] used four white blood cell nucleus features. These features are first and second Granulometric moments [200], area of the nucleus and the location of its pattern spectrum's peak. It is found that all these four shape features applied on segmented nucleus where this segmentation is not very easy in all possible low quality images. In addition, to obtain granulometric moments different structure elements should be used to analyze morphological characteristics of white blood cell nucleus where these settings are not reliable in presence of irregular messy nucleus shapes. Furthermore, granulometric operation is sensitive to noise and false calculation will

be addressed in moment results.

Authors in [106] used 12 ensemble features such as shape, intensity, and texture features with 71 dimensions. These features as shape descriptors are; area, perimeter, eccentricity, first and second invariant moment, the number of nuclei. For the intensity feature; average and standard deviation of each nucleus and lastly, for the texture feature, 59 LBPs (local binary patterns) are used. This argument relies too heavily on qualitative analysis of blood slides and the existing accounts fail to resolve cell discrimination with different quality.

Authors in [189] used feature vector which was made of nucleus and cytoplasm area, nucleus perimeter, number of separated parts of nucleus, mean, variance of nucleus and cytoplasm boundaries, co-occurrence matrix and also local binary patterns (LBP) measures. In a broadly speaking, questions have been raised about the nucleus and cytoplasm area, nucleus perimeter, number of separated parts of nucleus and cytoplasm boundaries. However, co-occurrence matrix and also local binary patterns (LBP) measures are appropriate candidates in different dataset.

Authors in [38] proposed a white blood cell classification with 19 features evaluated for the nucleus and cytoplasm. These features are such as area, perimeter, convex area, solidity, orientation, eccentricity, circularity, ratio of nucleus area to area of white blood cell, entropy of the cytoplasm, and mean gray-level intensity of the cytoplasm. Almost the same feature extraction strategy is addressed in other work [51] with reference to geometrical shape features such as area, solidity, eccentricity, the area of convex part of the nucleus and perimeter. As a result, in a low quality image using these named shape features is questionable and the generalizability of only these features on this issue is problematic.

Overall, the difficulties in detection and classification are further aggravated by the fact that there is no definitive procedure exactly prescribing what features should be generated, or what features should be used in each specific case. Previous work as mentioned in detail used features that they are not always invariant and can be changed in different conditions and resolutions. Shape features such as area, perimeter and so on rely heavily on their own data set and of course these findings cannot be extrapolated to all possible dataset. Previous researches did not investigate benefits of local data preserving techniques such as dual-tree complex wavelet transform, Run length and invariant orthogonal moments such as Fourier-Mellin, Radial Harmonic

Fourier, Dual Hahn.

In reality, this work suggests some proper invariant features that maintain local information even in presence of low quality images where internal details are not easy to distinguish. These features can be named as orthogonal invariant moments (i.e, Radial Harmonic Fourier, Dual Hahn, Fourier- Mellin), DT-CWT (Dual-Tree Complex Wavelet Transform), run length and Tamura features. Experimental results prove that these named invariant features bring benefits in presence of low quality imaged.

5.6 Relevant and Redundant Features

In this section we obtain a set of relevant and least redundant features among all candidates. Intensity (see Section. 5.3.1) and texture features (see Section. 5.3.3) are not correlated and thus they have negligible redundancy and large relevance. However, shape features are based on invariant moment descriptors (see sub-section 5.3.2) in which similar characteristics can be found to some extent (see Table 14). The evaluation procedure for shape features has been organised as follows. The first part deals with distribution functions. In both Kolmogorov - Smirnov and Wilcoxon-Mann-Whitney tests, all scaled feature data with primary matrix (140 rows = 28 samples per each five class) are used to evaluate distribution behaviour. In the next step, Pearson and Spearman measure objectively linear correlation or/and monotonic function behaviour while Kendall addresses the rankings of the correlation coefficients for input data.

5.6.1 Kolmogorov - Smirnov (K-S)

Kolmogorov - Smirnov method provides a non-parametric measure test to determine whether an empirical density function over available dataset can be mapped to a particular known distribution model to describe the statistical properties of feature vector [170]. It calculates the vertical distance (KS_D) between the cumulative distribution function (CDF) of the reference hypothetical distribution and the empirical distribution function EDF. Two sided (K-S) test is used to compare two sample sets (two invariant moments in this case) without any particular distribution assumptions. The (KS_D) is defined by following equation:

$$KS_D = sup_n \, |CDF(x) - EDF(x)_n|$$

The null hypothesis, meaning that two distributions are similar is accepted when KS_D is less than the 5% significance level.

Dataset and K-S interpreting: For all samples, the aforementioned shape feature vector (see sub-section 5.3.2), the two-sided K-S test is used to calculate the significance value of vertical distances (KS_D) for all available pairs of feature moment candidates. The values obtained by applying the null hypothesis tell us whether two mutually independent feature sets are sufficiently close to each other to belong to the same distribution. The experimental results are summarized in table 16.

The table 16 presents p-values obtained from the preliminary analysis of two sided Kolmogorov-Smirnov test to evaluate distribution similarity among 11 invariant moments. It can be seen from the data in table that all these moments are drawn from the same distribution (null hypothesis is accepted). This tendency is also reflected in the p-value. From this data, we can see that the lowest discriminatory power is 0.42491, which occurs between Legendre and Gegenbauer moments. In contrast, there is a clear trend of increasing p-values, 0.9762 between Krawtchouk and Legendre moments and, 0.9906 between Radial Tchebichef and Zernike moments.

To make a firm determination, Mann-Whitney test is also used here (see. 5.6.2). Both the Mann-Whitney and the Kolmogorov-Smirnov tests are non-parametric tests to compare two groups of invariant moment data, and both methods calculate p-values over the same null hypothesis but using different approach.

K-S test computes p-values after cumulative distribution comparison of the two data moment sets and WMW test then computes p-values that depend on the discrepancy between the mean ranks of the two moments after ranking all the moment coefficient values from low to high. The K-S test is more sensitive to differences between any two feature moments, which are reflected in small p-values. In contrast, the WMW test is mainly sensitive to changes in median value. The WMW test has inherent and structural ability to handle tied values, whereas K-S test does not work very well with ties. In presence of moment categories, many ties are possible. For this reason, it is highly recommended to perform the WMW test,in addition to K-S test.

Table 16: P-values for Kolmogorov-Smirnov test, totals over 11 moment series (see Section 5.3.2), different feature sets.

	M1	M2	M3	M4	M5	M6
M1	0	0.84382	0.84382	0.84382	0.84382	0.84382
M2	0.84382	0	0.84382	0.84382	0.84382	0.84382
M3	0.84382	0.84382	0	0.84382	0.84382	0.84382
M4	0.84382	0.84382	0.84382	0	0.84382	0.84382
M5	0.84382	0.84382	0.84382	0.84382	0	0.84382
M6	0.84382	0.84382	0.84382	0.84382	0.84382	0
M7	0.84382	0.84382	0.84382	0.84382	0.84382	0.84382
M8	0.84382	0.84382	0.84382	0.84382	0.84382	0.84382
M9	0.84382	0.84382	0.84382	0.84382	0.84382	0.84382
M10	0.990623	0.42491	0.42491	0.42491	0.42491	0.42491
M11	1	0.42491	0.42491	0.42491	0.42491	0.42491
M12	1	0.990623	0.42491	0.42491	0.42491	0.42491

	M7	M8	M9	M10	M11	M12
M1	0.84382	0.84382	0.84382	0.990623	1	1
M2	0.84382	0.84382	0.84382	0.42491	0.42491	0.990623
M3	0.84382	0.84382	0.84382	0.42491	0.42491	0.42491
M4	0.84382	0.84382	0.84382	0.42491	0.42491	0.42491
M5	0.84382	0.84382	0.84382	0.42491	0.42491	0.42491
M6	0.84382	0.84382	0.84382	0.42491	0.42491	0.42491
M7	0	0.84382	0.84382	0.42491	0.42491	0.42491
M8	0.84382	0	0.84382	0.42491	0.42491	0.42491
M9	0.84382	0.84382	0	0.42491	0.42491	0.42491
M10	0.42491	0.42491	0.42491	0	0.97621	0.97621
M11	0.42491	0.42491	0.42491	0.97621	0	0.97621
M12	0.42491	0.42491	0.42491	0.97621	0.97621	0

5.6.2 Wilcoxon- Mann-Whitney (WMW) Test

Wilcoxon- Mann-Whitney - U test at the standard $\alpha = 0.05$ significance level is applied to see whether the two distribution functions with no prior normal assumption are shifted in some way from one another. Wilcoxon Mann-Whitney test is a non-parametric measure often used in place of the two sample parametric t-test when the normality assumption is questionable [165]. It assesses the similarity of two unpaired independent sample groups, which is also called U statistics. In this statistical hypothesis test, null hypothesis H_0 is that the two samples are from identical populations and an alternative hypothesis H_1 is that two distributions differ in the median value. The degree of similarity of both feature sequences is denoted using a probability term. A higher value means greater similarity between two sample distributions, whereas small value of p shows large variation and divergence between two populations.

Dataset and M-W interpreting: For all samples, aforementioned feature vector (see sub-section 5.3), a two-sided M-W test is used to calculate the significance value for vertical distance between any pair of feature candidates. The values obtained by applying the null hypothesis show whether two mutually independent feature follow the same distribution function. It should be noted that this technique has an advantage over K-S technique, when tied values are found. The experimental results in this work are summarized in Table 17.

Table 17: P-values for Mann-Whitney test, totals over 11 moment series (see. 5.3.2), different feature sets.

	M1	M2	M3	M4	M5	M6	M7	M8	M9	M10	M11	M12
M1	0	1	1	1	1	1	1	1	1	1	1	1
M2	1	0	1	1	1	1	1	1	1	0.6	0.6	1
M3	1	1	0	1	1	1	1	1	1	0.6	0.6	0.6
M4	1	1	1	0	1	1	1	1	1	0.6	0.6	0.6
M5	1	1	1	1	0	1	1	1	1	0.6	0.6	0.6
M6	1	1	1	1	1	0	1	1	1	0.6	0.6	0.6
M7	1	1	1	1	1	1	0	1	1	0.6	0.6	0.6
M8	1	1	1	1	1	1	1	0	1	0.6	0.6	0.6
M9	1	1	1	1	1	1	1	1	0	0.6	0.6	0.6
M10	1	0.6	0.6	0.6	0.6	0.6	0.6	0.6	0.6	0	1	0.8
M11	1	0.6	0.6	0.6	0.6	0.6	0.6	0.6	0.6	1	0	1
M12	1	1	0.6	0.6	0.6	0.6	0.6	0.6	0.6	0.8	1	0

As shown in Mann-Whitney test table . 17 there is a significant distribution similarity between the aforementioned moment groups. The calculation indicates that lowest discriminatory power is 0.6 which occurs among Legendre, Krawtchouk and Radial Tchebichef, whereas p-values are high (0.8 and 1.00) for most other moment pairs.

So far, it has conclusively been shown that named invariant moment features are from similar distribution, and it has been demonstrated that a high similarity among probability distributions exists. A question then arises whether these 11 invariant moments are redundant, related or totally independent. To address this question, methods such as Kruskal-Wallis H-Test, Pearson correlation analysis (PCA) and Spearman Correlation Analysis (SCA) are available to analyse the correlation relationships between feature variables, and they have been applied as follows.

5.6.3 Kruskal-Wallis H-Test

The one-way analysis of variance (abbreviated one-way ANOVA) is a statistical measure to examine whether three or more independent input variables are significantly different. Kruskal-Wallis H- test evaluates the behaviour of these unrelated groups using variance parameter. In typical one-way ANOVA the assumptions are based on approximately normally distributed variables and an equal interval scale randomly drawn from the population, and inputs are normal random variables.

If one or more of the mentioned assumptions are violated, then the one-way ANOVA may be inaccurate. To overcome this limitation Kruskal Wallis [165, 245] performs one-way analysis of variance (abbreviated one-way ANOVA) without normal distribution assumption, by ranking 11 independent moment groups of possibly unequal sizes (see Section 5.3.2). However, one of the limitations of Kruskal Wallis ($\mathbb{k}$) explanation is that it does not address where the dissimilarities take place or how many differences really occur in a completely randomized design.

The returned p value ($= 0.0669$) from the preliminary analysis of Kruskal Wallis test indicates a *slight* correlation between 11 different moments. However, a clear degree of similarities or differences between groups of moments could not be identified by this analysis. Further studies, which take the degree of correlation into account need to be undertaken.

5.6.4 Sensitivity Correlation Analysis

Pearson's correlation: The degree of scatter among feature variables can be evaluated using Pearson's correlation measure. It is a measure to evaluate the linear correlation (dependence) between two input feature variables. Pearson statistical approach computes moment correlation coefficient between two variables x_1 and x_2. It considers the strength of a linear relationship between paired input moment feature data. It is defined as the covariance of the two variables divided by the product of their standard deviations, which gives values between $+1$ and -1, where $+1$ means totally correlated inputs, 0 means no correlation, and -1 means negative correlation between two inputs.

The experimental result is summarized in table. 18. As shown in table 18, there is a significant linear similarity between some of the mentioned moment groups. The calculation indicates that the highest correlation is between the Radial Tchebichef and Legendre, and between Gegenbauer and Legendre moments with correlation rates of 0.99 and 0.95 respectively. In contrast, the lowest correlations values are between Gegenbauer and Radial Harmonic Fourier, and between Fourier-Chebyshev and dual Hahn moments (0.17 and 0.19 respectively).

Spearman's correlation: is a non-parametric version of correlation that estimates variables dependency. It calculates the power of association between two ranked input feature variables. It is a statistical measure that evaluates how two variables can be fitted using a monotonic function. A monotonic relationship is an essential primitive hypothesis of referring the Spearman index correlation. A linear relationship is a firm underlying assumption that has to be met by Pearson correlation measure. The value of Spearman's index ranges between $+1$ for a perfect monotonic function to -1 which is furtherest from a mapped monotonic function.

As shown in Spearman test table. 19 there is a significant monotonic relationships among few of the aforementioned moment groups. The calculation indicates that highest dependency exists between Legendre and Gegenbauer moments, Radial Tchebichef and Legendre moments, and Krawtchouk and Dual Hahn moments with correlation rates of 0.9819, 0.9027 and 0.8355 respectively. In contrast, lowest correlations are between Dual Hahn and Gegenbauer, Dual Hahn and Legendre, and Dual Hahn and Generalized Pseudo-Zernike moments with minimum correlations values of $-0.1335, -0.1104$ and 0.0005 respectively.

Table 18: Correlation degree for Pearson test, totals over 11 moment series (see. 5.3.2), different feature sets.

	M1	M2	M3	M4	M5	M6
M1	1	0	0	0	0	0
M2	0	1	0.667934	0.94987	0.712445	0.730867
M3	0	0.667934	1	0.610314	0.732017	0.947971
M4	0	0.94987	0.610314	1	0.635324	0.650374
M5	0	0.712445	0.732017	0.635324	1	0.776434
M6	0	0.730867	0.947971	0.650374	0.776434	1
M7	0	0.623717	0.860916	0.632057	0.641255	0.849871
M8	0	0.330158	0.195434	0.1735	0.308071	0.256721
M9	0	0	0	0	0	0
M10	0	0.594213	0.309203	0.433271	0.488665	0.393357
M11	0	0.999855	0.667135	0.954899	0.709775	0.728852
M12	0	0	0	0	0	0

	M7	M8	M9	M10	M11	M12
M1	0	0	0	0	0	0
M2	0.623717	0.330158	0	0.594213	0.999855	0
M3	0.860916	0.195434	0	0.309203	0.667135	0
M4	0.632057	0.1735	0	0.433271	0.954899	0
M5	0.641255	0.308071	0	0.488665	0.709775	0
M6	0.849871	0.256721	0	0.393357	0.728852	0
M7	1	0.208364	0	0.255141	0.625463	0
M8	0.208364	1	0	0.893279	0.32264	0
M9	0	0	1	0	0	0
M10	0.255141	0.893279	0	1	0.587171	0
M11	0.625463	0.32264	0	0.587171	1	0
M12	0	0	0	0	0	1

Table 19: Correlation degree for Spearman test, totals over 11 moment series(see. 5.3.2), different feature sets.

	M1	M2	M3	M4	M5	M6
M1	1	0	0	0	0	0
M2	0	1	0.306306	0.835521	0.350064	0.246075
M3	0	0.306306	1	0.145689	0.604633	0.743372
M4	0	0.835521	0.145689	1	0.171686	0.074131
M5	0	0.350064	0.604633	0.171686	1	0.702188
M6	0	0.246075	0.743372	0.074131	0.702188	1
M7	0	0.149103	0.431543	0.132001	0.651457	0.404288
M8	0	0.0713	0.088031	-0.13359	0.061776	0.003089
M9	0	0	0	0	0	0
M10	0	0.283319	0.169208	0.071026	0.201326	0.091393
M11	0	0.902703	0.166795	0.981982	0.210811	0.100129
M12	0	0	0	0	0	0

	M7	M8	M9	M10	M11	M12
M1	0	0	0	0	0	0
M2	0.149103	0.0713	0	0.283319	0.902703	0
M3	0.431543	0.088031	0	0.169208	0.166795	0
M4	0.132001	-0.13359	0	0.071026	0.981982	0
M5	0.651457	0.061776	0	0.201326	0.210811	0
M6	0.404288	0.003089	0	0.091393	0.100129	0
M7	1	0.000534	0	0.074817	0.139483	0
M8	0.000534	1	0	0.837423	-0.11042	0
M9	0	0	1	0	0	
M10	0.074817	0.837423	0	1	0.1115	0
M11	0.139483	-0.11042	0	0.1115	1	0
M12	0	0	0	0	0	1

After investigation using the three named methods (Kruskal-Wallis H-Test, Spearman and Pearson) a very slight evidence of correlation among all the aforesaid invariant moments is found when Kruskal Wallis test is applied. Then, it can be seen from the data in tables. 18 and 19 that there are significant correlations between Legendre and Gegenbauer and between Legendre and Radial Tchebichef. In contrast, a decreasing monotonic trend and very low correlations between Dual Hahn and generalized pseudo-Zernike moments are found.

As a result, the experimental results do not show any significant increase in redundancy among the aforementioned moments. In this evaluation process, Legendre was found to provide information redundant to Gegenbauer and Radial Tchebichef to some extent. This suggests that Legendre may be removed from the moment list, since, according to table 14, both Gegenbauer and Radial Tchebichef moments are superior to Legendre moment in connection with feature extraction.

Thus, the findings would have been more original and convincing if the orthogonal Legendre moments had been excluded from the above moment list of the feature vector (see Section 5.3.2).

5.7 Feature Extraction Contributions

Another contribution is the procedure developed for obtaining optimum invariant feature set from a comprehensive literature review in mathematical concepts. The current findings add substantially to our understanding of invariant global features in preserving details even in presence of low degraded images. For this, an image, segmented white blood cell, is characterized based on the information such of dual tree complex wavelet transform, invariant orthogonal moments, Run length, and so on. This is an approach to address global invariant characteristics and the results are encouraging.

Feature Extraction

Overall, the difficulties in detection and classification are further aggravated by the fact that there is no definitive procedure exactly prescribing what features should be generated, or what features should be used in each specific case. Previous work as mentioned in detail used features that they are not always invariant and can be

changed in different conditions and resolutions. Shape features such as area, perimeter and so on rely heavily on their own data set and of course these findings cannot be extrapolated to all possible dataset. Previous researches did not investigate benefits of local data preserving techniques such as dual-tree complex wavelet transform, Run length and invariant orthogonal moments such as Fourier-Mellin, Radial Harmonic Fourier, Dual Hahn. Comparative study and discussion is also found in section 5.5.

Chapter 6

Feature Selection

The purpose of feature selection is to provide a smaller effective feature vector compared to the starting data pool. The main objective is to find a way to identify the features that are worth extracting for optimal accuracy and speed of operation. Feature selection is to trim a large number of input variables from a given data-set, based on similarities and discrepancies. Then eventually, the low sensitivity and low correlation between feature and desired classes means weak interaction between feature and desired output and can be neglected. Feature discriminatory power is a criteria for feature selection.

6.1 High Dimensional Model Representation

We look at the effect and contribution of multiple features (see Section. 5.3) on the supervised white blood cell classification. Several studies investigating high-dimensional model representation (HDMR) have been carried out on input and output relationship analysis. In general, in the field of image processing and feature selection, HDMR has not yet been investigated comprehensively. To overcome this gap, this work focuses on the use of HDMR for image processing pattern recognition applications.

In reviewing the literature, several methods with various expansions of high dimensional model representations are found, such as factorized high dimensional model representation (FHDMR) [4, 234], Cut-HDMR [4, 147], (ANOVA)-HDMR [4] as the analysis of variance (ANOVA) decomposition, random sample(RS)-HDMR [4, 267], multiple sub-domain random sampling HDMR [260], logarithmic HDMR [233] and

hybrid function [235].

HDMR is an appropriate statistical approach to evaluate the input - output mapping of a manifold model with many input parameters and using high dimensional interpolation [4]. High dimensional model representation (HDMR)can therefore evaluate the individual or cooperative contributions of the previously defined features used for classification of white blood cell. Next, the degree of importance and interaction of input feature parameters (12104) with regard to white blood cell classes are determined using sobol global sensitivity analysis.

Before a detailed description of the sensitivity analysis, we will provide a few definitions related to HDMR. The HDMR output function $f(x)$ utilizes a linear sum of super - positions of low - dimensional functions, where a multivariate data is given for a multivariate function $f(x) = f(x_1, ..., x_n)$ in R^n domain. These sub-divided terms are set of constant, univariate, bivariate and the other high-variate terms.

$$f(x) = f_0 + \sum_{i=1}^{n} f_i(x_i) + \sum_{1 \le i < j \le n} f_{ij}(x_i, x_j) + \sum_{1 \le i < j < k \le n}^{n} f_{ijk}(x_i, x_j, x_k) + \cdots + f_{12\ldots n}(x_1, x_2, \ldots, x_n)$$

where f_0 is the constant mean effect, $f_i(x_i)$ is the effect of variable x_i (each individual feature coefficient) independently upon the output $f(x)$ (five primary cell classes). Further, the function $f_{ij}(x_i, x_j)$ is a second order term describing the interaction between two feature series (x_i and x_j) upon the output $f(x)$. It is apparent that if there is no interaction between the input feature variables, then higher order terms will be zero, where only f_0 order and $f_i(x_i)$ will be written in the HDMR expansion.

From the experimental results for many input-output systems, it can be seen that a HDMR expansion up to second order $f_{ij}(x_i, x_j)$ is sufficient to approximate $f(x)$ in which higher order feature correlations are weak and negligible [126]. In this work, RS-HDMR approach with a random sample input over the entire domain is used [4, 267]. The sums of RS-HDMR expansion can be rewritten in the following form where determination of expansion components is based on shifted Legendre polynomials approximation and Monte Carlo integration [126]. Input variables are scaled between 0 and 1 ($0 \le x_{input} \le 1$) [178,267] to create scale - consistent coefficient

values.

$$f(x) = f_0 + \sum_{i=1}^{n}\sum_{r=1}^{k_1}\alpha_r^i\varphi_r(x_i) + \sum_{1\le i<j\le n}^{n}\sum_{p=1}^{k_2}\sum_{q=1}^{k_3}\beta_{pq}^{ij}\varphi_{pq}(x_i,x_j).$$

Where k_1, k_2 and k_3 are the order of the shifted Legendre polynomials expansion. α_r^i and β_{pq}^{ij} are constant coefficients which are determined using Monte Carlo integration. Also, $\varphi_r(x_i)$, $\varphi_{pq}(x_i,x_j)$ are the shifted Legendre polynomials basis functions. To understand expansion calculation, let's first define second-order Legendre's differential equation:

$$\left(1-x^2\right)\frac{d^2y}{dx^2} - 2x\frac{dy}{dx} + n\left(n+1\right)y = 0$$

The solution, Legendre polynomial is denoted by $P_n(x)$ which includes order n as an integer, which provides either odd or even components that are either symmetric or asymmetric polynomials ($P_n(-x) = (-1)^n P_n(x)$). To calculate shifted Legendre polynomials where $x \mapsto 2x-1$; $(\tilde{P}_n(x) = P_n(2x-1))$, calculations are given by recurrence relation, based on Bonnet's recursion formula. Therefore, an explicit representation is obtained:

$$\tilde{P}_n(x) = (-1)^n \sum_{c=0}^{n}\binom{n}{c}\binom{n+c}{c} \times (-x)^c.$$

Consequently, shifted Legendre polynomial are given in table 20.

Table 20: The first five shifted Legendre polynomial terms

n	$\tilde{P}_n(x)$
0	$\tilde{P}_0(x) = 1$
1	$\tilde{P}_1(x) = 2x-1$
2	$\tilde{P}_2(x) = 6x^2-6x+1$
3	$\tilde{P}_3(x) = 20x^3-30x^2+12x-1$
4	$\tilde{P}_4(x) = 70x^4-140x^3+90x^2-20x$
5	$\tilde{P}_5(x) = 252x^5-630x^4+560x^3-210x^2+30x-1$

Legendre polynomials have the property of orthogonality, i.e. their components are non-overlapping and non-redundant, and therefore their principal sums can be obtained.

$$\int_0^1 \widetilde{p_k(x)}\widetilde{p_l(x)}dx = \begin{cases} \frac{1}{2n+1} & k=l \\ 0 & k\neq l \end{cases}$$

The theory of Legendre polynomials is found in book [110] section 5.2. The optimal order of shifted Legendre polynomials is used for approximation of the HDMR expansion component functions.

Global Feature Sensitivity: The aim of this section is to measure the level of influence (global sensitivity) of the input feature variable on the white blood cell classification using RS-HDMR implementation to identify the best feature set. Following that, the influence of individual each input feature variable is computed using global sensitivity approach, in which Monte Carlo is the basis function of calculation [214]. An integrable function is defined for an arbitrary monotonic function $f(x)$ that preserves the given order. It is denoted that for every sequence D_n of subsets on $[a, b]$, we have shown that $\{\mu(D_n)\} \to 0$. S_n is a sample of mentioned partition, which can be expressed as follows.

$$\left\{\sum(f, D_n, S_n)\right\} \to K.$$

An integrable function could be written in the ANOVA - representation form [214] where total number of sums is 2^n. The general definition is

$$f(x) = f_0 + \sum_{s=1}^{n} \sum_{i_1<\ldots<i_s}^{n} f_{i_1\ldots i_s(x_{i_1},\ldots,x_{i_s})}$$

where that the terms are orthogonal and can be expressed as

$$\int_0^1 f_{i_1\ldots i_s}(x_{i_1}, ..., x_{i_s})dx_k = 0, \qquad k = i_1, ..., i_s.$$

Above terms can be rewritten in following form :

$$\int f(x)dx = f_0$$

$$\int f(x) \prod_{k\neq i} dx_k = f_0 + f_{i_{xi}}$$

$$\int f(x) \prod_{k\neq i,j} dx_k = f_0 + f_{i_{x_i}} + f_{j_{x_j}} + f_{ij_{x_i,x_j}}.$$

Global sensitivity is defined by the following equations:

$$\int f(x)^2 dx - f_0^2 = \sum_{s=1}^{n} \sum_{i_1<\ldots<i_s}^{n} \int f^2_{i_1\ldots i_s(x_{i_1},\ldots,x_{i_s})dx_{i_1},\ldots dx_{i_s}}.$$

To simply notation, indices D and $D_{i_1}, ..., D_{i_s}$ are defined as follows :

$$\underbrace{\int f(x)^2 d_x - f_0^2}_{D} = \sum_{s=1}^{n} \sum_{i_1<...<i_s}^{n} \underbrace{\int f_{i_1...i_s}^2(x_{i_1},...,x_{i_s})dx_{i_1},...dx_{i_s}}_{D_{i_1},...,D_{i_s}}$$

Therefore, global sensitivity indices are denoted by: $S_{i_1,...,i_s} = \frac{D_{i_1},...,D_{i_s}}{D}$ where total of the summation $\sum_{s=1}^{n} s_{i_1} + \sum_{1<i<j\leqslant n}^{n} S_{ij}, ... + S_{1,2,...,n} = 1$. The first order index S_i is the fractional contribution of x_i (each individual coefficient) to the variance of $f(x)$ (five main white blood cell classes), whereas the second order shows the effect of interaction between x_i and x_j on the classification outcome. These sensitivity analysis indices can be continued. Rabitz *et al.* [4] demonstrated that, often, the low order interactions of input variables have the dominant impact on the output assignment. It means that, quite often, the high ranked global sensitivity feature variable input in mathematical models are first order terms. In the current study, first order S_i for all each individual intensity, shape and texture coefficients are calculated to reach the most effective feature set.

To date, little evidence has been found associating HDMR with image processing and pattern recognition. Kaya *et al.* [101] carried out a number of investigations into the feature selection by high dimensional model representation, where the experiment is conducted using a data set which includes 12 band multi spectral images taken over Tippecanoe County. Article references were searched further for additional relevant publications, and no other work pertaining to the question of HDMR efficiency in feature selection for medical images and blood smear slides in particular was found. A further study with more focus on selecting optimum feature set is suggested in this work.

6.2 Sequential Feature Selection

Sequential feature selection applies an iterative method and an algorithm that learns which feature from an initial set, without a transformation, is the most informative at each step, when choosing the next feature depends on the already selected features. The method removes unfavourable features but it preserves salient features to reach the optimum subset combination of features by considering their predictive efficiency for a given classifier. The method has two distinctive variants. Sequential forward

selection (SFS) is a method that keeps adding features, until the criterion function stops decreasing with new feature candidates. In contrast the process of sequential backward selection (SBS) starts with a full feature set, and features are removed until the removal action starts to increase the criterion function [93].

In SFS, new added feature x^+ should maximize $J(Y_k + x^+)$. In an iterative and incremental procedure, new component is combined with already selected features (Y_k) to increase criterion function $(x^+ = \arg_{x \notin Y_k} max\ J(Y_k + x^+))$. Both SFS and SBS have some drawbacks in practice. Questions have been raised about the update procedure used in sequential feature selection algorithm. SFS is unable to revise an already selected a feature vector by removing feature variables after they have been added. The main limitation of SBS is its inability to improve the efficiency by restoring a feature variable after it has been abandoned in a previous step. It can also be seen that without an appropriate criterion to determine a stop point, the SFS or BSS may run an exhaustive number of combinations $\binom{F}{N}$ considering (N) input samples, which make the process impractical and infeasible because of its complexity. To improve feature selection sustainability, it is necessary to develop a criterion to avoid exhaustive comparison. An optimum criterion value means a minimum error rate in supervised classification where each candidate feature is placed in the new revised subset vector upon classifier feedback.

Next, 10-fold cross-validation by calling a criterion with different training and testing subsets of x_{in} and y_{out} is performed. In practice, after computing the mean criterion values for each candidate feature subset, SFS chooses the optimal feature candidate that minimizes the mean criterion value. It measures the reduction in distance between the predicted values and the output testing subset. This process continues until adding or removing features results in no decrease in criterion.

To date, several studies investigating sequential forward selection (SFS) have been carried out on medical imaging. Bouatmane *et al.* [21] used sequential forward selection to assess various sets and to eliminate irrelevant features, in order to classify prostatic tissue taken from needle biopsies images. Rezatofighi *et al.* [189] examined the most discriminative features using sequential forward selection, artificial neural network (ANN) and support vector machine (SVM) to classify five main types of white blood cells. Because of a large amount of previous work in SFS, in this work, SFS approach is applied to a high dimensional feature vector for a comparative study.

6.3 Branch and Bound Algorithm

Preliminary work on branch and bound algorithm for selecting the optimal and the most favourable subset of features in pattern recognition applications was undertaken by Fukunaga, K (1992) [63]. Branch and bound algorithm relies on procedures that select a reduced subset of D_s features from a primary larger set of D_a inputs, where a function (J) is used as evaluation criterion. This selects an optimal feature set without exhaustively exploring the entire search space. It should be noted that, for any branch & bound algorithm, the (J) function must meet the monotonicity condition.

$$J(X_p) \geq J(X_{ch}); \qquad X_{ch} \subseteq X_p.$$

In brief, branch and bound algorithm assembles a search tree, including end-point leaves, with target subsets of (D_s) selected features. The start node (root) represents all initial input features (D_a). From this node follows a top-down tree structure, with branch descendants that are evaluated and updated at nodes, based on criterion function (J), and the process is called bound algorithm (the best updated evaluation value). The branches are extended first based on the number of features $(D_a - D_s)$ that should be cut-off. Simultaneously, the bound is updated, as the search tree is growing and leaf nodes are reached. Afterwards, the sub-tree will be pruned, so that the associated evaluation value is less or equal to the bound. Search and evaluation theories typically suffer from certain drawbacks, and this method of analysis has a number of limitations. Perhaps the most serious disadvantage of this method is that the computation of criterion value is usually slow.

Different studies have been carried out on investigating branch and bound model, and modifications have been made to improve the traditional performance.

In reviewing the literature, different methods have been found, including typical and conventional branch and bound (BB) [63], efficient branch and bound (BB^+) [258], and fast branch and bound (FBB) [216].

Recently in 2013, a globally optimal selection framework has been proposed using regression [98]. The results, as shown in [98] indicate computational efficiency and effectiveness of that framework, while shortcomings of existing criterion function (J) is overcome. In reviewing the literature, Stiglmayr *et al.* [218] conducted a series of trials using Branch & Bound methods for medical image registration. Up to date, no

work was found in the literature on the question of branch and bound efficiency in feature selection for medical images, and for blood smear slides in particular. Our study has the aim of assessing the effectiveness of branch and bound with evaluation function using regression in feature selection to reach optimal feature subset.

6.4 Experimental Result on Feature Selection

HDMR approach: The initial configuration and setting for this experiment is based on steps in [267]. All samples (140) are used for the RS-HDMR accuracy test. Also, the maximum order for approximation of the first order $\{f_i(x_i)\}$ terms is 5 where 3 is maximum assigned order for second order $\{f_{ij}(x_i, x_j)\}$. Also a ratio control variate (see Section 2.1 in [267]) to supervise and regulate the Monte Carlo integration error with 10 iterations is set for the first and second order RS-HDMR component functions. It also should be noted that in the initial setting to ignore insignificant component functions from the HDMR expansion where the current white blood cell classification system has a high number of input features, a threshold mechanism set to 10% (see Section 2.2 in [267]) is also used.

Global sensitivity analysis for all three feature sets are collected in table 21 where intensity feature set (see Section 5.3.1) with 788 members composed of 1-784 raw gray scale intensity value, 785 mean, 786 standard deviation, 787 skewness, and 788 kurtosis features and next, shape feature set (see Section 5.3.2) with 297 members composed of 1-7 Hu set, 8 Zernike, 9-44 Hahn, 45-80 generalized pseudo-Zernike, 81-116 Chebyshev, 117-152 Krawtchouk, 153-188 Fourier-Mellin, 189-224 Radial Harmonic Fourier , 225-260 Fourier-Chebyshev, 261-296 Gegenbauer and 297 for relative area are considered. Then a texture feature vector with 11019 members (see Section 5.3.3) composed of 1-784 gradient, 785-1568 Laplacian, 1569-2352 flat texture, 2352-2365 Haralick texture features, 2365-2371 Tamura, 2372-8667 Gray Level Run Length, and 8667-11019 for dual tree complex wavelet transform features is considered. To provide in-depth analysis of the Sobol index calculation, each of above individual ranges of features is used separately to estimate global sensitivity values

In this work based on above explanation 273 elements with exact addressed indices among all 12104 coefficients (almost 2.25%) which are the most convincing set on HDMR input - output relationship in current white blood cell classification system

are selected ($HDMR_{FV}$).

In order to compare the performance on classification accuracy using sobol HDMR, sequential forward selection (SFS) and downwards branch and bound [98] to select subset with the exact number of ($HDMR_{FV} = 273$) are also addressed. In connection with these two approaches, many feature indices should be listed here but an exhaustive review is beyond the scope of this current work. Eventually, to do a comparative sensitivity analysis, two feature vectors (SFS_{FV}) and (BB_{FV}) are created.

Sequential feature selection: Sequential forward selection is initialized using 10-fold cross-validation by repeatedly calling a criterion based support vector machine setting (see Section 7.2). It is also with different training and testing subsets of χ_{in} and Y_{out} where selected feature are saved into a logical matrix in which row (i) indicates the features selected at step (i) with minimum criterion value.

Branch and bound: In following subset selection and in order to understand how branch & bound regulates the best n-variable subset of invariant aforementioned features, in this work downwards branch and bound to select subset for least squares regression problems, $Y = \chi \times K$, is addressed. In this approach χ are independent feature variables, Y are white blood cell classes and K is a parameter to minimize regression error in approximating calling a criterion $J = 0.5 \times (Y - A * K)' \times (Y - A * K)$. More details are addressed in Kariwala *et al.* work [98].

Therefore, this study may leads a difference between classification performance rate (see Table 22) for these feature selection algorithms.

6.4.1 Feature Selection Settings

Feature selections are addressed in section. 6.1. This framework profits RS-HDMR implementation to do a comprehensive global sensitivity among all features. RS-HDMR requires initial setting to implement. All samples (140) are used for the RS-HDMR accuracy test. Also, the maximum order for approximation of the first order terms is 5 where 3 is maximum assigned value for second order. Also a ratio control variate to regulate the Monte Carlo integration error with 10 iterations is set for the first and second order RS-HDMR component functions. More details about these settings is found in [267].

In a comparative study (see Section 6.4) sequential forward selection is initialized using 10-fold cross-validation by repeatedly calling a criterion based SVM.

6.5 Comparison of the Proposed Approach to State-of-the-Art

To date, limited work with regard to blood classification has been able to draw attention to feature selection algorithms. Few studies investigating sequential forward selection (SFS) have been carried out on medical imaging. Bouatmane et *al.* [21] used sequential forward selection to eliminate irrelevant features in a prostatic tissue classification. In other work, Rezatofighi et *al.* [189] examined the most discriminative features using sequential forward selection and support vector machine (SVM) to classify five main types of white blood cells. The key problem with this sequential forward selection explanation is that sequential feature selection argument relies heavily on qualitative analysis of classifier and its performance depends on classifier settings. In these wrapper algorithms (such as SFS) there is no way to revise feature vector to remove or add feature variables after the addition or removal of other features. The number of selected features is totally controlled by user intervention and there is no automated way to control this stop number with reference to the nature of features. In addition, there exist no procedure to look over to degree of sensitivity of features to rank them for a specific dataset.

To sum up, in last studies so far there is no chance to rank and score candidate features for an unknown dataset. This work addresses a formulation of a highly discriminative score between different candidate features, and it should reflect the confidence in choosing one feature set over others.

This work first applied sort of statistical approaches to maintain a set of relevant and least redundant features among all candidates (see Section. 5.6). This procedure ensures that these features are not redundant before any feature selection strategy.

Article references were searched further for additional relevant publications, and no other work pertaining to the question of HDMR efficiency in feature selection for medical images and blood smear slides in particular was found. RS-HDMR concepts and practical implementation are borrowed from two articles [4,267] that are published in journals of mathematical chemistry and environmental modelling & software.

RS-HDMR emerged as reliable input-output relationship where full feature sensitivity analysis based on Sobol sequences is extracted. RS- HDMR gives a comprehensive review of the importance and sensitivity rate for feature candidates. The number

of optimum features as well as the ranks are mentioned automatically without user intervention. Once, these candidates are selected, only these high rank coefficients will be applied for next coming data set with the same condition (see Table. 21). It is obvious that results could be changed for a different dataset and RS- HDMR will adjust input-output modelling with new conditions. Sobol -HDMR (see Section. 6.1) works independently to classifier settings and this is another superiority of HDMR over sequential feature selection argument.

6.6 Feature Selection Contributions

One of the convincing contributions is the Random sampling-high dimensional model representation (RS-HDMR) in combination with global sensitivity analysis using Sobol index, for feature selection. This algorithm is a significant development as the most commonly used approaches, i.e. sequential feature selection, can not be used without a typical classifier. The results of the these methods are changeable when the the classification settings are variable. Sobol RS- HDMR overcomes these problems. RS-HDMR ranks the features using a Sobol criterion for interactions between input (individual features) and output (class) variables. A Sobol HDMR procedure is developed for extracting features rank for white blood cell detection without the need for computing classification feedback criteria. This procedure is found to be simple, accurate and more intuitive.

Feature Selection

To date, limited work with regard to blood classification has been able to draw attention to feature selection algorithms. Few studies investigating sequential forward selection (SFS) have been carried out on medical imaging. Furthermore, the current existing work fail to resolve the feature importance rate and possible classification outcome. They fail to take the degree of importance and global sensitivity features into account. Also this work avoids redundant features using sort of statistical approaches. This procedure ensures that these features are not redundant before any feature selection strategy. RS-HDMR emerged as reliable input-output relationship where full feature sensitivity analysis based on Sobol sequences is extracted (see Table. 21).

Table 21: Global sensitivity analysis (top to down: a, b) for RS-HDMR expansion, in connection with total features over each white blood cell image

	Sobol index: Assigned Intensity & Shape feature set			
Feature	**Total**	**Effective**	**Sobol**	**Comment**
Intensity	788	38	0.38	Calculations indicate that indices: 711, 443, 284, 191 and 456 (in range of gray scale intensity value) and 785 (mean) have the first five most discriminative power.
Shape	297	18	0.82	Calculations indicate that indices: 44 (Hahn coefficient), 155,156 (in range of Fourier-Mellin), 189, 190 (in range of Radial Harmonic Fourier) and 254 (in range of Fourier Chebyshev) have the first six most discriminative power.

	Sobol index: Assigned texture feature set			
Feature	**Total**	**Effective**	**Sobol**	**Comment**
Gradient	784	43	0.44	Where first five indices including 589, 185, 266, 658 and 659 have the most discriminatory power with total $S_i = 0.41$.
Laplacian	784	4	0.17	A weak link may exist between Laplacian and desired cell classes.
Flat texture	784	13	0.17	A weak link may exist between Flat texture and desired cell classes.
Haralick	13	9	0.70	Almost majority of Haralick coefficients has effective impact on classification.
Tamura	6	3	0.60	With considering half of Tamura elements an acceptable sensitivity index is accessible.
Run Length	6296	34	0.62	Just by selecting a very small subsets of features a good predictor is built.
DT-CWT	2353	111	0.64	With almost 4.7% of total elements convincing input- output relationship is built.

Chapter 7

Classification

Machine learning and pattern recognition play critical role in the digital medical imaging field, including computer-aided diagnosis and medical image analysis. Medical pattern recognition essentially requires "learning from samples". Classification of objects such as white blood cells into specific white blood cell classes based on input features (e.g., shape, intensity, and texture) is obtained from segmented leukocyte candidates. In white blood cell analysis, a well defined system is initially created as an explanation of its features and then classifies the cell based on that after applying feature selection strategies such as sequential forward feature selection, improved branch and bound algorithm and high dimensional model representation. The results of white blood cell classification are not always perfect and numerous factors affect the results. This work examines Convolutional Neural Networks (LeNet5) [117] and support vector machine (SVM) [13] in connection with white blood cell classification.

7.1 Convolutional Neural Networks (LeNet5)

Traditional manual-designed feature extractors are typically computationally intensive and need prior theoretical and practical knowledge of the problem at hand. They often cannot process raw images directly, while in classification scenario, automatic methods which can retrieve features directly from raw data are generally preferable. These trainable automatic systems solve classification problems without prior knowledge on the data and features. A convolutional neural network (CNN) is a multilayer perception with a special topology containing more than one hidden layer. It allows

for automatic feature extraction within its architecture and has as input the raw data.

7.1.1 The Standard CNN Formulation

We will investigate Convolution Neural Networks [117] which are sensitive to the topology of the images being classified. An CNN uses a feed-forward method for neurons feeding and back propagation for parameters training. The main advantage of the CNN approach is its ability to extract topological properties from the raw gray-scale image automatically and generate a prediction to classify high-dimensional patterns. An CNN is composed of two distinct parts. The first part consists of several layers that extract features from the input image pattern by a composition of convolutional and sub-sampling layers. Conceptually, visual features from local receptive fields [117] are extracted by an extended 2D convolution approach to gain the appropriate spatially local correlation present in the input images. Since the precise location of an extracted feature is in-consequent and dispensable, resolution reduction by 2 of the features is followed through the sub-sampling layers. The second distinct part categorizes the pattern into classes. In general, an CNN consists of three different layers: convolution layer, sub-sampling (max-pooling) layer and an ensemble of fully connected layers.

7.1.2 Literature Survey

There is a considerable amount of literature dedicated to using convolutional neural network (CNN), starting with Lawrence *et al.* [118] in 1997 presenting a hybrid neural network solution to automate facial feature detection. In last decade, CNN is very often used in different signal detection applications. The CNN has been used for object recognition [121] and handwriting character recognition [117, 119, 210]. Simard [210] examined various neural networks performance on visual handwriting recognition tasks. Applications range from FAX documents, to analysis of scanned documents and MNIST [120] data set.

Lauer *et al.* [117] introduced a trainable feature extractor based on convolutional neural network to recognize handwritten digits. The results on the MNIST data set showed that the system provided performances comparable in a black box data without prior knowledge. Cecotti *et al.* [26] presented a model based on a convolutional

neural network (CNN) to detect P300 waves as brain reflections in the time domain. Krizhevsky *et al.* [112] used a deep convolutional neural network consisting of five convolutional layers and three fully-connected layers to recognize and classify the 1.2 million high-resolution images into the 1000 different classes. The results on the test data was a top-5 error rate of 17.0% which is better than the previous state-of-the-art on the specific data set.

In medical images research on automatic feature extraction and using CNN in particular is still an open research topic and this work addresses this subject.

7.1.3 Experimental Result with CNN

This section presents the white blood cells classification results obtained by the proposed approaches on the existing database (115 learning samples and 25 testing ones) using two types of classifiers: support vector machine with image feature intensity values (see Section 5.3.1) and CNN. The confusion matrices and misclassification error rates are shown in tables 22–24.

In the current study, we use an CNN with the architecture of *LeNet5* [117](see Fig. 31). In the first layers (properties extractors) convolutional filters in a 5×5 pixels window are applied over the image. It is highly recommended to add two blank pixels at each four directions to avoid missing real data at each border in convolution computations. The number of alternative three main layers depends on input database and can be varied between different input size to get better performance and confidence. In this work a *LeNet5* with eight layers is used (including first layer as input gray-scale image and also output layer). Each convolution layer (C-layers) has different feature maps, C_1 is composed of 6 units while C_3 has 16 and C_5 has 120 units. Also because of convolution windows size (5×5) and input size (28×28), the size of each convolution layer is defined as shown in fig. 31: C_1 is 28×28, C_3 10×10, and C_5 is 1×1, a single neuron.

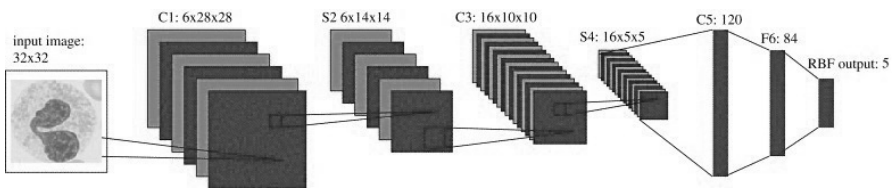

Figure 31: LeNet-5 structure in modelling CNN for a 28×28 input image

Confusion Matrices:

For all available 115 (training) and 25 (testing) samples the best scenario in confusion matrices for CNN (recognition rate after 105 epoch) is summarized in table 22, linear SVM with dimension reduction using K-PCA [253] with 2nd degree polynomial is summarized in table 23, and linear SVM without dimensionality reduction is summarized in table 24 below.

Table 22: Confusion matrices for CNN, total over testing images

	CNN: Assigned WBC 5 classes				
Known	**Basophil**	**Eosinophil**	**Lymphocyte**	**Monocyte**	**Neutrophil**
Basophil	0.625	0.125	0.250	0.00	0.00
Eosinophil	0.00	0.95	0.05	0.00	0.00
Lymphocyte	0.125	0.00	0.875	0.00	0.00
Monocyte	0.00	0.00	0.00	0.80	0.20
Neutrophil	0.00	0.00	0.00	0.014	0.985

Table 23: Confusion matrices for Linear SVM with feature set dimensionality reduction using K-PCA, total over testing images

	Linear SVM&K-PCA: Assigned WBC 5 classes				
Known	**Basophil**	**Eosinophil**	**Lymphocyte**	**Monocyte**	**Neutrophil**
Basophil	0.60	0.00	0.30	0.10	0.00
Eosinophil	0.00	1.00	0.00	0.00	0.00
Lymphocyte	0.30	0.10	0.60	0.00	0.00
Monocyte	0.00	0.00	0.20	0.80	0.00
Neutrophil	0.10	0.00	0.20	0.00	0.70

Table 24: Confusion matrices for Linear SVM without dimension reduction, total over testing images

	Linear SVM (without dimensionality reduction): Assigned WBC 5 classes				
Known	**Basophil**	**Eosinophil**	**Lymphocyte**	**Monocyte**	**Neutrophil**
Basophil	0.30	0.00	0.70	0.00	0.00
Eosinophil	0.00	1.00	0.00	0.00	0.00
Lymphocyte	0.40	0.10	0.50	0.00	0.00
Monocyte	0.20	0.00	0.00	0.80	0.00
Neutrophil	0.00	0.00	0.10	0.20	0.70

In particular, for normal white blood cells using CNN 85% of known WBCs were classified as such, with this classification rate decreasing to 74% for linear SVM using dimensionally reduced features using K-PCA, and to 66% for linear SVM (without K-PCA-based feature dimensionality reduction). So, based on the confusion matrices

with five classes the proposed CNN classifier is much more reliable and accurate even in presence of similarity among classes (specially between *Basophil* and *Lymphocyte*) in this difficult database yielding acceptable accuracy when compared to SVM (compare the third diagonal entries in confusion matrices with *(Lymphocyte)* classification rate =87% versus 60%).

CNN yields a false positive rate (FPR) of 14%, i.e., the proportion of negatives samples incorrectly classified as positive, with this FPR increasing to 23% for linear SVM using dimensionally reduced features using K-PCA, and then to 31% for linear SVM (without using feature dimensionality reduction via K-PCA). The FPR of CNN is also smaller than the FPR of a SVM using kernel PCA and it again confirms the effectiveness of automatic feature extraction by CNN.

The CNN classifier has the acceptable accuracy by optimizing the topological features on a difficult database containing small WBCs with no restrictions on background or capturing conditions. Experimental results indicate that a system based on an CNN offers an improved recognition accuracy even in presence of poor quality samples and multiple classes. Another advantage of CNN it extracts features automatically while in most other classifiers the features are chosen by the designer. It is expected that classification accuracy will be further improved by extending the data set size (especially to avoid confusion between *Basophil* & *Lymphocyte* cells since their shapes are very similar in small magnification images) and also by optimizing the CNN structure to reach higher performance in training and testing. However, CNN-based systems are very slow convergence of the loss during training particularly when the number of iterations increases during the training. These systems can be difficult to implement and are usually slower than typical classifiers.

It should be noted that in CNN the most common method to reduce over-fitting on this limited image data and also to reach better performance is to artificially enlarge the dataset using different transformations that can be addressed for future work.

7.2 Support Vector Machine(SVM)

Studies and results indicate that support vector machine analysis offers remarkable recognition accuracy even in presence of low number of samples and multiple classes. Advances in implementation result is the possibility of extending the use of this

classifier to quantitatively measure the subtypes of cells (sub-differentiation) in the entire field of haematology analysis.

7.2.1 The Standard SVM Formulation

Support vector machines are an example of a well-known linear/non-linear two-class classifier. Let the notation x_i (patterns) be the i_{th} vector in a dataset sample $(x_i, y_i)_{i=1}^{n}$ where y_i is the label associated with x_i. A linear discriminant function is defined implicitly by $f(x) = \omega^T x + b$. A simple and naive non-linear classifier is obtained by mapping data from the input space using $f(x) = \omega^T \phi(x) + b$ where ϕ is a kernel mapping function. A linear combination of the training samples can be expressed as the weight vector $\omega = \sum_i^n \alpha_i x_i$. The classifier in non-linear approach takes the form: $f(x) = \sum_i^n \alpha_i \phi(x_i)^T \phi(x) + b$. The maximum margin classifier in support vector machine is the discriminant function that maximizes the geometric margin $\frac{1}{\|\omega\|}$. To allow errors and misclassified inputs, the optimization problem can be formulated as a minimization over ω and b of the function $\frac{1}{2}\|\omega\|^2 + C\sum_{i=1}^{n} \zeta_i$, where C is a constant value, subject to the inequality constraints $y_i(\omega^T x_i + b) \geqslant 1 - \zeta_i$, and $\zeta_i \geq 0$. This optimization problem can be solved in dual form using the Lagrange multipliers as follows [13]. More detailed mathematical treatment of SVM and its implementations can be found in [13, 117].

7.2.2 Literature review

There are increasing evidences that prove support vector machines are being advantaged and popular in image classification. It has long clinical classification success in use. Numerous studies have attempted to explain SVM in medical imaging such as found in [47, 54, 111, 129, 183, 220].

7.2.3 Experimental Result with SVM

Support vector machine (SVM) as a popular classification can efficiently perform non-linear with using kernel trick in biomedical and biological applications. Common kernel functions addressed are sigmoidal, polynomial kernels and radial basis functions (RBFs) where kernel parameters have a direct impact on the decision boundary of the support vector machine [13]. The lowest degree polynomial (polynomial with $D = 1$)

performed best in which several kernels of radial basis function (RBF) and polynomial type were experimented. As in many other bio-informatics frameworks radial basis function and polynomial kernels lead to over-fitting in our high dimensional problem involving a large number of intensity, shape and texture features (12104) with a small input data set (28 samples for each of five WBC classes) [13]. Further, to reach an optimal hyperplane in this research Soft-Margin SVM which is more robust to outliers tries to maintain misclassification points (slack variables = ξ_i) to minimum while maximizing margin. Also to generalize the formulation to multi-class SVMs in this work One-versus-all to train five classifiers, one for each class against all other classes is used and the predicted category is the class of the most confident classifier. Next, given a linear SVM classifier with 10 fold - cross validation is examined in this work. 10 fold - cross validation is commonly used in presence of small size (140 samples) of the training and testing data set and with large number of parameters (12104 = all feature coefficients) to avoid over fitting and to cover all observations for both training and validation.

Three different sets of training and testing are introduced consisting of the feature vector using high dimensional model representation feature selection, sequential feature selection, branch and bound (sections. 6.4, 7.2.3) separately.

In this section, a set of 140 $8-$bit gray scale poor images with low magnification $(28 * 28)_{px}$ in five balanced dataset (see Fig. 32) are used. We have randomly chosen the data to construct the training set after removing almost 20% of the data to be used for testing the SVM classifier.

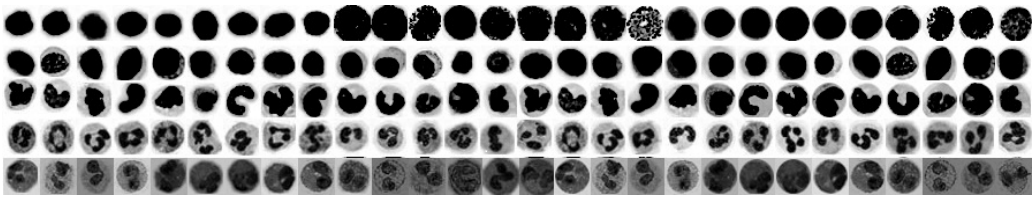

Figure 32: WBC testing data, each row, top to bottom: Basophil(B), Lymphocyte(L), Monocyte(M), Neutrophil(N), and Eosinophil(E).

Confusion Matrices

A 5×5 confusion matrix is used to represent the different possibilities of the set of instances. The matrices are built on five rows and five columns: Neutrophil; Monocyte;

Lymphocyte; Eosinophil; and Basophil representing the known WBC classes whereas for each matrix, each row the values are normalized to sum to 1. Several standard performance terms such as true positive rate or the recall (correctly identified- TP), false positive rate (incorrectly identified- FP), true negative rate (correctly rejected- TN), false negative rate (incorrectly rejected- FN), accuracy (proportion of the total corrected predictions - AC), precision (proportion of the corrected predicted positive cases -P) have been extracted for the confusion matrix. This work addresses kappa (κ) measure as it provides accuracy (AC) versus precision (P) interpretation across class categories [116]. Common Cohen's un-weighted κ interpretation is:

$$\begin{cases} \leq 0 & \Rightarrow Poor \\ [0, 0.20] & \Rightarrow Slight \\ [0.21, 0.40] & \Rightarrow Fair \\ [0.41, 0.60] & \Rightarrow Moderate \\ [0.61, 0.80] & \Rightarrow Substantial \\ [0.81, 1.00] & \Rightarrow AlmostPerfect \end{cases}$$

The experiments are categorized into set of named selected 273 out of 12140 features (FV_{SFS}, FV_{BB} and FV_{HDMR}) also with a total high dimensional feature vector with 12140 members (FV_{Total}).

Statistical performance measure is analyzed using analysis of confusion matrices for each named feature & SVM summarized in tables 25a, 25b, 25c and 25d. Further statistical tests revealed that given a small number of input samples (140) in high dimensional feature sets (= 12140) using non-linear SVM kernels leads to over-fitting.

The result, as shown in table 25, indicates that for normal low resolution white blood cells using linear SVM & all feature vector FV_{Total} 85% of known white blood cells were classified as such, with this classification rate decreasing to 83.5% for FV_{BB} and 83% for (FV_{HDMR}) (see Table 25 b,d) where the efficiency of (FV_{SFS}) is also 81% which is less than proposed Sobol - HDMR with 83%. RS-HDMR classification performance with 273 elements is less and more similar where classification accuracy is also found with all 12140 coefficients and with improved branch and bound method [98] are selected. As confusion matrix tables illustrate, in this poor imaginary database there is not a significant difference between for example the all high dimensional data set and feature selected group with RS-HDMR expansion.

However, in general RS-HDMR and "improved branch and bound" are more efficient than SFS; and RS-HDMR is superior to both of the above mentioned methods. All these three methods conducted a series of trials where they are different in both their basis functions and the way they find a solution for the problem.

First, RS-HDMR selected feature vector is based on sobol calculation where the number of efficient principal coefficients are up (i.e, 273 in this work) to reach first order of sensitivity index (S_i) value close to zero (more comments in [4, 267]). Secondly, feature subset selection in improved downwards branch and bound [98] is based on least squares regression between invariant features and dependent white blood cell class where subset size to be selected is under user decision. Both these two aforementioned cases are total independent tasks before classifier involving. Following that, SFS method is a combination technique where its result is dependent on different initial setting for classifier and its scalar return value criterion. Also, it is apparent that the number of selected futures are manually assigned by user where unlike the RS-HDMR there is no way to look over to degree of sensitivity of all individual features.

The results, as shown in confusion matrix tables indicate that also HDMR results for almost each sub-group is more accurate than SFS method where also sequential forward selection algorithm is too dependent to classifier feedback as well.

Also with compare with two ground truth groups, using machines Sysmex XE-series and also Abbott CELL-DYN range (see Section 2.1) it can be seen from the data in confusion matrix tables that global sensitivity with Sobol on RS-HDMR expansion reveals 91% accuracy for Neutrophil, 65% rate for Lymphocyte and also 100% for Eosinophil while the expensive machines mentioned above provide 92.5%, 92.2%, and 87.7%, respectively in an ideal performance. It also provides 81% classification rate for Monocytes and 77% for Basophils where the results obtained from machines are 75.6% and 76.3%. The following conclusions in regard to κ coefficient can be also drawn from the present confusion matrices. The Cohen's unweighted κ coefficient of the FV_{Total}, FV_{SFS}, FV_{BB} also FV_{HDMR} are acceptable (0.81= almost perfect and $0.77, 0.79$ = substantial) in this low resolution WBC classification. Taken together, the most obvious finding to emerge from feature selection and with RS- HDMR study in particular is that all these two methods provide *substantial* performance where

lessen computational time and improve model interpret-ability to enhance generalization by reducing over-fitting possibility as well.

Table 25: Confusion matrices (top to down: a,b,c,d) for SVM classifier, totals over testing images in invariant features & linear SVM

	Linear SVM (FV_{Total}): Assigned WBC classes				
Known	**Basophil**	**Eosinophil**	**Lymphocyte**	**Monocyte**	**Neutrophil**
Basophil	0.72	0	0.21	0.03	0.04
Eosinophil	0	1.00	0	0	0
Lymphocyte	0.17	0	0.68	0.13	0.02
Monocyte	0.01	0	0.04	0.90	0.05
Neutrophil	0	0	0	0.03	0.97
	Linear SVM (FV_{BB}): Assigned WBC classes				
Known	**Basophil**	**Eosinophil**	**Lymphocyte**	**Monocyte**	**Neutrophil**
Basophil	0.69	0.04	0.27	0.00	0.00
Eosinophil	0	1.00	0	0	0
Lymphocyte	0.13	0.00	0.70	0.13	0.04
Monocyte	0.01	0 .01	0.1	0.85	0.03
Neutrophil	0.00	0.02	0.04	0.01	0.93
	Linear SVM (FV_{SFS}): Assigned WBC classes				
Known	**Basophil**	**Eosinophil**	**Lymphocyte**	**Monocyte**	**Neutrophil**
Basophil	0.72	0	0.24	0.04	0
Eosinophil	0.00	1.00	0.00	0.00	0.00
Lymphocyte	0.17	0	0.62	0.14	0.07
Monocyte	0.02	0	0.18	0.80	0.0
Neutrophil	0.01	0	0.01	0.04	0.94
	Linear SVM (FV_{HDMR}): Assigned WBC classes				
Known	**Basophil**	**Eosinophil**	**Lymphocyte**	**Monocyte**	**Neutrophil**
Basophil	0.77	0.01	0.17	0.01	0.04
Eosinophil	0	1.00	0	0	0
Lymphocyte	0.16	0.01	0.65	0.1	0.08
Monocyte	0.04	0	0.13	0.81	0.02
Neutrophil	0.02	0.01	0.01	0.05	0.91

7.3 Classification Settings

In this framework, two classifiers namely, support vector machine and convolutional neural network are used. Setting and parametrization of support vector machine is addressed in following table (see Table 26). It should be said that SVM in this work with limited data used linear kernel. However, it could be changed in other enough large dataset.

As for the convolutional neural network, all the parameters including the structure, number of layers and selection of fully connected network are varying for different

Table 26: Support Vector Machine: Settings

	SVM; supervised classifier	
Parameter	**Value**	**Comment**
Kernel	Linear	The lowest degree polynomial performed best in high dimensional problem involving a large number of features with a small input data set.
Margin	Soft-Margin	Robust to outliers to minimum misclassification points while maximizing margin.
Multi-class	One-versus-all	One for each class against all other classes is used and the predicted category is the class of the most confident classifier.
Training	23	23 out of 28 samples in each cross validation step are considered to build training set.
Validation	10 fold - cross validation	To avoid over fitting and to cover all observations for both training and validation.

Table 27: Convolutional neural network: Settings

	CNN; Topological Features	
Parameter	**Value**	**Comment**
Convolutional windows	5×5 pixels window	It is highly recommended to add two blank pixels at each four directions to avoid missing real data at each border in convolution computations.
Convolution layers	Different values	C_1 is composed of 6 units while C_3 has 16 and C_5 has 120 units.
Convolution size layers	Different values	C_1 is 28×28, C_3 10×10, and C_5 is 1×1, a single neuron.
Sub-Sampling	Max Pooling	S_2 is 6× 14 × 14, S_4 is 16×5 × 5.
Validation	10 fold - cross validation	To avoid over fitting and to cover all observations for both training and validation.

dataset. Convolution Neural Network in this work is composed of convolution layers, sub-sampling (max-pooling) and an ensemble of fully connected layers such as radial basis function (RBF) networks (see Fig. 31). These CNN setting must be interpreted with caution and these initialization cannot be extrapolated to all possible dataset with different conditions. The CNN settings with respect to current dataset which is only with 28 samples for each class in low resolution size (28 × 28) is addressed in fig. 31 and table 27.

Chapter 8

Conclusions and Future Work

There are many challenging problems in automatic processing of cytological of image blood cells. The main problems include large variation of blood cells, occlusions, low quality of images and difficulties in getting enough real data. These problems are addressed in this work. In this work, a step-by-step efficient segmentation and classification algorithm have been presented automatic detection and segmentation of microscopic blood imagery. Experimental results indicate that our system offers good segmentation and recognition accuracy with normal samples. The performance of the proposed method has been evaluated by comparing the automatically extracted cells with manual segmentations by a pathologist from GHODS polyclinic (Tehran, Iran). In this work, a framework divided into four main stages: image pre-processing, feature extraction, feature selection and classification is proposed. We provide literature survey and point out new challenges.

First, a reliable pre-processing system that may be used under different conditions (such as low quality, unfavourable resolution, varying inconsistent illumination conditions and also the complexity staining techniques) is introduced. Next, separation of different cells as well as the identification of RBC and WBC is resolved. An efficient and highly accurate local binarization method is introduced here. Cell separation is accomplished using cutting edge image segmentation and boundary detection techniques in combination with morphological techniques with the goal of improving the accuracy of complete blood count (CBC). The available data is poor quality and therefore shape and inside structures are difficult to estimate. These conditions include noisy low resolution blood smear images. White blood cells texture, cytoplasm

and membrane are non-uniform staining and granular white blood cell shapes are also difficult to detect. As a result, we have introduced efficient invariant shape, intensity and texture features for white blood cells classification in this difficult dataset with low resolution images.

Statistical measures were used to investigate redundancy and relevance of features. They include Kolmogorov - Smirnov (KS) and Wilcoxon- Mann-Whitney (WMW) tests, Pearson, Spearman and Kendall rank correlation coefficients. These statical tests show a low degree of redundancy among these features. Almost all aforementioned features (except for Legendre moments) are independent and there is no redundant information in them. Furthermore, this work concentrates on usefulness of feature selection in presence of big data with high dimensional invariant features in connection with white blood cell classification. In our work on white blood cell classification features vectors have 12140 components and lot of effort is devoted to feature selection. This work examines and presents the effectiveness of three methods such as sequential feature selection (SFS) set, improved branch and bound (BB) and random sample high-dimensional model representation (RS-HDMR). RS-HDMR using Sobol rank calculation automatically detected 273 best features and then we used sequential feature selection (SFS) set, improved branch and bound (BB) to select the best 273 features as well.

All these three SFS, RS-HDMR and "improved branch and bound" substitute large number of features (D_{12104}) to subset of features (D_{273}) to avoid curse of dimensionality, reduce feature measurement and computational burden and then recall the SVM classifier based on these selected features.

We subsequently tested the set of selected features using SVM and determined that RS-HDMR produced the most discriminatory features. These findings suggest that, in general, RS-HDMR emerged as a reliable input-output relationship predictor of small distorted WBCs and their own classes to allow the full feature sensitivity analysis based on Sobol sequences.

One of the more significant findings to emerge from this study is the possibility of extending this framework to entire field of hematology analysis, stool examination or other similar medical research. Furthermore, the introduced method being simple and easy to implement is best suited for biomedical applications in clinical settings.

This work aims at development of publicly available software for complete blood

count test for automatic processing of blood slide images. Of course with good recognition accuracy even in presence of low resolution images and noise.

8.1 Original Contributions of the Thesis

The thesis addresses the problem of segmentation and counting red blood cells along with classification of cytological images of white blood cells in peripheral blood smear for complete blood count (CBC) test. In this concept, this study made an effort to reach a framework to extract blood test parameters even in presence of low resolution images. This work calculates main CBC test indices such as RBC count, red cell distribution width (RDW), WBC Count and WBC differential (see Section. 1.2.1).

The main contribution of this study is in forming a complete framework of methodologies and procedures required for automatic processing of normal blood slide images for complete blood count diagnosis test. The system is able to process the low resolution and degraded images where manual analysis of microscopic blood slides which is not only a tedious task and but also likely to fail or make human errors.

This section lists main achievements of the thesis. The finding of this work points out some contributions to the literature in normal blood segmentation and classification.

- More accurate white blood cells classification in presence of low quality images.
- The introduction of using semi-interquartile range, variance statistical approach to reach channel color selection criteria in presence of different gray scale options for blood smear microscopic images (see Section 3.2.1).
- Study and investigation of more accurate blood smear image pre-processing, which it includes Bayesian Non-local means as image de-noising, utilizing Kauwahra filter for white blood edge preserving (see Sections 3.2.2, 3.2.3).
- The introduction of an improved and more generalized binarization using merged Niblack as local and Otsu as global techniques to improve foreground/background segmentation of blood smear microscopic images (see Section 4.3.1).
- Study and investigation of white blood cell image separation using improved active contour model without an edge, morphological operations and edged images

for blood cells separation in presence of degraded images (see Section 4.3.1).

- A comprehensive study and introduction of a set of appropriate invariant high dimensional feature coefficients such as invariant orthogonal moments, Dual-Tree Complex Wavelet Transform, Run-length for classification of blood smear microscopic images (see Section 5.3).

- Study and investigation of the redundancy and distribution behaviour of these named invariant features with approaches such as Kolmogorov - Smirnov (KS), Wilcoxon- Mann-Whitney (WMW) tests, Spearman and Kendall rank correlation coefficients for blood smear microscopic images (see Section 5.6).

- Study and investigation of feature selection to provide effective reduction of feature vector size for classification of blood smear microscopic images. Global sensitivity analysis with combination of random sampling-high dimensional model representation (RS-HDMR) and Sobol sensitivity analysis to assess discriminatory power and rank of each individual feature is addressed (section 6.1, table 21).

- The comparison of set of classifiers such as support vector machine (SVM), Convolutional Neural Networks (CNN) to evaluate their performance to distinguish between inter-classes for classification of white blood cells in blood smear microscopic images. This work extracts topological features by Convolutional Neural Networks (LeNet5) to separate white blood cell classes (see Sections 5.3, 7.1.3, 7.2.3).

Aforementioned sub-sections explain original contributions of this thesis in more detail. Blood smear image pre-processing findings are addressed in section 3.4. The original contribution emerges from Binarization & blood cell separation are found in section 4.5.

Finally I applied feature extraction & selection algorithms to obtain good discriminative features for white blood cells classification, see discussion in sections 5.7, 6.6.

8.2 Publications of the Author

The aim of [78] was to introduce an accurate mechanism for counting blood smear particles. This is accomplished by using the Immersion Watershed algorithm which counts red and white blood cells separately. To evaluate the capability of the proposed framework, experiments were conducted on noisy normal blood smear images. This framework was compared to other published approaches and found to have lower complexity and better performance in its constituent steps; hence, it has a better overall performance.

In paper [113] we discuss applications of pattern recognition and image processing to automatic processing and analysis of histopathological images. We focus on two applications: counting of red and white blood cells using microscopic images of blood smear samples and breast cancer malignancy grading from slides of fine needle aspiration biopsies. We provide literature survey and point out new challenges.

In third article [72] we discuss improved binarization using merged Niblack and Otsu techniques to improve foreground/background segmentation of blood smear microscopic images. We aim at more accuracy in terms of minimizing the number of close pairs of cells that are merged into single cells during binarization process.

In conference work [75] a convolutional neural network (CNN) to extract topological features is proposed. The proposed classifiers were compared through experiments conducted on low resolution cytological images of normal blood smears

In [73] we particularly interested in classification and counting of the five main types of white blood cells (leukocytes) in a clinical setting where the quality of microscopic imagery may be poor. In this paper we implement a machine learning system based on using extracting features by Dual-Tree Complex Wavelet and SVM as a classifier.

In [74] we analyze the performance of white blood cell recognition system for three different sets of features and these features are combined with the Support Vector Machine (SVM) which classifies white blood cells into their five primary types. This approach was validated with experiments conducted on digital normal blood smear images with low resolution.

In conference work [76] we use a high dimensional vector addressing invariant features. Global sensitivity analysis using Sobol RS-HDMR which can deal with independent and dependent input variables is used to assess dominate discriminatory

power and the reliability of feature models in presence of high dimensional input feature data to build an efficient feature selection.

Paper [77] has been submitted to *Computers in Biology and Medicine Journal - Elsevier*. It is about feature extraction and selection for White Blood Cell differential counts in low resolution cytological images. These work focus on the development of effective strategies for the understanding of invariant feature extraction and then optimal selection based on different statistically measured approaches on high-dimensional feature data in low resolution images.

8.3 Challenges & Future Work

Automatic CBC (complete blood count) is a challenging and unsolved problem. It involves classification of white blood cells into five main categories such as basophils, eosinophils, lymphocytes, monocytes and neutrophils, and detection and categorization of blood pathologies such as anemias, leukaemias, lymphomas, cholera, malaria and many others. As different white blood cell and pathologies may be differentiated by shape, texture, color and other visual cues advanced image processing and machine learning techniques need to be utilized to build reliable classification systems. An important problem to address is the separation of different white blood cell classes(mature and immature) into 20 sub-classes "information about cellular immaturity " such as mentioned in [67, Chapter 170]. It may be used to help monitor more sophisticated cases, as well as the identification of deformed RBC and white blood cell shapes with diseases [67]. Some red blood cell abnormalities case are listed here ([67], figures 160-2 to 160-15) :

I **Macrocytic anemia** : cells are larger than normal and oval in shape(arrow).

II **Sickle cells** : a sickle or crescent shape.

III **Teardrop poikilocytes** : Teardrop-shaped red cells.

IV **Rouleau formation** : chain of overlapped red cells. and etc.

Further research should be done to investigate the different techniques to address better improvement in segmentation step. This will be accomplished using cutting edge image segmentation techniques in combination with advanced machine learning

techniques for classification, with the goal of improving the accuracy of CBC reports and to isolate cells in the individual sub images. The methods such as simultaneous detection and segmentation [83] should be investigated. Feature selection is an important issue for future research. The findings are expected to be supported by future work considering different underdeveloped HDMR variations, i.e., Sobol HDMR using Quasi Monte Carlo, multiple sub-domain random sampling HDMR, or Cut-HDMR.

In this study it is assumed that the number of samples in each individual class is identical and we have a balanced database in which in practice typical proportions of the cell types are not the same in blood smear slides (e.g., neutrophil (40- 75%) vs basophil granulocytes (0.5%)). In such cases, a Breiman Random Forest (BRF) [23], deep belief networks and Restricted Boltzmann Machines classifiers may be potentially useful. The BRF algorithm can deal with imbalanced data, can handle more variables (features) than observations (large attributes, small sample), is robust for data sets containing noisy samples, and has a good predictive ability without over-fitting the data. Further, to extract a compact basis of discriminant training samples, dictionary learning techniques and sparse coding to learn each species are used. In particular, sparse coding and dictionary methods have proven to be efficient at modeling complex structures and to be robust to noise, two essential abilities for the target problem.

8.4 Acknowledgements

We would like to thank professor Nick Kingsbury from the University of Cambridge, UK for providing his Dual-Tree Complex Wavelet Transform code. We also thank Dr. Tilo Ziehn and professor Alison Tomlin from University of Leeds for providing a freely available Matlab toolbox with a graphical user interface to global sensitivity analysis of complex models. We also appreciate Aida Habibzadeh and M.D Parvaneh Saberian whose comments and suggestions helped to improve and clarify this manuscript.

Chapter 9

Appendix - Images

This section contains image information, links to normal, blood cell disorders and mature white blood cell classes.

9.1 Blood with Different Characteristics

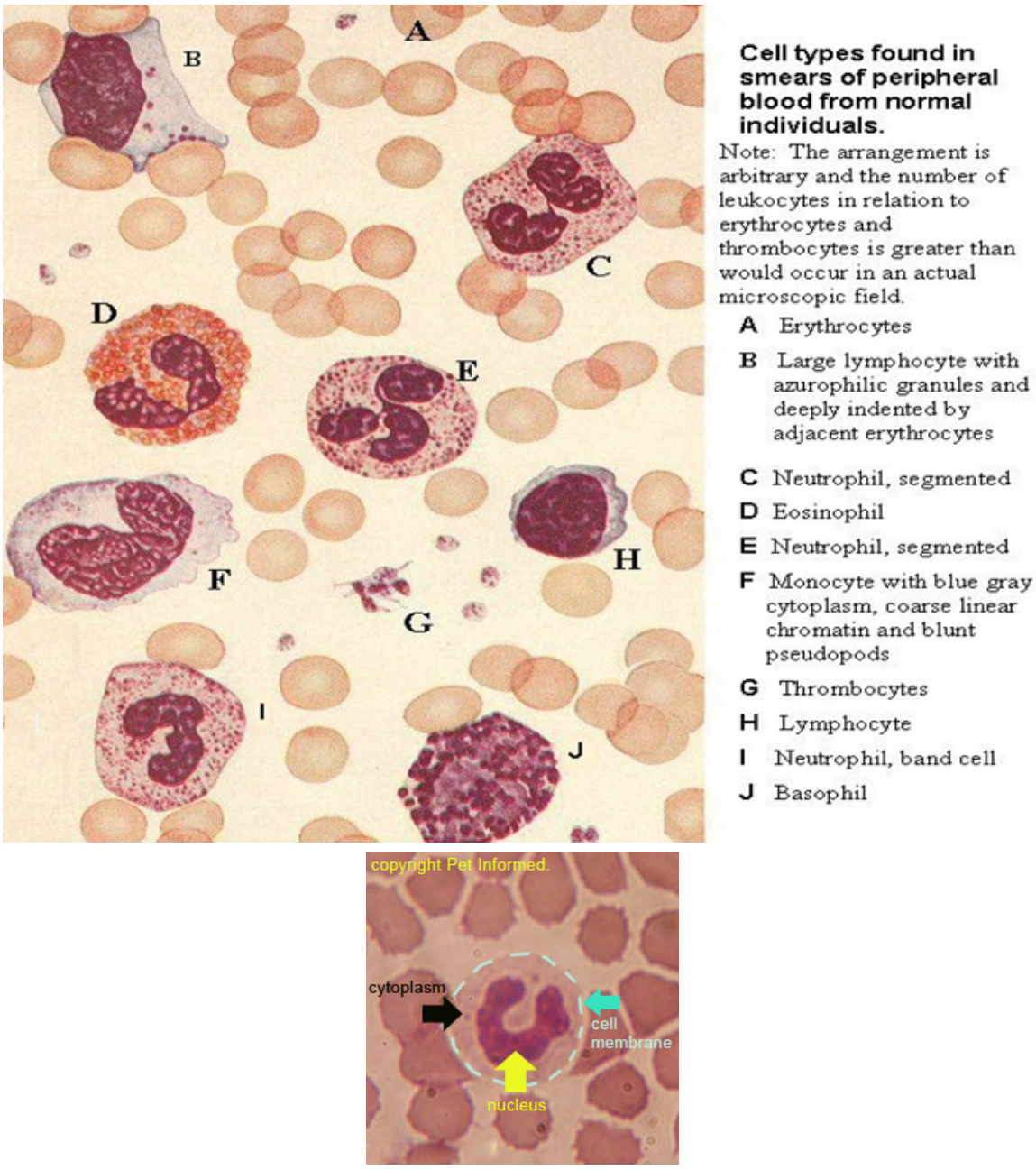

Figure 33: Glossary of human blood smear terms

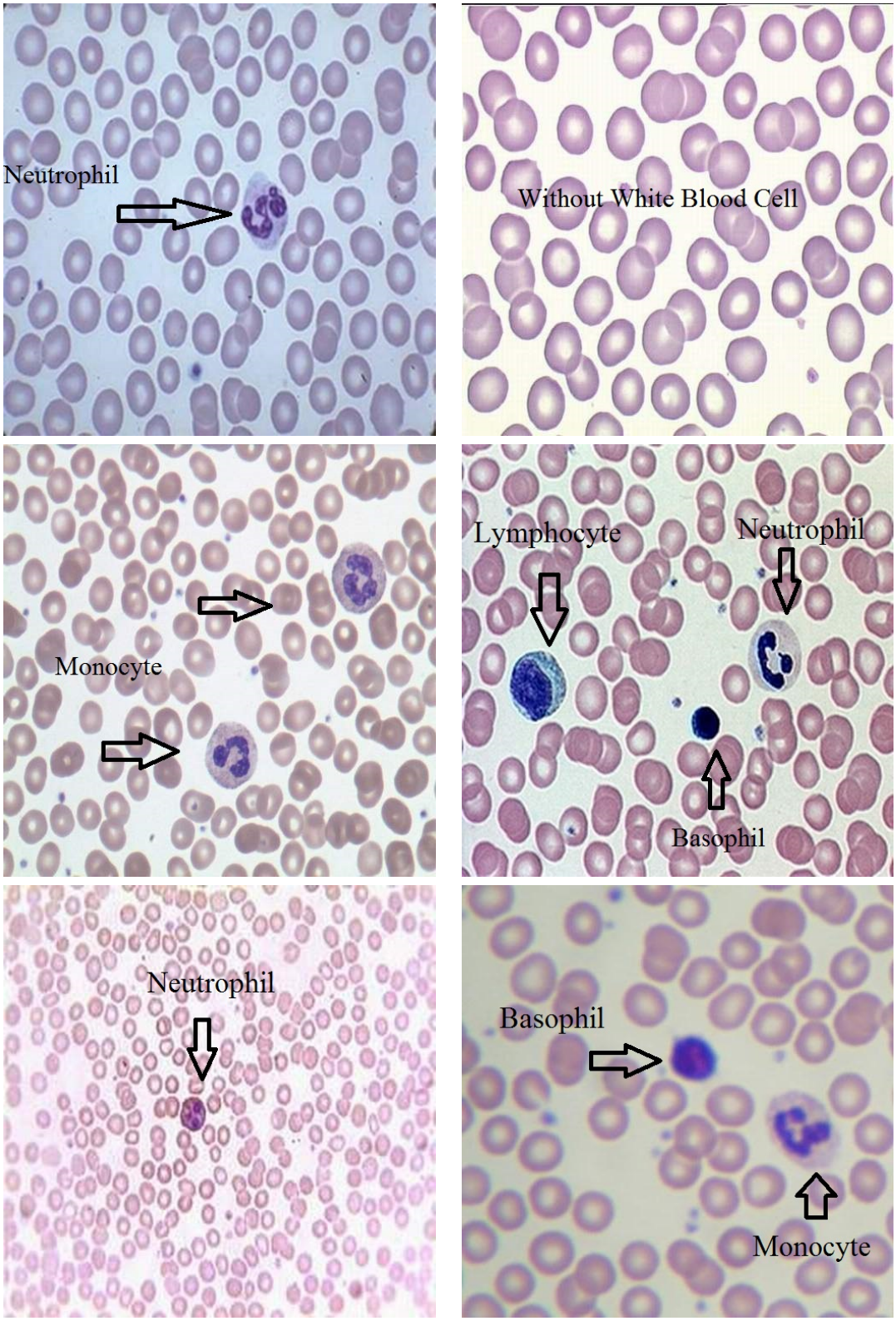

Figure 34: Normal blood smear images with different characteristics (N0–N5)

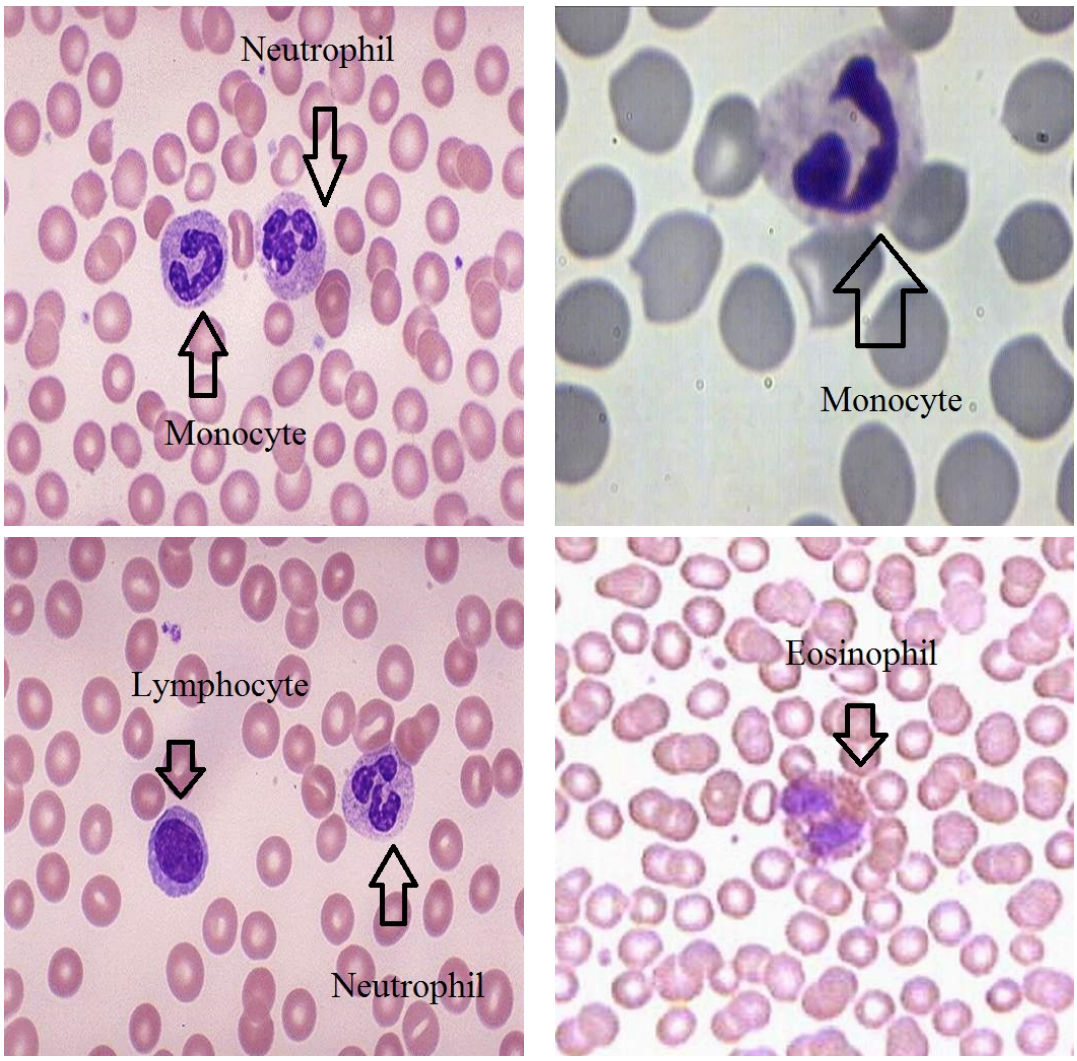

Figure 35: Normal blood smear images with different characteristics (N6–N9)

9.2 Disorders in Blood Smears

9.3 WBC classes in Blood Smears

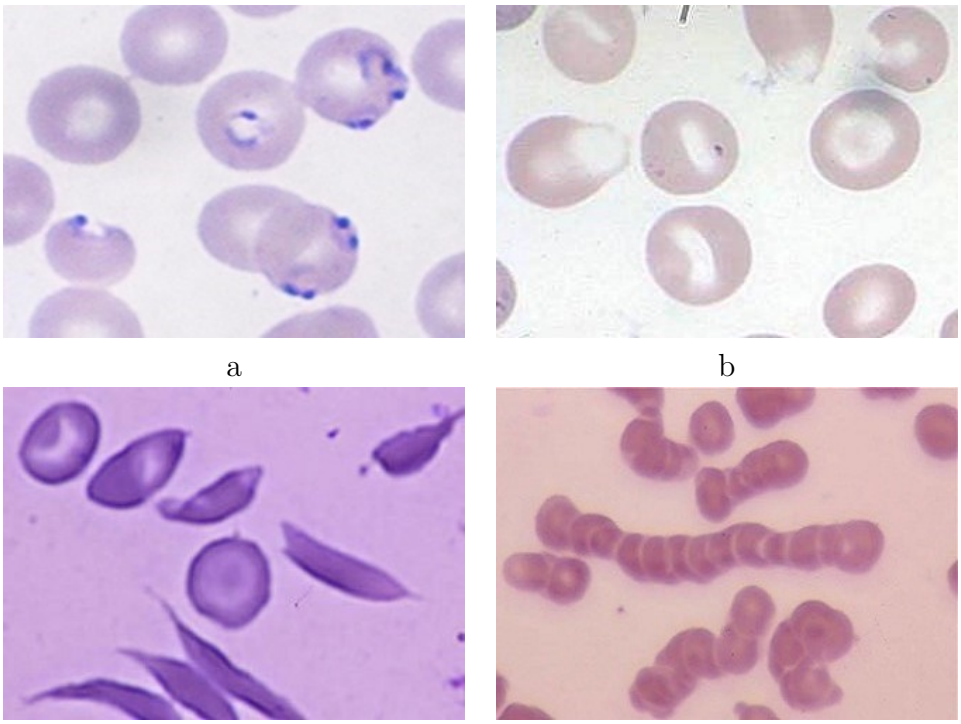

a b

c d

Figure 36: Red Blood Cell Disorders: a)Malaria(P.f) b)Pappenheimer c)Sickle Cell, d)Rouleaux

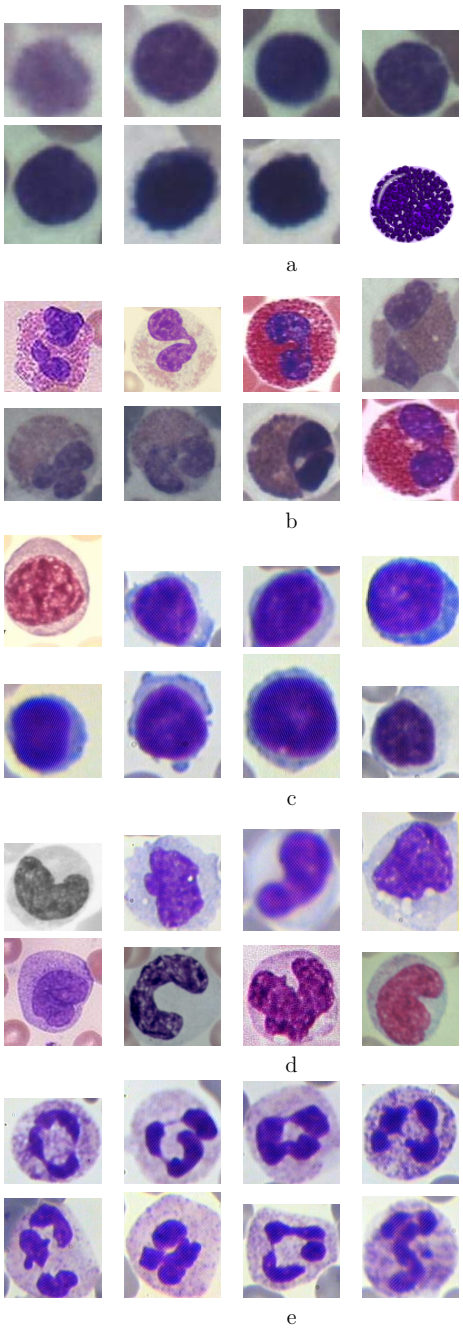

Figure 37: Samples of white blood cells : a)Basophils b)Eosinophil c)Lymphocyte d)Monocyte and e)Neutrophil (8 samples for each in different actual size)

Bibliography

[1] M. Adjouadi and N. Fernandez. An orientation-independent imaging technique for the classification of blood cells. *Particle & Particle Systems Characterization*, 18(2):91–98, 2001.

[2] Sh. Ahmad, Q. Zhang, Z.M. Lu, and M.W. Anwar. Feature-based watermarking using discrete orthogonal hahn moment invariants. In *7th International Conference on Frontiers of Information Technology*, FIT, pages 38:1–38:6, 2009.

[3] M. Albertini, L. Teodori, E. Piatti, M. Piacentini, A. Accorsi, and M. Rocchi. Automated analysis of morphometric parameters for accurate definition of erythrocyte cell shape. *Cytometry Part A*, 52A(1):12–18, 2003.

[4] Ö. Aliş and H. Rabitz. Efficient implementation of high dimensional model representations. *Journal of Mathematical Chemistry*, 29(2):127–142, 2001.

[5] J.P. Ananth and V.S. Bharathi. Face image retrieval system using discrete orthogonal moments. In *4th International Conference on Bioinformatics and Biomedical Technology (IPCBEE)*, pages 218–223, 2012.

[6] G. Apostolopoulos, S. Tsinopoulos, and E. Dermatas. Recognition and identification of red blood cell size using Zernike moments and multicolor scattering images. In *10th International Workshop on Biomedical Engineering*, pages 1–4, 2011.

[7] R. Archibald, K. Chen, A. Gelb, and R. Renaut. Improving tissue segmentation of human brain MRI through preprocessing by the gegenbauer reconstruction method. *NeuroImage*, 20(1):489 – 502, 2003.

[8] R. Archibald, H. Jiuxiang, A. Gelb, and G. Farin. Improving the accuracy of volumetric segmentation using pre-processing boundary detection and image reconstruction. *IEEE Transactions on Image Processing*, 13(4):459–466, 2004.

[9] M.R. Asadi, A. Vahedi, and H. Amindavar. Leukemia cell recognition with Zernike moments of holographic images. In *Proceedings of the 7th Nordic Signal Processing Symposium (NORSIG)*, pages 214–217, 2006.

[10] Z.V. Babic and D.P. Mandic. An efficient noise removal and edge preserving convolution filter. In *6th International Conference on Telecommunications in Modern Satellite, Cable and Broadcasting Service*, volume 2, pages 538–541, Oct. 2003.

[11] J.W. Bacusmber and E.E. Gose. Leukocyte pattern recognition. *IEEE Transactions on Systems, Man and Cybernetics*, SMC-2(4):513–526, 1972.

[12] R.R. Bailey and M. Srinath. Orthogonal moment features for use with parametric and non-parametric classifiers. *IEEE Transactions on Pattern Analysis and Machine Intelligence*, 18(4):389–399, 1996.

[13] A. Ben-Hur and J. Weston. A user guide to support vector machines. In *Data Mining Techniques for the Life Sciences*, volume 609, pages 223–239, 2010.

[14] S. Bentley and S. Lewis. The use of an image analyzing computer for the quantification of red cell morphological characteristics. *British Journal of Hematology*, 29:81–88, 1975.

[15] T. Bergen, D. Steckhan, T. Wittenberg, and T. Zerfass. Segmentation of leukocytes and erythrocytes in blood smear images. In *30th Annual International Conference of the IEEE on Engineering in Medicine and Biology Society*, pages 3075–3078, 2008.

[16] J. Bernsen. Dynamic thresholding of grey-level images. In *International Conference on Pattern Recognition*, pages 1251–1255, 1986.

[17] H.S. Bhadauria and M.L. Dewal. Efficient Denoising Technique for CT images to Enhance Brain Hemorrhage Segmentation. *Journal of Digital Imaging*, pages 1–10, 2012.

[18] S.F. Bikhet, A.M. Darwish, H.A. Tolba, and S.I. Shaheen. Segmentation and classification of white blood cells. In *IEEE International Conference on Acoustics, Speech, and Signal Processing(ICASSP)*, volume 6, pages 2259–2261, 2000.

[19] T.J. Bin, A. Lei, C. Jiwen, K. Wenjing, and L. Dandan. Subpixel edge location based on orthogonal fourier-mellin moments. *Image and Vision Computing*, 26(4):563 – 569, 2008.

[20] B. Bobier and M. Wirth. Evaluation of binarization algorithms. Technical report, Department of Computing and Information Science, University of Guelph, Guelph, ON, 2008.

[21] S. Bouatmane, M. Roula, A. Bouridane, and S. Al-Maadeed. Round-robin sequential forward selection algorithm for prostate cancer classification and diagnosis using multispectral imagery. *Machine Vision and Applications*, 22(5):865–878, 2011.

[22] D. Bradley and G. Roth. Adaptive thresholding using the integral image. *Journal of Graphics, GPU, & Game Tools*, 12(2):13 – 21, 2007.

[23] L. Breiman. Random forests. *Machine Learning*, 45(1):5–32, Oct. 2001.

[24] M. Buttarello and M. Plebani. Automated blood cell counts -state of the art. *American Journal of Clinical Pathology*, 130:104–116, 2008.

[25] E.A. Castro and D.L. Donoho. Does Median filtering truly preserve edges better than linear filtering? *The Annals of Statistics*, 37(3):1172 – 1206, 2009.

[26] H. Cecotti and A. Graser. Convolutional neural networks for P300 detection with application to brain-computer interfaces. *IEEE Transactions on Pattern Analysis and Machine Intelligence*, 33(3):433–445, Mar. 2011.

[27] J. Salmon Ch.A. Deledalle and A. Dalalyan. Image denoising with patch based PCA: local versus global. In *Proceedings of the British Machine Vision Conference*, pages 25.1–25.10. BMVA Press, 2011.

[28] H. Chan, J. Li-Jun, and B. Jiang. Wavelet transform and morphology image segmentation algorism for blood cell. In *4th IEEE International Conference on Industrial Electronics and Applications*, pages 542 –545, May. 2009.

[29] T.F. Chan and L.A. Vese. Active contours without edges. *IEEE Transactions on Image Processing*, 10(2):266 –277, Feb. 2001.

[30] S.G. Chang, B. Yu, and M. Vetterli. Adaptive wavelet thresholding for image denoising and compression. *IEEE Transactions on Image Processing*, 9(9):1532–1546, 2000.

[31] G.Y. Chen, T.D. Bui, and A. Krzyżak. Image denoising with neighbour dependency and customized wavelet and threshold. *Pattern Recognition*, 38(1):115 – 124, 2005.

[32] C.K. Chow and T. Kaneko. Automatic boundary detection of the left ventricle from cineangiograms. *Computers and Biomedical Research*, 5(4):388 – 410, 1972.

[33] J. L Coatrieux. Moment-based approaches in imaging part 2: invariance. *IEEE Engineering in Medicine and Biology Magazine*, 27(1):81–83, 2008.

[34] D. Comaniciu and P. Meer. Cell image segmentation for diagnostic pathology. In *Advanced algorithmic approaches to medical image segmentation*, pages 541–558. Springer, , 2002.

[35] H. Costin, C. Rotariu, M. Zbancioc, M. Costin, and E. Hanganu. Fuzzy rule-aided decision support for blood cell recognition. *Fuzzy Systems & Artificial Intelligence*, 7(1-3):61–70, 2001.

[36] P. Coupè, P. Hellier, C. Kervrann, and C. Barillot. Nonlocal Means-Based Speckle Filtering for Ultrasound Images. *IEEE Transactions on Image Processing*, 18(10):2221–2229, Oct. 2009.

[37] A. Cramer. Bijdrage tot de quantitative mikroskopische analyse van het bloed. *Het tellen der bloedligchaampjes*, 4(453), 1855.

[38] B. Dangott, M. Salama, N. Ramesh, and T. Tasdizen. Isolation and two-step classification of normal white blood cells in peripheral blood smears. *Journal of Pathology Informatics*, 3(1):13, 2012.

[39] D.K. Das, C. Chakraborty, B. Mitra, A.K. Maiti, and A.K. Ray. Quantitative microscopy approach for shape-based erythrocytes characterization in anaemia. *Journal of Microscopy*, 249(2):136–149, 2013.

[40] M. Portes de Albuquerque, I.A. Esquef, A.R. Gesualdi Mello, and M. Portes de Albuquerque. Image thresholding using Tsallis entropy. *Pattern Recognition Letters*, 25(9):1059 – 1065, 2004.

[41] A G. Dempster and C. Di Ruberto. Using granulometries in processing images of malarial blood. In *IEEE International Symposium on Circuits and Systems*, volume 5, pages 291–294, 2001.

[42] Z. Dengwen and Ch. Wengang. Image denoising with an optimal threshold and neighbouring window. *Pattern Recognition Letters*, 29(11):1694 – 1697, 2008.

[43] C. Desbleds-Mansard, A. Anwander, L. Chaabane, M. Orkisz, B. Neyran, P. Douek, and I. Magnin. Dynamic active contour model for size independent blood vessel lumen segmentation and quantification in high-resolution magnetic resonance images. In *Computer Analysis of Images and Patterns*, volume 2124 of *Lecture Notes in Computer Science*, pages 264–273. Springer Berlin Heidelberg, 2001.

[44] C. Di Ruberto, A. Dempster, S. Khan, and B. Jarra. Segmentation of blood images using morphological operators. In *15th IEEE International Conference on Pattern Recognition (ICPR)*, pages 397–400, 2000.

[45] C. Di Ruberto, A. Dempster, S. Khan, and B. Jarra. Analysis of infected blood cell images using morphological operators. *Image and Vision Computing*, 20(2):133–146, 2002.

[46] C. Di Ruberto, A. Dempster, Sh. Khan, and B. Jarra. Morphological image processing for evaluating malaria disease. In *Visual Form*, volume 2059 of *Lecture Notes in Computer Science*, pages 739–748. Springer Berlin, Heidelberg, 2001.

[47] A. P. Dobrowolski, M. Wierzbowski, and K. Tomczykiewicz. Multiresolution MUAPs decomposition and SVM-based analysis in the classification of

neuromuscular disorders. *Computer Methods and Programs in Biomedicine*, 107(3):393 – 403, 2012.

[48] G. Dong, N. Ray, and S.T. Acton. Intravital leukocyte detection using the gradient inverse coefficient of variation. *IEEE Transactions on Medical Imaging*, 24(7):910–924, Jul. 2005.

[49] D.L. Donoho. De-noising by soft-thresholding. *IEEE Transactions on Information Theory*, 41(3):613–627, 1995.

[50] D.L. Donoho and I.M. Johnstone. Adapting to unknown smoothness via wavelet shrinkage. *Journal of the American Statistical Association*, 90(432):1200–1224, 1995.

[51] L.B. Dorini, R. Minetto, and N.J. Leite. Semi-automatic white blood cell segmentation based on multiscale analysis. *IEEE Journal of Biomedical and Health Informatics*, 17(1):250–256, 2013.

[52] S.R. Dubois and F.H. Glanz. An autoregressive model approach to two-dimensional shape classification. *IEEE Transactions on Pattern Analysis and Machine Intelligence*, 8(1):55–66, 1986.

[53] M.P. Dubuisson and A.K. Jain. A modified hausdorff distance for object matching. In *12th IAPR International Conference on Pattern Recognition*, volume 1, pages 566–568, 1994.

[54] I. El-Naqa, Yongyi Y., M.N. Wernick, N.P. Galatsanos, and R.M. Nishikawa. A support vector machine approach for detection of microcalcifications. *IEEE Transactions on Medical Imaging*, 21(12):1552–1563, Dec. 2002.

[55] J. Fan, R. Wang, L. Zhang, D. Xing, and F. Gan. Image sequence segmentation based on 2D temporal entropic thresholding. *Pattern Recognition Letters*, 17(10):1101 – 1107, 1996.

[56] M.L. Feng and Y.P. Tan. Contrast adaptive binarization of low quality document images. *IEICE Electron. Express*, 1(16):501 – 506, 2004.

[57] S. Fischer, F. sroubek, L. Perrinet, R. Redondo, and G. Cristbal. Self-invertible 2D Log-Gabor Wavelets. *International Journal of Computer Vision*, 75(2):231–246, 2007.

[58] S. Fleagle, M. Johnson, C. Wilbricht, D. Skorton, R. Wilson, C. White, M. Marcus, and S. Collins. Automated analysis of coronary arterial morphology in cineangiograms: geometric and physiologic validation in humans. *IEEE Transactions on Medical Imaging*, 8(4):387–400, 1989.

[59] S. Fleagle, D. Thedens, J. Ehrhardt, T. Scholz, and D. Skorton. Automated identification of left ventricular borders from spin-echo magnetic resonance images. *Investigative Radiology*, 26(4):295–303, 1991.

[60] I. Fodor and C. Kamath. On denoising images using wavelet-based statistical techniques. Technical report, Lawrence Livermore National Laboratory, 2001.

[61] H. Freeman. Computer processing of line-drawing images. *ACM Computing Surveys*, 6(1):57–97, 1974.

[62] B. Fu, J. Zhou, Y. Li, G. Zhang, and Ch. Wang. Image analysis by modified legendre moments. *Pattern Recognition*, 40(2):691 – 704, 2007.

[63] K. Fukunaga. *Introduction to Statistical Pattern Recognition,second ed.* Academic Press Inc, New York, NY, USA, 1992.

[64] B. Gatos, I. Pratikakis, and S. Perantonis. An adaptive binarization technique for low quality historical documents. In *Document Analysis Systems VI*, volume 3163 of *Lecture Notes in Computer Science*, pages 102–113. Springer Berlin Heidelberg, 2004.

[65] B. Gatos, I. Pratikakis, and S.J. Perantonis. Adaptive degraded document image binarization. *Pattern Recognition*, 39(3):317 – 327, 2006.

[66] E. Gering and C. Atkinson. A rapid method for counting nucleated erythrocytes on stained blood smears by digital image analysis. *Journal of Parasitology*, 90(4):879–881, 2004.

[67] L. Gooldman and A. Schafer. The peripheral blood smear. In *Cecil Medicine*, chapter 160. Saunders Elsevier, Philadelphia, Pa, 24 edition, 2011.

[68] G.H. Granlund. Fourier preprocessing for hand print character recognition. *IEEE Transactions on Computers*, C-21(2):195–201, 1972.

[69] E. Grimaldi and F. Scopacasa. Evaluation of the abbott CELL-DYN 4000 hematology analyzer. *American Journal of Clinical Pathology*, 113(4):497–505, Apr. 2000.

[70] Yu-Hua Gu and T. Tjahjadi. Efficient planar object tracking and parameter estimation using compactly represented cubic B-spline curves. *IEEE Transactions on Systems, Man and Cybernetics, Part A: Systems and Humans*, 29(4):358–367, 1999.

[71] H. Taghizad E. Khajehpour H. Khajehpour, A. Mehri Dehnavi and M.R. Naeemabadi. Detection and segmentation of erythrocytes in blood smear images using a line operator and watershed algorithm. *Journal of Medical Signals and Sensors*, 3(3):164–171, Sept. 2013.

[72] M. Habibzadeh, A. Krzyżak, and T. Fevens. Application of pattern recognition techniques for the analysis of thin blood smear images. *Journal of Medical Informatics & Technologies.*, 18(1):29–40, 2011.

[73] M. Habibzadeh, A. Krzyżak, and T. Fevens. Analysis of white blood cell differential counts using dual-tree complex wavelet transform and support vector machine classifier. In *International Conference on Computer Vision and Graphics (ICCVG)*, volume 7594, pages 414–422, Sept. , 2012.

[74] M. Habibzadeh, A. Krzyżak, and T. Fevens. Comparative study of shape, intensity and texture features and support vector machine for white blood cell classification. *Journal of Theoretical and Applied Computer Science*, 7:20–35, 2013.

[75] M. Habibzadeh, A. Krzyżak, and T. Fevens. White blood cell differential counts using Convolutional Neural Networks for low resolution images. In *Artificial Intelligence and Soft Computing*, volume 7895 of *Lecture Notes in Computer Science*, pages 263–274. Springer Berlin Heidelberg, 2013.

[76] M. Habibzadeh, A. Krzyżak, and T. Fevens. Comparative Study of Feature Selection for White Blood Cell Differential Counts in Low Resolution Images.

In *Artificial Neural Networks in Pattern Recognition (ANNPR)*, volume 8774 of *Lecture Notes in Computer Science*, pages 216–227. Springer International Publishing Switzerland, Oct. 2014.

[77] M. Habibzadeh, A. Krzyżak, and T. Fevens. Feature selection using RS-HDMR and Branch & Bound algorithms for white blood cell classification in low resolution images. *Journal of Computers in Biology and Medicine (Submitted)*, 2015.

[78] M. Habibzadeh, A. Krzyżak, T. Fevens, and A. Sadr. Counting of RBCs and WBCs in noisy normal blood smear microscopic images. In *SPIE Medical Imaging : Computer-Aided Diagnosis*, volume 7963, page 79633I, Feb. 2011.

[79] J. Haddadnia, M. Ahmadi, and K. Faez. An efficient feature extraction method with pseudo-Zernike moment in RBF neural network-based human face recognition system. *EURASIP Journal on Applied Signal Processing*, 2003:890–901, Jan. 2003.

[80] M. Hamghalam, M. Motameni, and A.E. Kelishomi. Leukocyte segmentation in giemsa-stained image of peripheral blood smears based on active contour. In *IEEE International Conference on Signal Processing Systems*, pages 103–106, May. 2009.

[81] L.W. Hao, W.X. Hong, and C.L. Hu. A novel auto-segmentation scheme for colored Leukocyte images. In *International Conference on Pervasive Computing Signal Processing and Applications (PCSPA)*, pages 916–919, Sept. 2010.

[82] R.M. Haralick, K. Shanmugam, and I. Dinstein. Textural features for image classification. *IEEE Transactions on Systems, Man and Cybernetics*, SMC-3(6):610 –621, Nov. 1973.

[83] Bharath Hariharan, Pablo Arbeláez, Ross Girshick, and Jitendra Malik. Simultaneous detection and segmentation. In *European Conference on Computer Vision (ECCV)*, pages 1–16, 2014.

[84] D. Harwood, M. Subbarao, H. Hakalahti, and L.S. Davis. A new class of edge-preserving smoothing filters. *Pattern Recognition Letters*, 6(3):155 – 162, 1987.

[85] G. Hayem. *Du sang et de ses altérations anatomiques*. Paris : G. Masson, New York, NY, USA, 1889.

[86] R. Hedjam, R. Farrahi Moghaddam, and M. Cheriet. A spatially adaptive statistical method for the binarization of historical manuscripts and degraded document images. *Pattern Recognition*, 44(9):2184 – 2196, 2011.

[87] J. Herman, J. Sheeba Rani, and D. Devaraj. Face recognition using generalized pseudo-zernike moment. In *Annual IEEE India Conference*, pages 1–4, 2009.

[88] A Hoover, V. Kouznetsova, and M. Goldbaum. Locating blood vessels in retinal images by piecewise threshold probing of a matched filter response. *IEEE Transactions on Medical Imaging*, 19(3):203–210, Mar. 2000.

[89] Kh.M. Hosny. Image representation using accurate orthogonal Gegenbauer moments. *Pattern Recognition Letters*, 32(6):795 – 804, 2011.

[90] B. Hu and S. Liao. Chinese character recognition by Krawtchouk moment features. In *Image Analysis and Recognition*, volume 7950 of *Lecture Notes in Computer Science*, pages 711–716. Springer Berlin Heidelberg, 2013.

[91] M.K. Hu. Visual pattern recognition by moment invariants. *IEEE Transactions on Information Theory*, 8(2):179–187, 1962.

[92] H. Huang, G. Coatrieux, H.Z. Shu, L.M. Luo, and C. Roux. Blind forensics in medical imaging based on Tchebichef image moments. In *Annual IEEE International Engineering in Medicine and Biology Society Conference*, pages 4473–4476, 2011.

[93] A. Jain and D. Zongker. Feature selection: evaluation, application, and small sample performance. *IEEE Transactions on Pattern Analysis and Machine Intelligence*, 19(2):153–158, 1997.

[94] L. Jelen, T. Fevens, and A. Krżyzak. Influence of nuclei segmentation on breast cancer malignancy classification. *Proceedings of SPIE*, 7260:726014–726014–9, 2009.

[95] K. Jiang, Q.M. Liao, and S.Y. Dai. A novel white blood cell segmentation scheme using scale-space filtering and watershed clustering. In *IEEE International Conference on Machine Learning and Cybernetics*, pages 2820–2825, Nov. 2003.

[96] I.T Jolliffe. *Principal Component Analysis*. Springer-Verlag (New York Inc), 2 edition, 2002.

[97] J.N. Kapur, P.K. Sahoo, and A.K.C. Wong. A new method for gray-level picture thresholding using the entropy of the histogram. *Computer Vision, Graphics, and Image Processing*, 29(3):273 – 285, 1985.

[98] V. Kariwala, L. Ye, and Y. Cao. Branch and bound method for regression-based controlled variable selection. *Computers & Chemical Engineering*, 54(0):1 – 7, 2013.

[99] M. Kass, A. Witkin, and D. Terzopoulos. Snakes: Active contour models. *International Journal of Computer Vision*, 4:321–331, 1988.

[100] H. Kauppinen, T. Seppanen, and M. Pietikainen. An experimental comparison of autoregressive and fourier-based descriptors in 2D shape classification. *IEEE Transactions on Pattern Analysis and Machine Intelligence*, 17(2):201–207, 1995.

[101] G.T. Kaya, H. Kaya, and O.K. Ersoy. Feature selection by high dimensional model representation and its application to remote sensing. In *IEEE International Geoscience and Remote Sensing Symposium (IGARSS)*, pages 4938–4941, 2012.

[102] Kh. Khurshid, I. Siddiqi, C. Faure, and N. Vincent. Comparison of Niblack inspired binarization methods for ancient documents. In *Proceedings of SPIE*, volume 7247, pages 72470U–72470U–9, 2009.

[103] T.Y. Kim and H.K. Choi. Computerized Renal Cell Carcinoma Nuclear Grading Using 3D Textural Features. In *IEEE International Conference on Communications (ICC) Workshops*, pages 1–5, 2009.

[104] N.G. Kingsbury. Complex wavelets for shift invariant analysis and filtering of signals. *Applied and Computational Harmonic Analysis*, 10(3):234 – 253, May. 2001.

[105] N.G. Kingsbury. Design of Q-shift complex wavelets for image processing using frequency domain energy minimization. In *International Conference on Image Processing (ICIP)*, volume 1, pages I – 1013–16, Sept. 2003.

[106] B.C. Ko, J.W. Gim, and J.Y. Nam. Cell image classification based on ensemble features and random forest. *Electronics Letters*, 47(11):638–639, May. 2011.

[107] Byoung Chul Ko, Ja-Won Gim, and Jae-Yeal Nam. Automatic white blood cell segmentation using stepwise merging rules and gradient vector flow snake. *Micron*, 42(7):695 – 705, 2011.

[108] S. Kok-Swee, A. Faizy Salleh, Ch. Chee-way, Rosli B, and G. Hock-ann. Translation and scale invariants of Hahn moments. *International Journal of Image and Graphics*, 09(02):271–285, 2009.

[109] P. Kovesi. Phase Preserving Denoising of Images. In *The Australian Pattern Recognition Society Conference: DICTA*, pages 212 –217, Dec. 1999.

[110] E. Kreyszig. Legendre Equation. Legendre Polynomials Pn(x). In *Advanced Engineering Mathematics*, chapter 5, pages 175–180. John Wiley & Sons, Inc, New York, 2011.

[111] M.M.R. Krishnan, M. Pal, S.K Bomminayuni, Ch. Chakraborty, R.R. Paul, J. Chatterjee, and A.K. Ray. Automated classification of cells in sub-epithelial connective tissue of oral sub-mucous fibrosis-an SVM based approach. *Computers in Biology and Medicine*, 39(12):1096 – 1104, 2009.

[112] A. Krizhevsky, I. Sutskever, and G.E. Hinton. ImageNet classification with deep convolutional neural networks. In *25th International Conference Neural Information Processing Systems*, pages 1 – 9, Dec. , 2012.

[113] A. Krzyżak, T. Fevens, M. Habibzadeh, and L. Jelen. Application of pattern recognition techniques for the analysis of histopathological images. In *Computer Recognition Systems 4*, volume 95 of *Advances in Intelligent and Soft Computing*, pages 623–644. Springer, 2011.

[114] B.R. Kumar, D.K. Joseph, and T.V. Sreenivas. Teager energy based blood cell segmentation. In *14th International Conference on Digital Signal Processing*, pages 619–622, Jul. 2002.

[115] M. Kuwahara, K. Hachimura, S. Eiho, and M. Kinoshita. Processing of RI-Angiocardiographic images. In *Digital Processing of Biomedical Images*, pages 187–202. Springer US, 1976.

[116] J. R. Landis and G.G. Koch. The measurement of observer agreement for categorical data. *Biometrics*, 33(1):159–174, 1977.

[117] F. Lauer, C.Y. Suen, and G. Bloch. A trainable feature extractor for handwritten digit recognition. *Journal of Pattern Recognition*, 40(6):1816 – 1824, 2007.

[118] S. Lawrence, C. Lee Giles, A.Ch. Tsoi, and A.D. Back. Face recognition: A Convolutional Neural Network approach. *IEEE Transactions on Neural Networks*, 8(1):98–113, 1997.

[119] Y. LeCun, L. Bottou, Y. Bengio, and P. Haffner. Gradient-based learning applied to document recognition. *Proceedings of the IEEE*, 86(11):2278–2324, Nov. 1998.

[120] Y. LeCun and C. Cortes. The MNIST database of handwritten digits. `http://yann.lecun.com/exdb/mnist`, 1998. [Online; accessed 20-Jul-2015].

[121] Y. LeCun, F.-J. Huang, and L. Bottou. Learning methods for generic object recognition with invariance to pose and lighting. In *IEEE Computer Society Conference on Computer Vision and Pattern Recognition*, volume 2, pages II–97–104, June 27-July 2, 2004.

[122] P. Lepcha, W. Srisukkham, Li Zh., and A. Hossain. Red blood based disease screening using marker controlled watershed segmentation and post-processing. In *8th International Conference on Software, Knowledge, Information Management and Applications (SKIMA)*, pages 1–7, Dec. 2014.

[123] O. Lezoray, A. Elmoataz, H. Cardot, G. Gougeon, M. Lecluse, H. Elie, and M. Revenu. Segmentation of cytological images using color and mathematical morphology. *Acta Stereologica*, 18(1):1–14, 1999.

[124] B. Li, G. Zhang, and B. Fu. Image analysis using radial Fourier-Chebyshev moments. In *International Conference on Multimedia Technology (ICMT)*, pages 3097–3100, 2011.

[125] G. Li, T. Liu, A. Tarokh, J. Nie, L. Guo, A. Mara, S. Holley, and S. Wong. 3D cell nuclei segmentation based on gradient flow tracking. *BMC Cell Biology*, 8(1), 2007.

[126] G. Li, C. Rosenthal, and H. Rabitz. High dimensional model representations. *The Journal of Physical Chemistry A*, 105(33):7765–7777, 2001.

[127] S. Li, M.C. Lee, and C.M. Pun. Complex Zernike moments features for shape-based image retrieval. *IEEE Transactions on Systems, Man and Cybernetics, Part A: Systems and Humans*, 39(1):227–237, 2009.

[128] S. Li, M.Ch Lee, and Ch.M Pun. Complex Zernike moments features for shape-based image retrieval. *IEEE Transactions on Systems, Man and Cybernetics, Part A: Systems and Humans*, 39(1):227–237, 2009.

[129] Sh. Li, T. Fevens, A. Krzyżak, and S. Li. Automatic clinical image segmentation using pathological modeling, PCA and SVM. *Engineering Applications of Artificial Intelligence*, 19(4):403 – 410, 2006.

[130] S. Liao, A. Chiang, Q. Lu, and M. Pawlak. Chinese character recognition via gegenbauer moments. In *16th International Conference on Pattern Recognition*, volume 3, pages 485–488, 2002.

[131] Y.C. Lin, Y.P. Tsai, Y.P. Hung, and Z.C. Shih. Comparison between immersion-based and toboggan-based watershed image segmentation. *IEEE Transactions on Image Processing*, 15(3):632–640, Mar. 2006.

[132] Q. Liu, H. Zhu, and Q. Li. Object recognition by combined invariants of orthogonal fourier-mellin moments. In *8th International Conference on Information, Communications and Signal Processing (ICICS)*, pages 1–5, 2011.

[133] V.V. Makkapati. Improved wavelet-based microscope autofocusing for blood smears by using segmentation. In *IEEE International Conference on Automation Science and Engineering*, pages 208–211, Aug. 2009.

[134] L.CH. Malassez. De la numération des globules rouges du sang. *C.R. Acad. Sci.*, 75(1528), 1872.

[135] S. Mandal, A. Kumar, J. Chatterjee, M. Manjunatha, and A.K. Ray. Segmentation of blood smear images using normalized cuts for detection of malarial parasites. In *Annual IEEE India Conference (INDICON)*, pages 1 –4, Dec. 2010.

[136] J. V. Manjón, P. Coupé, L. Concha, A. Buades, D. L. Collins, and M. Robles. Diffusion weighted image denoising using overcomplete local PCA. *PLoS ONE*, 8(9):e73021, Sept. 2013.

[137] J. Víctor Marcos and G. Cristóbal. Texture classification using discrete Tchebichef moments. *Journal of the Optical Society of America A*, 30(8):1580–1591, Aug. 2013.

[138] A. Martelli. An application of heuristic search methods to edge and contour detection. *Communications of the ACM*, 19(2):73–83, 1976.

[139] R.A. McPherson and M.R. Pincus. *Henry Clinical Diagnosis and Management by Laboratory Methods*, chapter Basic examination of blood and bone marrow, pages 509–556. Elsevier Health Sciences, 22 edition, 2012.

[140] A Meijster and M.H.F. Wilkinson. Fast computation of morphological area pattern spectra. In *International Conference on Image Processing*, volume 3, pages 668–671, 2001.

[141] A.M. Mendonça and A. Campilho. Segmentation of retinal blood vessels by combining the detection of centerlines and morphological reconstruction. *IEEE Transactions on Medical Imaging*, 25(9):1200–1213, Sept. 2006.

[142] R.F. Moghaddam and M. Cheriet. A variational approach to degraded document enhancement. *IEEE Transactions on Pattern Analysis and Machine Intelligence*, 32(8):1347–1361, Aug. 2010.

[143] K.N.R. Mohana Rao and A G. Dempster. Area-granulometry: an improved estimator of size distribution of image objects. *Electronics Letters*, 37(15):950–951, Jul. 2001.

[144] S. Mohapatra, D. Patra, and K. Kumar. Blood microscopic image segmentation using rough sets. In *International Conference on Image Information Processing (ICIIP)*, pages 1–6, Nov. 2011.

[145] F. Mokhtarian and M. Bober. Robust image corner detection through curvature scale space. In *Curvature Scale Space Representation: Theory, Applications, and MPEG-7 Standardization*, volume 25 of *Computational Imaging and Vision*, pages 215–242. Springer Netherlands, 2003.

[146] F. Mokhtarian and R. Suomela. Robust image corner detection through curvature scale space. *IEEE Transactions on Pattern Analysis and Machine Intelligence*, 20(12):1376–1381, 1998.

[147] D Mukherjee, B. Rao, and A. Prasad. Cut-HDMR-based fully equivalent operational model for analysis of unreinforced masonry structures. *Journal of Sadhana*, 37(5):609–628, 2012.

[148] D.P. Mukherjee, N. Ray, and S.T. Acton. Level set analysis for leukocyte detection and tracking. *IEEE Transactions on Image Processing*, 13(4):562–572, 2004.

[149] R. Mukundan. Radial Tchebichef invariants for pattern recognition. In *International IEEE Region 10 Conference, TENCON*, pages 1–6, 2005.

[150] R. Mukundan, S.H. Ong, and P. A. Lee. Image analysis by Tchebichef moments. *IEEE Transactions on Image Processing*, 10(9):1357–1364, 2001.

[151] R. Muralidharan and C. Chandrasekar. Scale invariant feature extraction for identifying an object in the image using moment invariants. In *International Conference on Communication and Computational Intelligence (INCOCCI)*, pages 452 –456, Dec. 2010.

[152] C. Mythili and V. Kavitha. Efficient technique for color image noise reduction. *The Research Bulletin of Jordan ACM*, II(III):41 – 44, 2011.

[153] A. Nabatchian, I. Makaremi, E. Abdel-Raheem, and M. Ahmadi. Pseudo-zernike moment invariants for recognition of faces using different classifiers in

FERET database. In *Third International Conference on Convergence and Hybrid Information Technology*, volume 1, pages 933–936, 2008.

[154] F. Narváez and E. Romero. Breast mass classification using orthogonal moments. In *Breast Imaging*, volume 7361 of *Lecture Notes in Computer Science*, pages 64–71. Springer Berlin Heidelberg, 2012.

[155] W. Niblack. *An Introduction to Digital Image Processing*. Prentice-Hall, Inc., Upper Saddle River, NJ, USA, 1990.

[156] B. Nilsson and A Heyden. Segmentation of complex cell clusters in microscopic images: Application to bone marrow samples. *Cytometry Part A*, 66A(1):24–31, 2005.

[157] K. Ntirogiannis, B. Gatos, and I. Pratikakis. A combined approach for the binarization of handwritten document images. *Pattern Recognition Letters*, 35(0):3 – 15, 2014.

[158] Wadsworth Center New York State Department of Health. Clinical chemistry and hematology laboratories. `http://www.wadsworth.org/chemheme/`, 2014. [Online; accessed 20-Jul-2015].

[159] G. Oliver. The croonian lectures: A contribution to the study of the blood and the circulation. *The Lancet*, 147(3798):1621 – 1627, 1896.

[160] G. Ongun, U. Halici, K. Leblebicioglu, V. Atalay, M. Beksac, and S. Beksac. Feature extraction and classification of blood cells for an automated differential blood count system. In *International Joint Conference on Neural Networks*, pages 2461–2466, Jul. 2001.

[161] G. Ongun, U. Halici, K. Leblebicioglu, V. Atalay, M. Beksac, and S. Beksak. An automated differential blood count system. In *IEEE International Conference on Engineering in Medicine and Biology Society*, volume 3, pages 2583–2586, 2001.

[162] G. Ongun, U. Halici, K. Leblebicioglu, V. Atalay, S. Beksac, and M. Beksac. Automated contour detection in blood cell images by an efficient snake algorithm. *Nonlinear Analysis-Theory Methods & Applications*, 47(9):5839–5847, 2001.

[163] S. Osowski, R. Siroic, T. Markiewicz, and K. Siwek. Application of support vector machine and genetic algorithm for improved blood cell recognition. *IEEE Transactions on Instrumentation and Measurement*, 58(7):2159–2168, Jul. 2009.

[164] N. Otsu. A threshold selection method from gray-level histograms. *IEEE Transactions on System, Man and Cybernetics*, 9(1):62–66, Jan. 1979.

[165] N.C. Smeeton P. Sprent. *Applied Non Parametric Statistical Methods*, chapter 5. Methods for Two Independent Samples, pages 151–191. Chapman & Hall/CRC, London, fourth edition, 2007.

[166] G.A. Papakostas, B.G. Mertzios, and D.A. Karras. Performance of the orthogonal moments in reconstructing biomedical images. In *16th International Conference on Systems, Signals and Image Processing (IWSSIP)*, pages 1–4, 2009.

[167] G. Papari, N. Petkov, and P. Campisi. Artistic edge and corner enhancing smoothing. *IEEE Transactions on Image Processing*, 16(10):2449–2462, 2007.

[168] P. Patidar, M. Gupta, S. Srivastava, and A.K. Nagawat. Image de-noising by various filters for different noise. *International Journal of Computer Applications*, 9:45–50, 2010.

[169] T. Pavlidis. Representation of figures by labeled graphs. *Pattern Recognition*, 4(1):5 – 17, 1972.

[170] Y. Peng, J. Chen, X. Xu, and F. Pu. SAR Images Statistical Modeling and Classification Based on the Mixture of Alpha-Stable Distributions. *Remote Sensing*, 5(5):2145–2163, 2013.

[171] E. Persoon and K.S. Fu. Shape discrimination using fourier descriptors. *IEEE Transactions on Systems, Man and Cybernetics,*, 7(3):170–179, 1977.

[172] Z. Ping, R. Wu, and Y. Sheng. Image description with Chebyshev-Fourier moments. *Journal of the Optical Society of America A*, 19(9):1748–1754, Sept. 2002.

[173] V. Piuri and F. Scotti. Morphological classification of blood leucocytes by microscope images. In *IEEE international Conference on Computational Intelligence Far Measurement Systems and Applications*, pages 103–108, Jul. 2004.

[174] A. Pizurica and W. Philips. Estimating the probability of the presence of a signal of interest in multiresolution single- and multiband image denoising. *IEEE Transactions on Image Processing*, 15(3):654–665, Mar. 2006.

[175] Bhanu Prasad and S.R. Mahadeva Prasanna, editors. *Speech, Audio, Image and Biomedical Signal Processing using Neural Networks*, volume 83 of *Studies in Computational Intelligence*. Springer, 2008.

[176] P. Quelhas, M. Marcuzzo, AM. Mendonça, and A Campilho. Cell nuclei and cytoplasm joint segmentation using the sliding band filter. *IEEE Transactions on Medical Imaging*, 29(8):1463–1473, Aug. 2010.

[177] H. Rabbani, M. Vafadust, P. Abolmaesumi, and S. Gazor. Speckle Noise Reduction of Medical Ultrasound Images in Complex Wavelet Domain Using Mixture Priors. *IEEE Transactions on Biomedical Engineering*, 55(9):2152 –2160, Sept. 2008.

[178] S. Rahman. Extended polynomial dimensional decomposition for arbitrary probability distributions. *Journal of Engineering Mechanics*, 135(12):1439–1451, 2009.

[179] P.A. Raj. Image contrast enhancement using discrete Dual Hahn moments. In *International Conference on Machine Vision Applications*, pages 206–209, 2013.

[180] B. Rajwa, M. Dundar, V. Patsekin, K. Huff, A. Bhunia, M. Venkatapathi, E. Bae, E.D. Hirleman, and J.P. Robinson. Morphotypic analysis and classification of bacteria and bacterial colonies using laser light-scattering, pattern recognition, and machine-learning system. In *Proc. SPIE*, volume 7306, pages 73061A–73061A–7, 2009.

[181] B. Rajwa, M. M. Dundar, F. Akova, A. Bettasso, V. Patsekin, Dan H.E., A.K. Bhunia, and J. P. Robinson. Discovering the unknown: Detection of emerging pathogens using a label-free light-scattering system. *Cytometry Part A*, 77A(12):1103–1112, 2010.

[182] B. Rajwa, M. Murat Dundar, F. Akova, V. Patsekin, E. Bae, Y. Tang, J. E. Dietz, E. D. Hirleman, J. P. Robinson, and A.K. Bhunia. Digital microbiology: detection and classification of unknown bacterial pathogens using a label-free laser light scatter-sensing system. In *Proc. SPIE*, volume 8029, pages 80290C–80290C–9, 2011.

[183] H. Ramoser, V. Laurain, H. Bischof, and R. Ecker. Leukocyte segmentation and classification in blood-smear images. In *27th IEEE Annual Conference Engineering in Medicine and Biology*, pages 3371–3374, Shanghai, China, Sept. 1-4, 2005.

[184] S. Rathore, A. Iftikhar, A. Ali, M. Hussain, and A. Jalil. Capture largest included circles: An approach for counting red blood cells. In *Emerging Trends and Applications in Information Communication Technologies*, volume 281 of *Communications in Computer and Information Science CCIS*, pages 373–384. Springer Berlin Heidelberg, 2012.

[185] H. Ren, A. Liu, J. Zou, D. Bai, and Z. Ping. Character reconstruction with radial-harmonic-Fourier moments. In *Fourth International Conference on Fuzzy Systems and Knowledge Discovery*, volume 3, pages 307–310, Aug. 2007.

[186] H. Ren, Z. Ping, W. Bo, W. Wu, and Y. Sheng. Cell image recognition with radial harmonic Fourier moments. *Chinese Physics*, 12(6):610–614, Jun. 2003.

[187] H. Ren, Z. Ping, W. Bo, W. Wu, and Y. Sheng. Multi distortion-invariant image recognition with radial harmonic Fourier moments. *Journal of the Optical Society of America A*, 20(4):631–637, Apr. 2003.

[188] S.H. Rezatofighi, A. Roodaki, R.A. Zoroofi, R. Sharifian, and H. Soltanian-Zadeh. Automatic detection of red blood cells in hematological images using polar transformation and run-length matrix. In *9th International Conference on Signal Processing*, pages 806–809, Oct. 2008.

[189] S.H. Rezatofighi and H. Soltanianzadeh. Automatic recognition of five types of white blood cells in peripheral blood. *Computerized Medical Imaging and Graphics*, 35(4):333 – 343, 2011.

[190] T. W. Ridler and S. Calvard. Picture thresholding using an iterative selection method. *IEEE Transactions on Systems, Man, and Cybernetics*, 8:630–632, 1978.

[191] D. Rivest-Hénault, M. Cheriet, S. Deschênes, and C. Lapierre. Length increasing active contour for the segmentation of small blood vessels. In *20th International Conference on Pattern Recognition (ICPR)*, pages 2796–2799, Aug. 2010.

[192] R. Robinson, L. Benjamin, J. Cosgri, C. Cox, O. Lapets, P. Rowley, E. Yatco, and L. Wheeless. Textural differences between AA and SS blood specimens as detected by image analysis. *Cytometry*, 17(2):167–172, 1994.

[193] K. Rodenacker and E. Bengtsson. A feature set for cytometry on digitized microscopic images. *Analytical Cellular Pathology*, 25(1):1–36, 2001.

[194] R. Rowan. Automated examination of the peripheral blood smear. In *Automation and Quality Assurance in Hematology*, chapter 5, pages 129–177. Blackwell Scientific, Oxford, 1986.

[195] R. Rowan and J. M. England. Automated examination of the peripheral blood smear. In *Automation and quality assurance in hematology*, chapter 5, pages 129–177. Blackwell Scientific Oxford, 1986.

[196] S.T. Roweis and L.K. Saul. Nonlinear dimensionality reduction by locally linear embedding. *Science*, 290:2323–2326, 2000.

[197] K. Ruzicka, M. Veitl, R. Thalhammer-Scherrer, and I. Schwarzinger. New hematology analyzer Sysmex XE-2100 : performance evaluation of a novel white blood cell differential technology. *Archives of Pathology and Laboratory Medicine*, 125(3):391–396, 2001.

[198] F. Sadeghian, Z. Seman, A.R. Ramli, Badrul H. Abdul K., and M.I Saripan. A framework for white blood cell segmentation in microscopic blood images

using digital image processing. *Biological Procedures Online*, 11(1):196–206, Dec. 2009.

[199] J. Salmon, Z. Harmany, Ch.A. Deledalle, and R. Willett. Poisson noise reduction with non-local PCA. *Journal of Mathematical Imaging and Vision*, 48(2):279–294, 2014.

[200] F. Sand and E.R. Dougherty. Robustness of granulometric moments. *Pattern Recognition*, 32(9):1657 – 1665, 1999.

[201] J. Sauvola and M . Pietikainen. Adaptive document image binarization. *Pattern Recognition*, 33(2):225–236, Feb. 2000.

[202] B. Schachter. Decomposition of polygons into convex sets. *IEEE Transactions on Computers*, C-27(11):1078–1082, 1978.

[203] I.W. Selesnick, R.G. Baraniuk, and N.G. Kingsbury. The dual-tree complex wavelet transform. *IEEE Signal Processing Magazine*, 22(6):123 – 151, Nov. 2005.

[204] L. Sendur and I.W. Selesnick. A bivariate shrinkage function for wavelet-based denoising. In *IEEE International Conference on Acoustics, Speech, and Signal Processing (ICASSP)*, volume 2, pages 1261–1264, 2002.

[205] L. Sendur and I.W. Selesnick. Bivariate shrinkage functions for wavelet-based denoising exploiting interscale dependency. *IEEE Transactions on Signal Processing,*, 50(11):2744–2756, Nov. 2002.

[206] J. Serra. *Image Analysis and Mathematical Morphology*. Academic Press, Inc., USA, 1983.

[207] Y. Sheng and L. Shen. Orthogonal fourier-mellin moments for invariant pattern recognition. *Journal of the Optical Society of America A*, 11(6):1748–1757, Jun. 1994.

[208] W. Shitong and W. Min. A new detection algorithm (NDA) based on fuzzy cellular neural networks for white blood cell detection. *IEEE Transactions on Information Technology in Biomedicine*, 10(1):5–10, Jan. 2006.

[209] H. Shu, L. Luo, and J.-L. Coatrieux. Moment-based approaches in imaging. 1. basic features. *IEEE Engineering in Medicine and Biology Magazine*, 26(5):70–74, 2007.

[210] P.Y. Simard, D. Steinkraus, and J.C. Platt. Best practices for convolutional neural networks applied to visual document analysis. In *7th International Conference on Document Analysis and Recognition*, pages 958 – 963, Aug. 2003.

[211] Ch. Singh and S.K. Ranade. A high capacity image adaptive watermarking scheme with radial harmonic Fourier moments. *Digital Signal Processing*, 23(5):1470 – 1482, 2013.

[212] Ch. Singh and R. Upneja. Accurate computation of orthogonal fourier-mellin moments. *Journal of Mathematical Imaging and Vision*, 44(3):411–431, 2012.

[213] N. Sinha and A.G. Ramakrishnan. Automation of differential blood count. In *IEEE International Conference on Convergent Technologies for Asia-Pacific Region*, pages 547–551, Oct. 2003.

[214] I.M. Sobol. Global sensitivity indices for nonlinear mathematical models and their Monte Carlo estimates. *Mathematics and Computers in Simulation*, 55(13):271 – 280, 2001.

[215] P. Sobrevilla, E. Montseny, and J. Keller. White blood cell detection in bone marrow images. In *18th International Conference of the North American Fuzzy Information Processing Societ, (NAFIPS)*, pages 403–407, 1999.

[216] P. Somol, P. Pudil, and J. Kittler. Fast branch & bound algorithms for optimal feature selection. *IEEE Transactions on Pattern Analysis and Machine Intelligence*, 26(7):900–912, Jul. 2004.

[217] P. Sprawls. *Physical Principles of Medical Imaging (2nd Edition)*. Medical Physics Pub, 1995.

[218] M. Stiglmayr, F. Pfeuffer, and K. Klamroth. A branch and bound algorithm for medical image registration. In *Combinatorial Image Analysis*, volume 4958 of *Lecture Notes in Computer Science*, pages 217–228. Springer Berlin Heidelberg, 2008.

[219] B. Su, Sh. Lu, and Ch.L. Tan. Binarization of historical document images using the local maximum and minimum. In *Proceedings of the 9th IAPR International Workshop on Document Analysis Systems*, DAS '10, 2010.

[220] A. Subasi. Classification of EMG signals using PSO optimized SVM for diagnosis of neuromuscular disorders. *Computers in Biology and Medicine*, 43(5):576 – 586, 2013.

[221] S. Svensson. A decomposition scheme for 3D fuzzy objects based on fuzzy distance information. *Pattern Recognition Letters*, 28(2):224 – 232, 2007.

[222] H. Tamura, Sh. Mori, and T. Yamawaki. Textural features corresponding to visual perception. *IEEE Transactions on Systems, Man and Cybernetics*, 8(6):460–473, 1978.

[223] X. Tang. Texture information in runlength matrices. *IEEE Transactions on Image Processing*, 7(11):1602 – 1609, Nov. 1998.

[224] F.B. Tek, A.G. Dempster, and I. Kale. Malaria parasite detection in peripheral blood images. In *Proceedings of the British Machine Vision Conference*, pages 36.1–36.10. BMVA Press, 2006.

[225] F.B. Tek, A.G. Dempster, and I. Kale. Computer vision for microscopy diagnosis of malaria. *Malaria Journal*, 8(1):153–167, 2009.

[226] F.B. Tek, A.G. Dempster, and I. Kale. Parasite detection and identification for automated thin blood film malaria diagnosis. *Computer Vision and Image Understanding*, 114(1):21 – 32, 2010.

[227] J.Ch. Terrillon, M. Shirazi, D. McReynolds, M. Sadek, Y. Sheng, Sh. Akamatsu, and K. Yamamoto. Invariant face detection in color images using orthogonal Fourier-Mellin moments and support vector machines. In *Advances in Pattern Recognition - ICAPR*, volume 2013 of *Lecture Notes in Computer Science*, pages 83–92. Springer Berlin Heidelberg, 2001.

[228] N. Theera-Umpon and S. Dhompongsa. Morphological granulometric features of nucleus in automatic bone marrow white blood cell classification. *IEEE*

Transactions on Information Technology in Biomedicine, 11(3):353–359, May. 2007.

[229] K.H. Thung, S.C. Ng, C.L. Lim, and P. Raveendran. A preliminary study of compression efficiency and noise robustness of orthogonal moments on medical X-Ray images. In *5th Kuala Lumpur International Conference on Biomedical Engineering (IFMBE)*, volume 35, pages 587–590. Springer Berlin Heidelberg, 2011.

[230] V.J. Tiagrajah, O. Jamaludin, and H.N. Farrukh. Discriminant Tchebichef based moment features for face recognition. In *IEEE International Conference on Signal and Image Processing Applications (ICSIPA)*, pages 192–197, Nov.

[231] C. Tomasi and R. Manduchi. Bilateral filtering for gray and color images. In *Sixth IEEE International Conference on Computer Vision*, pages 839–846, Jan. 1998.

[232] A.B. Tosun and C. Gunduz-Demir. Graph run-length matrices for histopathological image segmentation. *IEEE Transactions on Medical Imaging*, 30(3):721–732, 2011.

[233] B. Tunga and M. Demiralp. A novel hybrid high-dimensional model representation (HDMR) based on the combination of plain and logarithmic high-dimensional model representations. In *Advances in Numerical Methods*, volume 11 of *Lecture Notes in Electrical Engineering*, pages 101–111. Springer US, 2009.

[234] M. A. Tunga and M. Demiralp. A factorized high dimensional model representation on the nodes of a finite hyperprismatic regular grid. *Applied Mathematics and Computation*, 164(3):865 – 883, 2005.

[235] M. A. Tunga and M. Demiralp. Hybrid high dimensional model representation (HHDMR) on the partitioned data. *Journal of Computational and Applied Mathematics*, 185(1):107 – 132, 2006.

[236] The university of Utah Eccles Health Sciences Library. The internet pathology laboratory for medical education. `http://library.med.utah.edu/WebPath/HEMEHTML/HEMEIDX.html#3`, 2014. [Online; accessed 20-Jul-2015].

[237] D.M. Ushizima, A.C. Lorena, and A.C.P.L.F. de Carvalho. Support Vector Machines Applied to White Blood Cell Recognition. In *5th International Conference on Hybrid Intelligent Systems*, pages 379–384, Nov. 2005.

[238] M. L. Verso. The evolution of blood-counting techniques. *Journal of Medical History*, 8(2):149–158, 1964.

[239] L. Vincent. Morphological grayscale reconstruction in image analysis: applications and efficient algorithms. *IEEE Transactions on Image Processing*, 2(2):176–201, Apr. 1993.

[240] L. Vincent and P. Soille. Watersheds in digital spaces: an efficient algorithm based on immersion simulations. *IEEE Transactions on Pattern Analysis and Machine Intelligence*, 13(6):583–598, Jun. 1991.

[241] K. Virordt. Neue methode der quantitativen mikroskopischen analyse des blutes. *Arch.f physiol*, 9(26), 1852.

[242] M. Wang and R. Chu. A novel white blood cell detection method based on boundary support vectors. In *IEEE International Conference on Systems, Man and Cybernetics*, SMC'09, pages 2595–2598, 2009.

[243] W. Wang and J.E. Mottershead. Adaptive moment descriptors for full-field strain and displacement measurements. *The Journal of Strain Analysis for Engineering Design*, 48(1):16–35, 2013.

[244] X. Wang and S. Liao. Image reconstruction from orthogonal fourier mellin moments. In *Image Analysis and Recognition*, volume 7950 of *Lecture Notes in Computer Science*, pages 687–694. Springer Berlin Heidelberg, 2013.

[245] L. J. Wei. Asymptotic conservativeness and efficiency of kruskal-wallis test for K dependent samples. *Journal of the American Statistical Association*, 76(376):1006–1009, 1981.

[246] X. Wei, Y. Cao, G. Fu, and Y. Wang. A counting method for complex overlapping erythrocytes-based microscopic imaging. *Journal of Innovative Optical Health Sciences*, 8(6):15500331–155003311, 2015.

[247] C. Wolf, J. Jolion, and F. Chassaing. Text localization, enhancement and binarization in multimedia documents. In *16th International Conference on Pattern Recognition*, volume 2, pages 1037–1040, 2002.

[248] K. Wu, C. Garnier, J. Coatrieux, and H. Shu. A preliminary study of moment-based texture analysis for medical images. In *Annual IEEE International Conference of the Engineering in Medicine and Biology Society (EMBC)*, pages 5581–5584, 2010.

[249] A. Wunsche. Generalized Zernike or disc polynomials. *Journal of Computational and Applied Mathematics*, 174(1):135 – 163, 2005.

[250] T. Xia, H. Zhu, H. Shu, P. Haigron, and L. Luo. Image description with generalized pseudo-Zernike moments. *Journal of the Optical Society of America A*, 24(1):50–59, Jan. 2007.

[251] Y. Xiao, Zh. Cao, and T. Zhang. Entropic thresholding based on gray-level spatial correlation histogram. In *19th International Conference on Pattern Recognition (ICPR)*, pages 1 –4, Dec. 2008.

[252] Y. Xiao-min, L. Li-min, and W. Yu. Automatic classification system for leukocytes in human blood. *Journal of Computer Science and Technology*, 17(2):130–136, 1994.

[253] S. Dambreville Y. Rathi and A. Tannenbaum. Statistical shape analysis using kernel PCA. In *SPIE Conferences: IS&T Electronic Imaging*, volume 6064, page 60641B, Jan. 2006.

[254] Sh. Yan, D. Xu, B. Zhang, H.J. Zhang, Q. Yang, and S. Lin. Graph embedding and extensions: A general framework for dimensionality reduction. *IEEE Transactions on Pattern Analysis and Machine Intelligence*, 29(1):40 –51, Jan. 2007.

[255] Y. Yang, Y. Cao, and W. Shi. A method of leukocyte segmentation based on s component and b component images. *Journal of Innovative Optical Health Sciences*, 07(01):1450007, 2014.

[256] P.T. Yap, R. Paramesran, and S.H. Ong. Image analysis by Krawtchouk moments. *IEEE Transactions on Image Processing*, 12(11):1367–1377, 2003.

[257] A.B.J. Teoh Y.H. Pang and D.C.L. Ngo. A discriminant pseudo Zernike moments in face recognition. *Journal of Research and Practice in Information Technology*, 38(2):197–211, May. 2006.

[258] B. Yu and B. Yuan. A more efficient branch and bound algorithm for feature selection. *Pattern Recognition*, 26(6):883 – 889, 1993.

[259] H. Yu, L. Zhao, and H. Wang. Image denoising using Trivariate shrinkage filter in the wavelet domain and joint bilateral filter in the spatial domain. *IEEE Transactions on Image Processing*, 18(10):2364 –2369, Oct. 2009.

[260] Q. Yuan and D. Liang. A new multiple sub-domain RS-HDMR method and its application to tropospheric alkane photochemistry model. *International Journal of Numbercial Analysis and Modeling, Series B*, 2(1):73 – 90, 2011.

[261] B. Kang Z. Ma and J. Ma. Translation and scale invariant of Legendre moments for images retrieval. *Journal of Information & Computational Science*, 8(11):2221–2229, 2011.

[262] F. Zamani and R. Safabakhsh. An unsupervised GVF snake approach for white blood cell segmentation based on nucleus. In *8th International Conference on Signal Processing*, volume 2, pages 16–20, 2006.

[263] C. Zhang, X. Xiao, X. Li, Y.J. Chen, W. Zhen, J. Chang, Ch. Zheng, and Zh. Liu. White blood cell segmentation by color-space-based k-means clustering. *Sensors (Basel, Switzerland)*, 14(9):16128–16147, 2014.

[264] H. Zhang, H. Shu, G.N. Han, G. Coatrieux, L. Luo, and J.L. Coatrieux. Blurred image recognition by Legendre moment invariants. *IEEE Transactions on Image Processing*, 19(3):596–611, Mar. 2010.

[265] F. Zhu, T. Carpenter, D.R. Gonzalez, M. Atkinson, and J. Wardlaw. Computed tomography perfusion imaging denoising using gaussian process regression. *Physics in Medicine and Biology*, 57(12):N183, 2012.

[266] H. Zhu, H. Shu, J. Zhou, L. Luo, and J.L. Coatrieux. Image analysis by discrete orthogonal dual hahn moments. *Pattern Recognition Letters*, 28(13):1688 – 1704, 2007.

[267] T. Ziehn and A.S. Tomlin. GUI-HDMR - a software tool for global sensitivity analysis of complex models. *Environmental Modelling & Software*, 24(7):775 – 785, 2009.